2019-07-01

Characterization of Phase Transformation and Twin Formation in Automotive Sheet Metal Alloys to Quantify and Understand Their Impact on Ductility

Isaac Chelladurai
Brigham Young University

Characterization of Phase Transformation and Twin Formation in Automotive Sheet Metal Alloys to Quantify and Understand Their Impact on Ductility

Isaac Chelladurai

A dissertation submitted to the faculty of
Brigham Young University
in partial fulfillment of the requirements for the degree of

Doctor of Philosophy

David T. Fullwood, Chair
Eric R. Homer
Oliver Kent Johnson
Michael Paul Miles
Tracy W. Nelson

Department of Mechanical Engineering

Brigham Young University

ABSTRACT

Characterization of Phase Transformation and Twin Formation in
Automotive Sheet Metal Alloys to Quantify and
Understand Their Impact on Ductility

Isaac Chelladurai
Department of Mechanical Engineering, BYU
Doctor of Philosophy

The motivation to use lightweight materials in the construction of the automotive structure is the resultant increased fuel efficiency. However, these materials possess certain drawbacks that make it challenging to adopt them into current automobile manufacturing processes. In this dissertation the microstructural response observed in a magnesium alloy, AZ31, and an advanced high strength steel alloy, QP1180, to uniaxial deformation is analyzed and the results are presented.

In AZ31 the required slip modes are not activated at room temperature leading to its low ductility at room temperature. The resulting activity of these twins in response to uniaxial tension is analyzed and its correlations with the microstructure features is reported. Additionally, a neighborhood viscoplastic self-consistent model is developed that will allow more accurate simulation of twin response to outside deformation. Furthermore, activity of slip modes that are usually observed at high temperatures (>200°C) are also observed at lower temperatures (<125°C) and they are compared to the relative twin activity at these temperatures. It is observed that larger grains, with high schmid factors, longer grain boundaries and have misorientation with its neighboring grain greater than 27° are more favorable for twin formation and transmission in the AZ31 microstructure in response to uniaxial tension.

The nature of retained austenite (RA) transformation into martensite that gives QP1180 its enhanced ductility, is not clearly understood primarily because of challenges present in characterization of these metastable RA. Further, a 2 dimensional characterization method does not provide the complete information of the RA grain. These challenges are overcome by characterization of a 3 dimensional volume element using serial sectioning and EBSD followed by reconstruction using DREAM3D. The influence of 3d morphology and orientation direction on RA transformation is studied using as-is and uniaxially deformed samples. A novel shear affinity factor is introduced as a metric to describe the ease of RA transformation under uniaxial tension. The 3d nature of the information collected allows a new classification of disk shape in addition to globular and lamellar shapes for RA. It is found that RA that are low volume laths and have low shear affinity factor transform later compared to disk shaped RA's. Through these guidelines the preparation of a microstructure that is conducive to RA transformation under uniaxial tension is possible.

Keywords: magnesium, QP1180, EBSD, retained austenite, DIC, VPSC, twinning, AZ31

ACKNOWLEDGEMENTS

I would like to express gratitude to the constants in my life namely God, my wife and my family, who have all provided stability for me in this journey. I also want to express my utmost gratitude to my committee chair, Dr. Fullwood, for his untiring confidence and generous actions, many of which would never be known to the larger public. Dr. Miles has provided hope with his contagious optimism that has lifted me up whenever there were research setbacks. Dr. Nelson has always inspired new direction in this work with his pragmatic insights. Dr. Homer has been very encouraging from my nervous beginnings in the graduate program to its completion. Dr. Johnson has provided clarity with his questions and insights at all times. I am thankful for all them for their individual and collective contribution to this academic milestone.

I also want to thank Janelle Harkness who has been consistently gracious along with the rest of the office staff especially Judy and Ryan and many other office secretaries employed over the years. Miriam Busch had guided me through the admission process during her tenure as the graduate advisor and has been a great support to my family with her friendship. Dr. Lowell had taken interest in my application and circulated it to other professors when I initially applied to the program. Dr. Bowden has provided a steady guiding hand in both academic and personal choices. My friends and colleagues in the lab have also constantly assisted my work by providing expertise and levity whenever required.

Part of this research was supported by U.S. Department of Energy (DOE), Office of Science, Basic Energy Sciences (BES), under Award #DE-SC0012587 (computational studies and theory development), and by the National Science Foundation (NSF), under award #CMMI 1404771 (experimental data gathering activities). The other part was supported by Division of Materials Research (DMR) branch of the NSF under award #1507095.

TABLE OF CONTENTS

LIST OF TABLES

LIST OF FIGURES

1 INTRODUCTION

The selection of materials used in constructing automotive structures is an important consideration for improving overall vehicle quality. The automotive structure is exposed to various types of deformation forces during vehicle operation. As such, in conjunction with the geometry of the structure, the material used in building those structure influences the stability and usability of the vehicle. Various advances in material that are used in these structures, have resulted in increase in automobile efficiency for both performance and in its manufacturability.

Additionally, proper selection of material can help reduce the overall weight of the vehicle and influence its fuel economy without negatively affecting its performance. It has been observed that a 10% reduction in weight leads to 8% improvement in fuel economy (Taub et al. 2007). However, a study by the Environmental Protection Agency in 2018 about the trends seen in changes with respect to fuel economy, vehicle horsepower and vehicle weight, shown in figure 1-1, shows that though there are improvements with fuel economy and horsepower, vehicle weight has not been positively changed.

Several candidates that fall into a category of lightweight materials are listed in table 1-1 along with the percentage of mass reduction they can provide when compared to mild steel that is traditionally used in high percentage in the chassis of the vehicle. From these materials, magnesium alloy AZ31B and advanced high strength steel alloy QP1180, are studied in this dissertation. A brief introduction to these two materials is given below.

1.1 Magnesium alloy AZ31B

Magnesium alloys are light weight metals with a density of 1.77 g/cm^3. With such a low density it has higher strength to weight ratio compared to aluminum which is a heavily used lightweight alternative to traditional steel alloys. Among the available Mg alloys, AZ31B is a wrought alloy that is available more commonly compared to the other alloys. It has better room temperature strength-ductility combination and also has high corrosion resistance. It has found widespread application in aircraft fuselages, cell phone and laptop body cases and for other lightweight structural applications. It is available as rods, sheets and plates. The chemical composition of this alloy is Al 2.5-3.5%, Zn 0.6-1.4%, Mn 0.2% and Mg coupled with Si, Cu, Ca, Fe and Ni in small quantities. Though they have high machinability, care should be taken to not ignite them and, forming has to be currently undertaken at high temperatures (> 250° C).

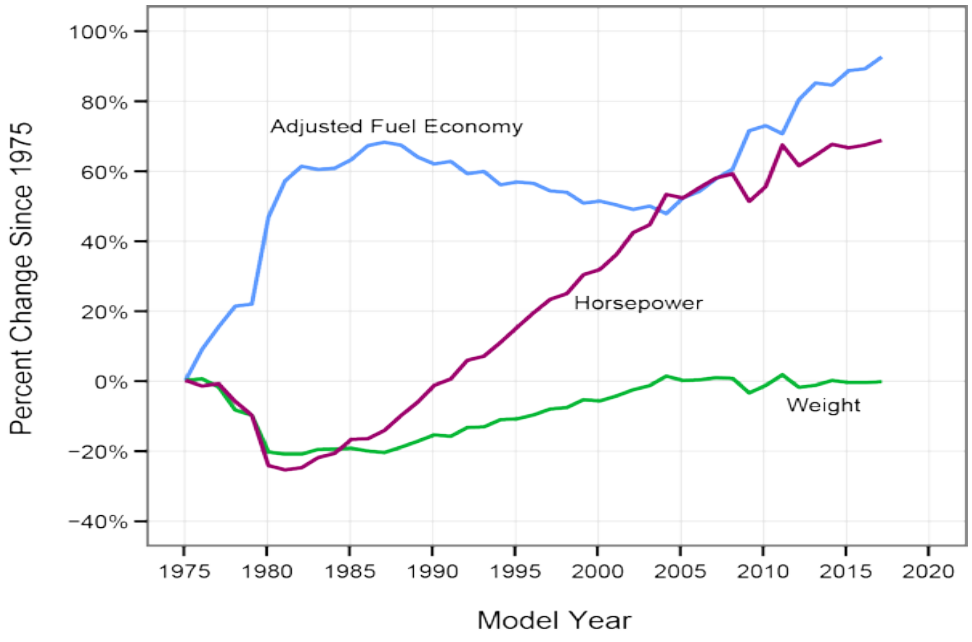

Figure 1-1: Percent change in adjusted fuel economy, weigh and horsepower for automobiles from the year 1975 to 2017. Adjusted fuel economy reflects the real world performance and are not comparable to automaker standards compliance levels and is about 20 % lower than unadjusted fuel economy values (Agency 2019)

Table 1-1: List of general categories of lightweight materials and the percentage of reduction in mass possible for them (Mueller 2016).

Lightweight materials	*% Mass reduction possible*
Magnesium	30 – 70 %
Carbon fiber composites	50 – 70 %
Aluminum	30 – 60 %
Titanium	40 – 55 %
Advanced high strength steels	15 – 25 %

The cause of difficulty in room temperature forming has been identified as because of the lack of the activation of the required number of slip systems as per the Taylor criterion. The hcp structure of Mg limits the activated slip systems to those involving the <a> type or $\frac{1}{3}\langle 11\bar{2}0\rangle$ dislocations within the basal or (0001) plane as it is the only close packed plane available (Agnew and Duygulu 2005). Slip systems in the basal plane does not allow for the extension or contraction of the c axis in the hcp crystal structure at room temperature that is necessary for increased ductility. Other non-basal slip systems such as, prismatic <a> slip and the pyramidal <c+a> slip have been observed to activate at higher temperatures thus leading to good high temperature formability behavior. Instead, deformation along the c axis at room temperature has been found to be accommodated by mechanical twinning in Mg crystals. The $\{10\bar{1}2\}\langle 10\bar{1}\bar{1}\rangle$ twin, which accommodates extension of the c axis is the more easily activated among the two twin systems. The other twin observed is the compression twin $\{\bar{1}011\}\langle 10\bar{1}2\rangle$. The identification of the compression twin has been difficult using current characterization methods because of

their lath like appearance and thus the resolution necessary to identify these twins is difficult to obtain at best.

In this dissertation chapters 1, 2 and 3 are dedicated to understanding the influence of these deformation modes by characterizing the twins and slip systems produced in the microstructure. Subsequently, three hypotheses that are listed below are tested.

1. New correlations between microstructure characteristics and twin activity can be deduced by using a J48 decision tree algorithm within a machine learning framework with additional information from high resolution electron backscatter diffraction.
2. There is increase in accuracy of bulk behavior modelling of twin activity when the influence of twin neighborhood is included.
3. c+a slip provided an important deformation mode in hexagonal materials even at mildly elevated temperatures.

Study of these hypothesis leads to a better understanding of microstructural influences for twin formation and slip activation. Such an understanding helps progress towards achieving better formability in AZ31B by designing the alloy with the proposed microstructure features.

1.2 Advanced high strength steel: QP1180

Third generation advanced high-strength steels (3GAHSS) are promising candidates for lightweighting automotive structures due to their ideal combination of high strength and large ductility. An example of using these AHSS in a car chassis is given in figure 1-2, which shows a body-in-white image for a 2017 Chevrolet Cruz automobile.

The development of Quenched and Partitioned (QP) 3GAHSS (Edmonds et al. 2006) has provided a less expensive way to manufacture a new family of these advanced steels. These steels have a high strength of up to 1400 MPa and ductility of 16-18%. The steel used in this

study is manufactured by Bao Steel for General Motors Lightweight metals research group. This steel has a chemical composition consisting of 0.19 C, 2.8 Mn, 1.6 Si, Fe with trace amounts of Cr, Mo, Ni, Ti, Al and others.

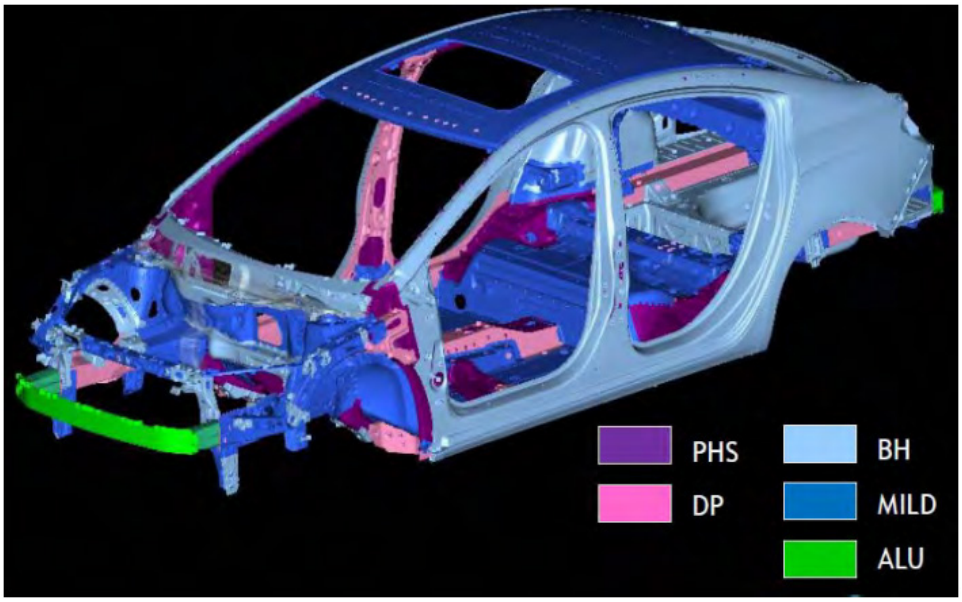

Figure 1-2: Body in white image for a 2017 Chevrolet Cruze showing different types of material used in its construction. From World Auto Steel report titled, Advanced high strength steel application guidelines v 6.0.

QP steels exhibit the TRIP (transformation induced plasticity) phenomenon, via the transformation of austenite, retained in the microstructure, into martensite. The manufacturing process consists of complete austenitization of the steel followed by quenching below the martensite start temperature but above the martensite finish temperature. The final step of partitioning the carbon from the supersaturated martensite to the remaining austenite is accomplished by either keeping it at the quench temperature (one-step) or raising the temperature slightly (two-step) (Speer et al. 2014). The increased amount of carbon in the retained austenite allows it to become stable at room temperature (Santofimia, Zhao, and Sietsma 2011). The complex ferrite-martensite-austenite microstructure and TRIP characteristics contribute to the

combination of high strength and high ductility. While TRIP steels are not new, the fact that the Q&P process can produce these types of metals at a reduced cost is favorable (Diego-Calderon et al. 2016).

However, while the influence of the TRIP effect is generally seen to have a positive effect on material ductility and formability, the detailed relationships between retained austenite (RA) characteristics and the magnitude of the TRIP effect are only partly understood. A guiding principle has been that a controlled rate of RA transformation throughout the deformation process is desirable to achieve ideal hardening rates and thereby obtain maximum ductility (Chiang, Boyd, and Pilkey 2015). But the optimal microstructure for obtaining such a controlled transformation is still to be determined.

Previous research in this area has determined many factors that play a significant role in the stability (and resultant transformation rate) of RA. The carbon content of the RA is one of the important factors, where low carbon concentration in RA grains can cause rapid transformation of these grains into martensite and high carbon concentration in RA grains makes them more stable (Shen et al. 2015; De Knijf et al. 2015). The next important factor is generally agreed to be RA grain size where larger sizes are known to transform faster than small size RA grains. Additionally morphologically, lamellar shaped RA grains are found to be more stable than blocky RA grains (Xiong et al. 2013; Jimenez-Melero et al. 2007). With respect to the influence of the crystallographic orientation of the RA grain, the more oriented it is towards the [111] plane the easier it is for it to transform (Tirumalasetty et al. 2012). Also, the characteristics of neighboring grains, namely if it is embedded in a soft ferrite grain or surrounded by hard martensite laths will dictate if there is any shielding of RA grains against transformation or not (Jacques, Ladriere, and Delanny 2001; Li et al. 2016). Finally when the steel is strained at higher

temperatures there is a reduction in the fraction of RA that is transformed (Wang et al. 2006; Blonde et al. 2012). Out of these factors, carbon content, RA grain size and morphology are generally considered to be most influential on RA trip effect.

With respect to the effect of morphology and orientation on RA transformation in QP1180 the hypothesis, "*a 3 dimensional study about the transformation of retained austenite in QP1180 advanced high strength steel will reveal hidden dependencies that such transformations have with their morphology and orientation"*, is analyzed in chapter 4 of this dissertation. Through this study a more comprehensive analysis about the influence of morphology on the RA transformation rate is attempted. Furthermore, such an analysis is combined with the directionality of the RA grains with respect to the loading axis to decipher any hidden relation between them. Using such relations, a microstructure can be designed that will promote appropriate transformation of RA grains to promote ductility in the metal. This is the motivation behind performing this analysis.

2 EXTRACTING RELATIONS BETWEEN MICROSTRUCTURE FEATURES AND TWIN NUCLEATION USING J-48 MACHINE LEARNING ALGORITHM

Publication citation: Orme, Andrew D., Isaac Chelladurai, Travis M. Rampton, David T. Fullwood, Ali Khosravani, Michael P. Miles, and Raja K. Mishra. "Insights into twinning in Mg AZ31: A combined EBSD and machine learning study." Computational Materials Science 124 (2016): 353-363.

2.1 Chapter Introduction

In this chapter we will be looking to prove the hypothesis that, "*new correlations between microstructure characteristics and twin activity can be deduced by using a J48 decision tree algorithm within a machine learning framework with additional information from high resolution electron backscatter diffraction*".

Machine learning is a suitable statistical analysis approach for mining large quantities of data, such as that from HR-EBSD methods. Already established in various fields as a reliable method for extracting insights and knowledge of relations between attributes in vast databases, machine learning provides a framework whereby complex events, such as deformation twinning, can be connected with local structure and field parameters (Al-Samman and Gottstein 2008; Chapuis and Driver 2010; Chapuis and Driver 2011; Klimanek and Potzsch 2002). In this section, a J48 machine learning algorithm will be employed to create predictive models for twin events in grains, as observed by EBSD, in the form of decision trees. A decision tree framework

is particularly valuable for its interpretability. Using this approach, instances of nucleated and propagated twins in Mg alloy AZ31 will be correlated with microstructure attributes and the relative importance of these attributes in triggering the physical phenomena will be investigated.

Using this proposed machine learning framework, the section aims to achieve the following:

1. Create decision tree models for describing twin nucleation in grains and twin propagation across grain boundaries in the Mg alloy AZ31 by extracting attribute based rules from EBSD data.
2. Rank the physical factors according to influence on the nucleation or propagation of twins.
3. Demonstrate that the proposed approach provides a reliable machine learning framework for mining EBSD data, such that future studies of rare and complex events may be accelerated.

2.1.1 Deformation modes in magnesium alloys

Slip in Mg depends upon a complex array of potential slip systems (Agnew and Duygulu 2005; Koike 2005; Izadbakhsh et al. 2011): basal <a> (2 independent), prismatic <a> (2 independent), pyramidal <a> type I (4 independent), and pyramidal <c+a> (5 independent). Furthermore, plastic deformation can be accommodated by compression twinning (predominantly the six variants) and tensile twinning (mainly the six variants (Christian and Mahajan 1995)). While there is a sufficient number of slip systems in Mg to accommodate the Taylor model, only the basal system and prismatic <a> systems are easily activated at room temperature, providing only 4 independent active slip systems (see Table 1-1). This leaves a

requirement of one additional deformation mechanism for compliance with the Taylor criterion and twin activity can provide the necessary 5th degree of freedom for deformation.

The interplay between slip and twin activity can most simply be described by a CRSS model. In the case of rolled AZ31 sheet, the strong basal texture requires some slip or twinning along the <c> or <c+a> directions in order to accommodate contraction or extension of the c-axis (Jonas et al. 2011). The much higher τ_{crss} values of the <c+a> slip systems relative to those for tensile twins (see Table 1 for ranges of values reported in the literature) indicates that tensile twinning will occur before <c+a> slip to provide the 5th active system in the Taylor model (Koike 2005; Agnew, Yoo, and Tome 2001; Agnew et al. 2003). However, such an approach is not adequate to describe the complex response that is seen in practice.

Table 2-1: Ranges of published τ_{CRSS} values for deformation mechanisms in Mg at room temperature.

Slip System	basal <a>	prismatic <a>	pyramidal <c+a>	$\{10\bar{1}2\}$ twinning	$\{10\bar{1}1\}$ twinning
τ_{crss} (MPa)	4	8-10	80-100	11-12	76-153

The nucleation of a deformation twin in Mg depends upon so many variables that it may be considered a stochastic event (Barnett et al. 2004; Beyerlein, McCabe, and Tomé 2011; Capolungo, Beyerlein, and Tomé 2009; Jonas et al. 2011). In order to begin to unravel the complexity behind the physics of twin deformation, many observations of nucleation events are required (as manifested by several of the studies quoted above). Once sufficient data is available, statistical analysis can be applied in various forms to extract correlations linking the observed structure and applied field variables to nucleation and propagation events.

For example, work by Barnett et al showed that twin nucleation in Mg follows a Hall-Petch relationship, where the required twinning stress increases with smaller grain size (Barnett et al. 2004). Furthermore, Beyerlein et al recently combined atomistic simulations with an extensive EBSD-based study to demonstrate the effects of grain boundary (GB) misorientation and GB dislocation structure on nucleation of twins (Beyerlein, McCabe, and Tomé 2011). The resultant model utilized a stochastic approach to twin nucleation and combined it with a CRSS based model for twin propagation. It proposed distinct weights for the probability of twin nucleation on grain boundaries above and below 45° misorientation, due to the observed tendency of twins to be present at low angle GBs. A similar study by Khosravani (Khosravani et al. 2015) further categorized twin nucleation events at GBs into spontaneous formation of twins (slip-assisted nucleation) and propagation of twins across grain boundaries (twin-assisted nucleation). This section also highlighted the importance of dislocation structure near GBs. The study further demonstrated that twins easily propagate through low angle (15°-25°) GBs and tend to nucleate at high angle GBs (>39°). The different considerations of these various studies and models might be reconciled into one framework via a different approach, in which large data sets are explored using machine learning to reveal correlations to form the basis for model structure and parameters.

Electron backscatter diffraction (EBSD)

Electron backscatter diffraction (EBSD) offers an ideal data collection technique to observe nucleation events, with the ability to scan hundreds of sample points per second (Wright, Nowell, and Basinger 2011). The automated acquisition of EBSD data has been used in materials science for several decades, culminating in tools that achieve common data collection speeds of hundreds of points per second. Such speeds allow for relatively large microstructures to be

quickly and accurately measured (~0.3° resolution in lattice orientation (Wright, Nowell, and Basinger 2011)). The gathered EBSD data can then be processed by commercially available software (e.g. OIM™) to produce other crystallographically significant data related to grain orientation, phase, and morphology. Available information from traditional EBSD techniques also includes grain size distribution, Schmid factors, variations (gradients) in lattice orientation, and GB misorientations.

Additionally, in recent years high resolution EBSD (HR-EBSD) techniques have been developed to extract even more information from the collected EBSD data (Basinger, Fullwood, and Adams 2011; Gardner et al. 2010; Villert et al. 2009; Wilkinson, Meaden, and Dingley 2005). These methods apply cross-correlation techniques to EBSD images in order to measure orientations and relative crystal rotations with even greater angular resolution (0.006°). Using the cross-correlation technique, HR-EBSD is also capable of being used to measure (relative) elastic strain and geometrically necessary dislocation (GND) density at each data point. Both measurements rely on the accurate extraction of the elastic distortion gradient, providing reliable strain and GND fields over large scan areas (Britton and Wilkinson 2011; Kacher, Adams, and Fullwood 2009; Landon, Adams, and Kacher 2008; Wilkinson, Meaden, and Dingley 2006).

With the combination of HR-EBSD data and standard EBSD metrics the mechanisms underlying deformation twinning of Mg can be more fully characterized. Microstructure characteristics analyzed in this section will include grain size, kernel average misorientation, geometrically necessary dislocations, orientation of the c-axis relative to the sheet normal direction, grain boundary misorientations, and the Schmid factors for <a> type slip, <c+a> type slip, and twinning. These attributes provide a broad set of crystallographic measurements that may relate to the nucleation and propagation of twinning in AZ31.

Machine learning

With the abundance of crystallographic information that may affect twinning in AZ31, and given the uncertainty underlying the cause and effect of twin nucleation and propagation, a modeling approach that minimizes assumptions made about the nature of the events under investigation may provide previously unidentified insights into the actual causes of these events. Machine learning, inclusive of various types of data mining developed to find statistical correlations among large datasets, offers one such method of non-discriminatory characterization (Reich and Travitzky 1995; Sha and Edwards 2007). The basic idea of machine learning is to create relationships between user defined attributes (such as microstructure characteristics) and an outcome (such as a twinning event), referred to as a class. This is performed by training an algorithm to predict the resulting class, or outcome, based on a set of training instances containing attribute and class data. The trained algorithm can then be tested against other sets of instances for accuracy, with potential to be deployed as a predictive model if accuracy and precision meet user specifications. By employing this approach to predict twin activity in AZ31, the resulting machine learning models will help confirm whether all important aspects have been incorporated into current statistical Mg twinning models and may give insights into what attributes are missing.

Machine learning has been utilized in various areas of materials science and engineering to develop constitutive relations that establish structure property relationships (Yassar et al. 2010; Perez-Benitez and Padovese 2011; Altinkok and Koker 2006; Haj-Ali et al. 2008). Many such studies treat the resultant machine learning models as a purely black box approach, used to predict an event without consideration to interpreting the decision framework behind the prediction. This is particularly true for certain algorithms employed by these studies, such as

neural networks or Naïve Bayes predictors, which while providing high levels of accuracy, do not have easily interpretable decision hierarchies. In contrast, the primary goal of this section is to create, via machine learning, comprehensible models which describe twinning phenomena in Mg and then use those models to elucidate the physics associated with these events.

Machine learning algorithms can be broken down into three categories: knowledge-based, rule-based, and skill-based (Rasmussen 1983). Knowledge-based learning is equivalent to ab-initio studies and therefore requires a greater prior understanding of the studied phenomenon. Rule-based models however, provide less structured connections while still maintaining a moderate level of accuracy. Finally, skill-based algorithms can be compared to complex curve fitting in which the resultant model provides an easily implementable mathematical equation but may have reduced physical significance and interpretability. For the case of twinning in AZ31, a rule-based method is most suitable, given that there is not enough information to develop an accurate knowledge-based model, and skill-based models would not provide physically interpretable insights into the causes of twinning.

The desire for an easily interpretable rule based classifier led to the selection of the J48 decision tree classifier. The J48 classifier expands the functionality of the C 4.5 algorithm by allowing for classification of continuous variables (Quinlan 1996). J48 produces easily comprehensible decision trees. During training, J48 categorically partitions data to maximize the information gain at each level of the tree structure, where information gain is a mathematically defined property. The result is a hierarchy of attribute (e.g. microstructure property) based divisions that results in the selection of a particular class, or an outcome (such as twin formation), for a given instance. Figure 2-1 is an example of a decision tree created using the J48 classifier. The tree hierarchy is composed of a root, multiple branches, and multiple leaves,

respectively labeled as “R,” “B,” and “L”. The predicted class for each instance is then tested against the actual class for that instance and the accuracy of the tree is evaluated.

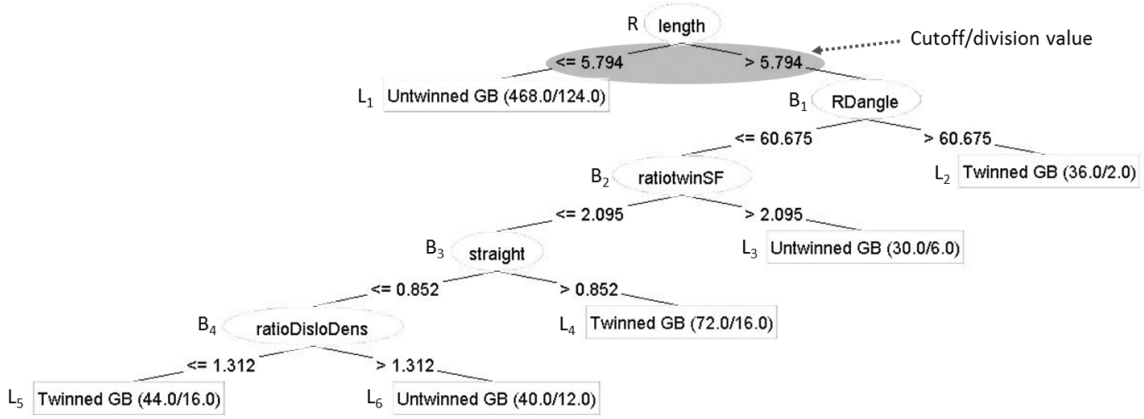

Figure 2-1: A typical decision tree and the associated hierarchy (R: Root, B: Branch, and L: Leaf) present in a decision tree. Note that the values inside the leaves appear in the following format: (# of classified instances / incorrect predictions). The relationships in this tree are provided for illustration and are not part of the investigation at hand.

By definition, attributes found nearer to the beginning of the tree, or “root”, provide greater information gain than subsequent attributes and are thus considered to be more influential in determining the outcome. “Branches” represent subsequent divisions and “leaves” represent a predicted class outcome. Hence smaller decision trees are desirable since they only retain attributes that have the greatest impact on a particular phenomenon. With only the most pertinent features captured, the resultant model becomes more physically understandable.

Thus the model created by a decision tree may be interpreted or applied in several ways:

i) as a model/constitutive relation for the studied event.

ii) as a set of insights into the causes of the event that help focus further research.

iii) as a way to determine/capture more events for further study by predicting when / where critical events will occur.

The tree also provides a framework to systematically increase the data set from which to train the algorithm and thus refine the resulting model. In the case of time-consuming data collection procedures, the potential for a refined data collection method is desirable as it has the ability to intelligently guide data collection towards areas of interest, as defined by the information contained in the decision tree. Such an approach to refined data collection is an area of ongoing research and beyond the scope of this section.

2.2 Methodology

The material studied in this research was a 3 mm thick cold rolled and annealed AZ31 Mg alloy plate with an initially twin-free microstructure. Specimens were prepared as 3mm x 4mm x 3mm square prisms, cut from a fully annealed AZ31 plates, using wire EDM to minimize the amount of deformation on the sample surface. The samples were then prepared for EBSD study by mechanical polishing using suitably sized diamond abrasives followed by an OP-S colloidal silica slurry polish. Finally, the sample was etched with a solution of 60% ethanol, 20% distilled water, 15% acetic acid and 5% nitric acid. Using a focused ion beam, platinum fiducial marks were deposited on the specimen surface to measure approximate 2-dimensional strain in the scan area (Khosravani et al. 2015).

The first specimen was compressed along the rolling direction (RD) up to ~3% strain, and the second specimen was strained slightly further to ~3.5%. This strain was chosen because it was the point at which there was sufficient twin nucleation and propagation for detailed analysis using machine learning, based on prior work (Jon Scott 2012). EBSD scans were carried out on an FEI-Helios NanoLab^{TM} 600i SEM equipped with OIM^{TM} data acquisition software and a high-speed Hikari^{TM} camera. A step size of 300 nm was selected for two scan areas of 84 x 84 μm^2 on the first sample and 70 x 270 μm^2 on the second. Subsequent post processing of data

utilized OIM™ Analysis, Matlab™, and OpenXY (open source HR-EBSD software from Brigham Young University) to organize attributes for input into the machine learning environment. The extracted attributes, their origin, and a brief explanation are listed in Table 1-2.

Table 2-2: Input attributes (parameters) for machine learning. Check marks indicate attributes utilized as inputs for creating each model (nucleation or propagation). Highlighted check marks indicate the important microstructural features as found by each machine learning model. (N: nucleation, P: propagation).

Attribute *(Abbreviation in decision tree)*	Description	Source	Model N	Model P
Grain size *(SIZE)*	– Equivalent diameter. The diameter of a circle with the same area as the measured grain	OIM Analysis	✓	
Neighboring grain size *(NBRSIZE)*	– Average neighbor grain size		✓	
Relative grain size *(RELSIZE)*	– Grain size divided by neighboring grain size		✓	
Number of neighbors *(NUMNBRS)*	– Number of neighboring grains		✓	
Deviation of c-axis from RD, TD, and ND *(RDMISO, NDMISO, TDMISO)* *	– Smallest angle of misorientation		✓	✓
Kernel average misorientation *(MISO)* *	– Average misorientation of directly neighboring points (with 5° cutoff)		✓	✓
Schmid factors (SF) of basal <a> and pyramidal <c+a> slip systems *(BASALSF, CASF)**	– Maximum value of each slip system taken as a grain average		✓	✓
Schmid factors of $\{10\bar{1}2\}\langle 10\bar{1}\,\bar{1}\rangle$ tensile twins *(TWINSF)*	- Maximum value, taken as a grain average (also considers the possibility of negative values)	Matlab	✓	

Table 1-2 continued

Attribute *(Abbreviation in decision tree)*	Description	Source	Model N	Model P
Ratio of twinning Schmid factor to <c+a> Schmid factor *(TWINCASF)**	– Maximum SF for twinning divided by max SF for pyramidal <c+a>		✓	✓
GB misorientation *(GBMISO)*	– Rodriguez misorientation			✓
GB length *(LENGTH)*	– Length along measured GB segment			✓
GB straightness *(STRAIGHT)*	– Average distance of the measured boundary from a straight line connecting the boundary endpoints			✓
Approximate GB orientation *(RDANGLE)**	– Angle between the GB trace and RD			✓
Local dislocation densities *(LOGDD)**	– Grain average of sum of Nye tensor terms	HR-EBSD	✓	✓

**Value for attribute recorded on both sides of a given grain boundary in addition to the average difference in values over the boundary – leading to multiple attributes relating to each of these items. They are labeled in decision trees with the prefix MAX, MIN, or DIFF preceding the attribute label given in Table 1-2.*

The analysis presented in this section calls for two separate models to be created, one for nucleation of twins in grains and another for propagation of twins across grain boundaries. For this study, a nucleation event was classified by identifying at least one twin in a grain (i.e. both twins that spontaneously formed in a grain and twins that propagated into the grain from a neighboring grain). A propagation event was defined when at least one twin was present on either side of a given GB. The nucleation model took into consideration attributes within a grain, but ignored GB morphology. The propagation model, on the other hand, focused on parameters relating to GBs.

Several attributes were selected to represent morphological data (e.g. grain size, number of neighbors, neighboring grain size, GB length). Attributes relating to feature size play a large role in both current Hall-Petch type models (Barnett 2007a; Barnett et al. 2004) and stochastic models (Beyerlein, McCabe, and Tomé 2011; Beyerlein et al. 2010).

Other attributes (such as GB trace orientation, GB straightness, grain orientation relative to loading direction, Schmid factors, kernel average misorientation and the related metric of GND density) may affect strain compatibility, incentive to slip or twin, and information regarding localization of deformation. Kernel average misorientation (KAM) and GND content, measureable by HR-EBSD, indicate strain localization in a material, potentially triggering twin activity. The Schmid factor of a particular slip or twin system also serves as an indicator of the likelihood of the relevant activity.

The remaining attribute of GB misorientation not only reflects morphology (local relative orientations), but also partially reflects energy associated with GBs. This also relates to GB defects, and has already been linked to twin nucleation and propagation (Beyerlein, McCabe, and Tomé 2011; Khosravani et al. 2015).

The metrics collected were gathered for grains that did not twin and grains that twinned, also referred to as parent grains. Grains and grain boundaries near the edge of the scanned area were excluded from consideration due to a lack of complete information for various local attributes (such as grain size).

Once the previously described attributes were collected for each grain and grain boundary, they were organized into a data structures suitable for input into a machine learning program. This study used a publicly available machine learning package, WEKA, for the data mining process (WEKA 2010). A J48 decision tree classifier was then chosen to find correlations

between input parameters and twinning (Quinlan 1993). The algorithm employs a method that increases the information gain of the data as it is partitioned at each node of the tree. Information gain for J48 is calculated by the following relations:

$$G(S,A) = E(S) - \sum_{v \in Values(A)} \frac{|S_v|}{|S|} E(S_v) \quad (2\text{-}1)$$

$$E(S) = \sum_{i=1}^{c} -p_i \, log_2 \, p_i \quad (2\text{-}2)$$

In these equations S is the total set of instances being considered, S_ν is the subset of S with value ν, A is the attribute under consideration, ν is a particular value of the considered attribute A, c is the set of possible outputs (these being 'twin' or 'no twin' for this study) for value ν, and p is the probability of instance *i* having value ν. Equation (2-1) calculates the information gained with selection of a particular attribute and equation (2-2) calculates the entropy of moving toward that attribute. When the information gain for an attribute is higher than a user defined threshold and the entropy required for moving towards this attribute is lower than the entropy required for moving towards other attributes, the algorithm selects this attribute as most suited for forming a branch or root in the decision tree.

In this study the data used to train the algorithm indicates, using a class variable, whether a grain nucleates a twin or not for the first study (nucleation), and whether a grain boundary propagates or blocks a twin for the second study (propagation). Relevant roots, branches and leaves of each decision tree are labeled "R," "B," and, "L" respectively in this section.

Additional constraints were placed on the machine learning algorithm to avoid arriving at an overly complicated model; these include applying a confidence factor of 0.25 (an algorithm parameter) and disallowing any leaf with less than two instances. The confidence factor value

sets a limit on the minimum acceptable information gain for a branch to be included in the tree. Its values are greater than zero, with larger values requiring less information gain per branch.

The two decision trees (for nucleation and propagation) were initially trained and validated using data from a single scan. They were subsequently tested on a second larger scan. In order to create a valid model using the initial data set, standard 10 fold cross-validation techniques were applied to the decision tree algorithm. Cross-validation is a proven machine learning technique where the data is split into 10 stratified subsets called folds. One fold is removed from the dataset, and the other 9 are used to train the classifier. The removed fold is then used to test the model created by the other 9. This is repeated with each of the 10 folds used to test against the model formed by the other 9 and a final average model is generalized from the results. A minimum of two instances per leaf was also required as an additional precaution to avoid the effects of over fitting (Sha and Edwards 2007; Tompos et al. 2007). Over fitting is an occurrence in machine learning that can cause a model to have poor generalization capabilities (i.e. the model only accurately describes the relatively small subset of training instances).

The models generated for this study used detailed inputs from 104 grains to build the nucleation model and 130 grain boundaries to create the propagation model, from the first specimen described above. Among the 104 grains used in the creation of the nucleation model, 38 had detectable twins present. The nucleation model took into account a total of 13 attributes, taken from Table 1-2, including grain size, number of neighboring grains, average size of neighboring grains, relative size of a grain compared to its neighbors, kernel average misorientation, deviation of the c-axis from the RD, TD, and ND, basal Schmid factor, pyramidal <c+a> Schmid factor, tensile twin Schmid factor, the ratio of the twin Schmid factor to the pyramidal <c+a> Schmid factor, and $\log_{10}$ of dislocation density measured by HR-EBSD.

Of the 130 observed grain boundaries that came in contact with one or more twins, 30 were found to facilitate twin propagation. The propagation model took into account a total of 19 attributes, based on attributes listed in Table 1-2. Included were kernel average misorientation, basal Schmid factor, the ratio of the twin Schmid factor to the pyramidal <c+a> Schmid factor, $\log_{10}$ of dislocation density measured by HR-EBSD, and deviation of the c-axis from the ND. These 5 attributes were calculated on both sides of a given grain boundary along with the difference between them. GB straightness, approximate GB orientation, GB length, and GB misorientation were also included. The second dataset contains 1239 grains and 1127 GBs. This data was used to test the models created with the smaller dataset, giving insight into the accuracy of the models when applied to a more generic dataset.

The overall accuracy of each model was assessed as the total number of correct predictions divided by the total number of instances used to create the model. Each model has two accuracy percentages, the first is the accuracy of the model against the training data, or the smaller dataset, and the second is the accuracy of the model when tested against the larger dataset, which was not used in training. The second accuracy suggests the feasibility of the model in being deployed for use against other independent datasets.

Maps of correct and incorrect predictions were also created to visually represent model accuracy in the microstructure. Attributes found to be influential were compared with literature on twinning in Mg to either confirm previous findings or suggest new areas of investigation. The number of correct predictions versus incorrect predictions at each leaf was also evaluated

2.3 Results

2.3.1 Twin nucleation in grains - results

The model created for nucleation of twins as a function of microstructure attributes is

shown in figure 2-2. In testing the observed microstructure against the created decision tree, 86.5% of the 104 grains and 75.1% of the 1239 grains were correctly categorized by the model is either twinning or not twinning. This decision tree is relatively shallow, with only five branches (decision points) and six leaves (end points). As seen in figure 2-2, only 4 attributes were needed to accurately define twin nucleation within a grain.

They are, ranked in order of importance:

1. grain size.
2. basal Schmid factor.
3. dislocation density.
4. c-axis to ND deviation.

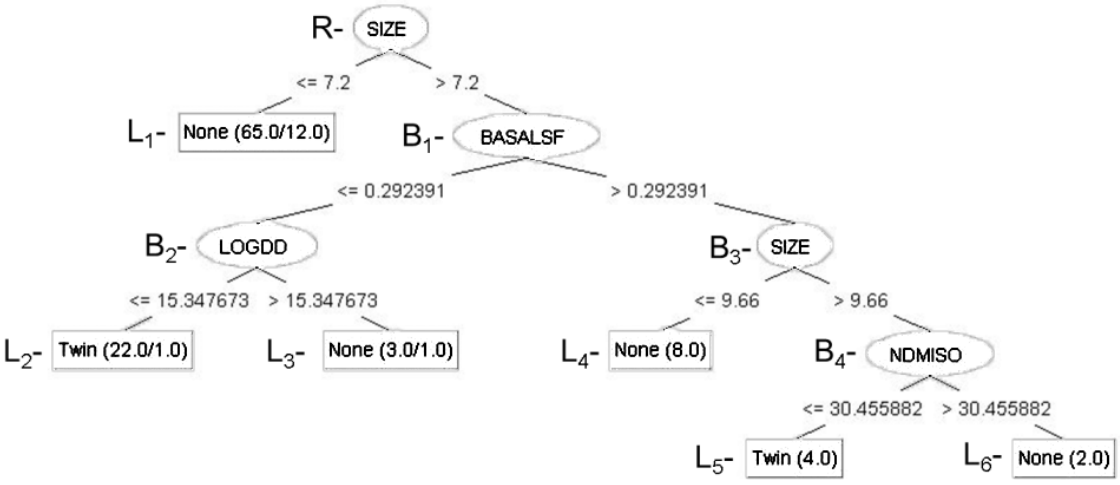

Figure 2-2: Decision tree for characterizing twin nucleation within an individual grain. Labels R, B and L index the root, branches and leaves, respectively. Attribute labels used in the tree are defined in Table 1-2.

The presence of grain size in the machine learning model coincides with the findings of many researchers (e.g. (Barnett et al. 2004)). Furthermore, the location of grain size at the "root" of the tree, and a further appearance at branch B3 within the tree, emphasize its fundamental

importance. The next attribute of importance in the decision tree is basal Schmid factor; its appearance is in line with the findings of others, as it indicates whether a grain is “hard” or “soft”, and therefore prone to twinning (e.g. (Khosravani et al. 2015)). The dislocation density and c-axis to ND deviation might be considered new findings pertinent to the twinning phenomenon in Mg. Influence of c-axis misorientation on twinning has previously been proposed for statistical models, but the previous study focused on the somewhat different attribute of misorientations between the c-axis of neighboring grains (Beyerlein et al. 2010). These attributes appear near the end of the tree, indicating that they do not provide as much information gain as the other attributes, such as grain size. However, if the lower attributes are removed and replaced with random class assignments, the accuracy of the tree on the training data drops by approximately 10%; this suggests that grain size is dominant, but not the exclusive factor in twin formation.

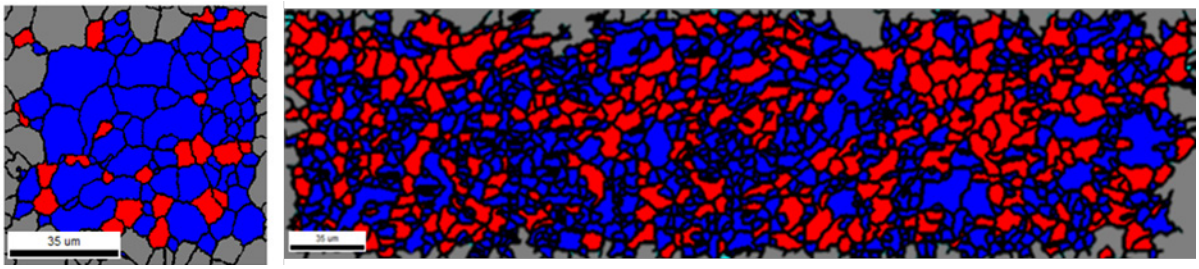

Figure 2-3: Error maps of decision tree for predicting twinning in individual grains. Microstructure used to build model, 104 grains (left) and test generalization,1239 grains (right). Correct predictions (blue) and incorrect predictions(red) are shown except for edge grains (gray) which were excluded due to incomplete information.

Additionally, the validation of the model is visually ascertained by mapping the predictions made in the decision tree onto the grain structure tested (see figure 2-2). Several insights into the model are made clear by the maps in figure 2-3. The first is that the model appears to better predict twin activity in small area grains than large grains, which is likely due to

the uneven distribution of instances in the training data. The uneven distribution of training instances can result in a final model that is slightly biased, as seen in the difference in accuracy between small and large grains. It is also seen that misclassified grains are often clustered together, suggesting a limitation in the current model. Twinning is known to often form in localized bands; by using grain based attributes in the model as opposed to local area attributes, this inter-granular interaction is not accounted for.

2.3.2 Twin propagation across grain boundaries – results

The decision tree model for twin propagation is shown in figure 2-4. The model correctly predicted whether a twin propagated across a given grain boundary (GB) in 125 GBs out of the 130 GBs (96.1%) used to create the model, and in 851 GBs out of the 1127 GBs (75.5%) used for testing the model. However, the higher accuracy came with an increased depth of decision tree. The nucleation of twins within grains has a relatively small decision tree (5 branches and 6 leaves), whereas the model for twin propagation has 11 branches and 12 leaves i.e. approximately twice the size of the prior tree.

In the propagation decision tree, 9 of the possible 19 distinct attributes are present. They are:

1. GB length
2. GB misorientation
3. Minimum twin to $\langle c + a \rangle$ Schmid factor ratio
4. Difference of twin to $\langle c + a \rangle$ Schmid factor across the GB
5. Minimum basal Schmid factor
6. Difference of basal Schmid factor across the GB
7. Difference of kernel average misorientations across the GB

8. The approximate angle of GB on the sample surface relative to the RD
9. The maximum basal Schmid factor

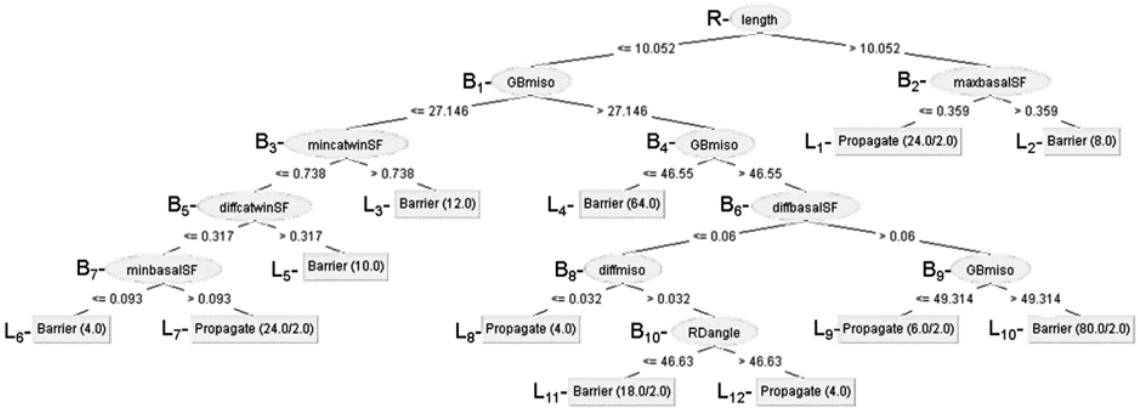

Figure 2-4: Decision tree for characterizing twin propagation across grain boundaries. Attribute labels used in the tree are defined in Table 1-2.

Several of the attributes in the model reflect findings from previous work. For example, GB misorientation was considered by both Beyerlein et al (Beyerlein, McCabe, and Tomé 2011) and Khosravani et al (Khosravani et al. 2015). The basal Schmid factor appears several times in the tree, confirming the finding by Khosravani et al. that showed the correlation between twin nucleation and basal dislocation buildup at a grain boundary. Other attributes such as GB length capture multiple aspects of prior research such as the grain size effect observed by Barnett (Barnett et al. 2004) and the statistical nature of twinning at a boundary observed by Beyerlein, since larger boundaries have more potential twin nucleation sites.

In order to visualize the accuracy of the GB propagation model, a different type of map is required from that shown in figure 2-3. In this case, twin boundaries were colored as either allowing or blocking propagation. Incorrect predictions in either case were highlighted as seen in figure 2-5.

2.4 Discussion

2.4.1 Twin nucleation in grains – analysis of model

In analyzing the results and accuracy of the decision tree models, the potential benefits include both a twin prediction model (in this case, provided by the decision tree), and detailed insights into microstructure attributes that contribute most to twin activity. An analysis of the grain nucleation model figure 2-2 reveals a hierarchy of attributes that influence twin formation. The detailed correlations between these attributes and twin activity can be explored in more depth using standard statistical analysis. The relative frequency of twinning across the range of values of selected attributes is shown in figure 2-6 revealing functional dependence which is not entirely captured in the decision tree, and aids the discussion of the overall performance of the decision tree approach.

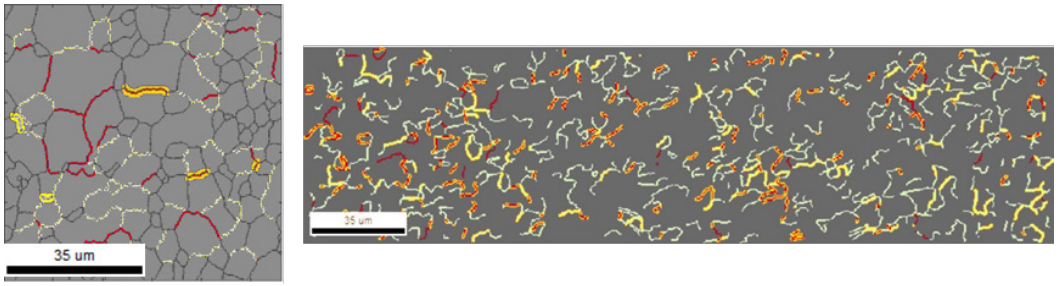

Figure 2-5: Error maps of the decision tree for predicting twin propagation across grain boundaries. Microstructure used to build model, 130 GBs (left) and test generalization, 1127 GBs (right). GBs that were predicted to allow propagation of twins are shown in red while those that predicted barriers to twin propagation are pale. Incorrect prediction assignments are highlighted in yellow (appears orange in the right image). Grain boundaries that do not intersect twins are displayed in black.

The most critical contributor to twin formation within a grain is grain size, at the root (R) of the decision tree. At this point the tree splits into a terminal leaf (L_1) and a branch (B_1). This initial division on the tree, dividing grains that are greater or smaller than 7.2 μm, illustrates the

difficulty of twin nucleation in relatively smaller grains, consistent with the Hall-Petch approach on the twinning shear stress described by Barnett (Barnett et al. 2004). This also aligns with the stochastic view of twinning (Niezgoda et al. 2014), where smaller grains would be less likely to nucleate twins due to fewer available nucleation sites. A more detailed view of this relationship can be seen in figure 2-6c, where increasing grain size generally results in increased likelihood of twinning. However, leaf L_1 has a relatively high error (12 of 65 predictions were incorrect), highlighting one negative aspect of the decision tree approach, representing non-linear data using discrete divisions. For example, figure 2-6c displays a somewhat non-linear relationship between grain size and twin occurrence; however, the decision tree creates a discrete division based on a single grain size to segregate grains that are more likely to twin from those that are less likely to twin. The non-linear relationship can be partially incorporated into the tree by the appearance of multiple branches containing the same attribute (as in branch B3 in this tree). More sophisticated machine learning algorithms can be used to better capture the non-linear functional dependence (for example, neural networks); however, such algorithms are not as good at quantifying the relative importance of the attributes and thus at clarifying the physics underlying the phenomena of interest.

Another source of error relating to grain size correlations is inherent in the nature of the data being used. EBSD infers a grain size from a 2D slice of the grain. While on average, stereological values of grain size have been shown to be correct (Wright 2010), there will be various cases when a large grain is assumed to be small due to the fact that it has been sliced near to one end. This type of error will reduce as the size of the data set increases.

The B_1 branch in figure 2-2 partitions the remaining instances into two sets based upon the basal Schmid factor being greater or less than ~0.29. Once again, the relevant chart in figure

2-6a displays a more complex relationship between Schmid factor and twin probability; nevertheless, the simple cutoff value approach in the model highlights the fact that lower Schmid values correlate with a higher tendency to twin, potentially owing to the lack of appropriately oriented basal slip systems to accommodate strain.

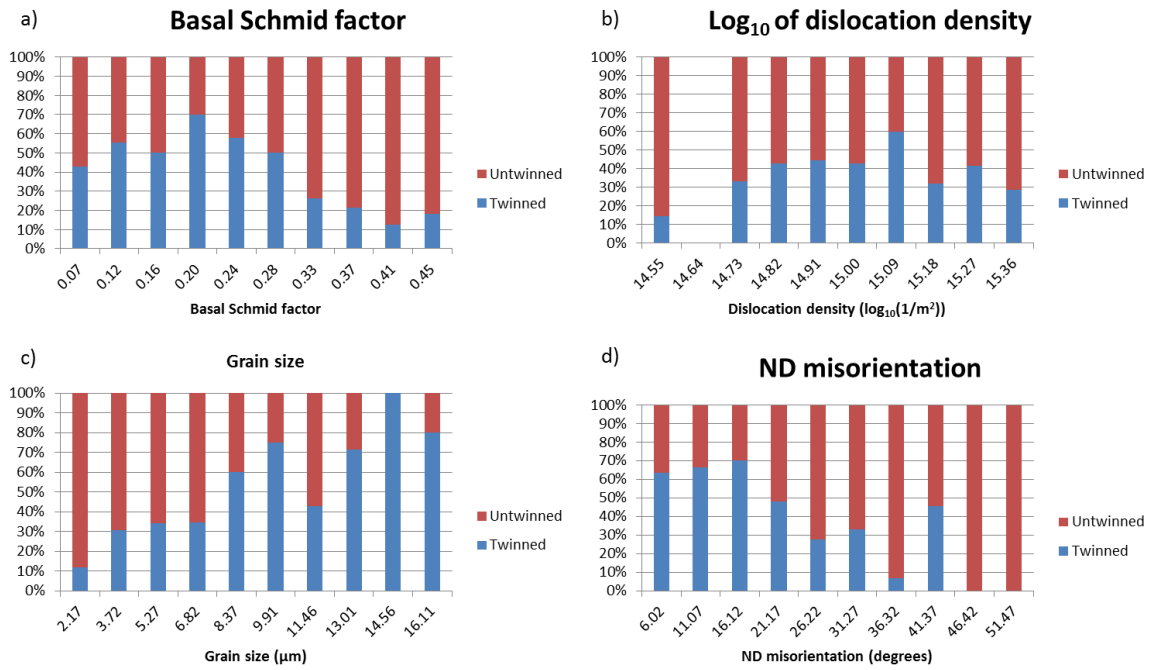

Figure 2-6: Bar charts of relevant features used in the decision tree for the twin nucleation model: basal Schmid factor (a), dislocation density (b), grain size (c), and ND deviation from the c-axis (d).

Of lesser influence in the production of twins is dislocation density, as apparent at branch B_2, immediately below the basal Schmid factor branch (B_1), indicating a correlation between lower dislocation content (<2.23e15 m^{-2}) and twin activity. This is presumably because of the presence of greater slip activity which reduces the necessity for strain accommodation by twinning. Such dependence may not have been immediately apparent from a simple view of the relationship between dislocation density and twin activity, as seen in figure 2-6b. The strong correlation comes

to light only after the small grains and those with low basal Schmid factors are filtered out using the decision tree approach.

The additional consideration of c-axis to sample-ND deviation contributes the last unique attribute found in the machine learning model, and is found in branch B_4. This attribute is used as a measure of how strongly aligned a grain is with the basal texture found in the tested samples (i.e. distinguishing "hard" and "soft" grains). The final leaves (L_5, L_6) of the model indicate that grains which are closer to the basal texture tend to twin more, presumably because of the need to accommodate c-axis expansion by means other than <a> type slip. Again, the statistical analysis in figure 2-6d provides further insight into the nature of this correlation by illustrating the trend that lower ND misorientations (stronger basal orientation) twin more frequently.

2.4.2 Twin propagation across grain boundaries - analysis of model

While the model presented for finding grains containing twins was relatively simple, the decision tree for characterizing propagation of twins across GBs figure 2-4 involved a larger number of parameters and was more complex. This is also highlighted by the statistical correlations of underlying dependencies for various attributes, as shown in figure 2-7. Therefore, the focus of the analysis of this model will not be to explain the tree in its entirety but to extract as many reliable conclusions as possible.

The first attribute that appears at the root of the decision tree (R) for propagation is GB length, and attribute that is not always considered in twin models. However, clearly larger GB areas statistically increase the probability of twins nucleating or propagating across a boundary; longer grain boundaries propagate twins more readily than their shorter counterparts (≤10.1 μm).

The next most important attribute in the decision tree is GB misorientation (B_1), which had been previously studied by other researchers (e.g. (Beyerlein, McCabe, and Tomé 2011)). In

the machine learning model, GB misorientation appears at three distinct branches (B_1, B_4, B_9), pointing to a more complex relationship between misorientation and twin activity than might previously have been captured by models in the literature. In general, grain boundaries with lower misorientation are more likely to propagate twins while higher misorientation grain boundaries serve as barriers to twin propagation. The machine learning model identified 27.1° as the approximate threshold angle of misorientation below which propagation is favored, showing good agreement with the 25-39° found by Khosravani et al (Khosravani et al. 2015). Note that this apparent correlation may also be due to the fact that hard grains neighboring soft grains tend to have high angle boundaries, and that, strain accommodated in the soft grain by slip must be accommodated in the hard grain by twins (see the discussion in (Khosravani et al. 2015)). However, the overall effect of GB misorientation on twin propagation is fairly complex, as seen in figure 2-7b. This complexity is expressed in the decision tree model by the reoccurrence of GB misorientation. It is interesting to note the presence of spikes in twin propagation instances in figure 2-7b. While not investigated in this work, these could correlate with special grain boundary types.

Another significant attribute in the machine learning model is the basal Schmid factor near grain boundaries (B2, B6, B7). As presented in the decision tree, the maximum basal Schmid factor is pivotal in deciding whether longer grain boundaries block or propagate twins. This can also be visualized to some extent via the basal SF plot in figure 2-7c. According to B2, when the maximum basal SF on either side of a boundary is less than ~0.36, twins tend to propagate. If basal slip systems cannot easily accommodate the stress state caused by a twin on the opposing side of a GB, then twinning may occur in order to accommodate that stress. Previous research has demonstrated the stress rise at GBs and triple junctions, using finite

element modeling, for various materials and triple junction configurations (Yue 2003; Fallahi and Ataee 2010). In these studies, the stress at a triple junction has been shown to be as much as 30% higher than the average stress in the grain. Referring back to Table 1-1 this increase in stress may accommodate the transition from activation of prismatic slip (8-10 MPa) to activation of tensile twinning (11-12 MPa). Furthermore, Koike (Koike 2005) discussed the formation of twins due to stress concentration and Barnett (Barnett 2007b) showed that twins intersecting other boundaries can lead to void/crack nucleation which also serves to illustrate the increased stresses at these locations. In brief, the stress concentration caused by a twin intersecting a GB may be sufficient to increase the local stress above the threshold for tensile twinning, causing that twin to propagate across the boundary.

Other attributes present in the decision tree include the ratio of twin Schmid factor to <c+a> Schmid factor (B_3, B_5), kernel average misorientation (B_8), and the average angle between the GB and loading direction (B_{10}). The ratio of Schmid factors (B_3, B_5) provides information as to whether incompatibility will exist at a GB which would then need to be accommodated by a twin. Smaller differences between these ratios across a GB may encourage twins to propagate, since both grains are more likely to twin than activate <c+a> slip. Additionally, kernel average misorientation (B_8) has been used by some researchers as an estimate of dislocation activity (Marion Calcagnatto 2010). In the decision tree smaller differences across a GB tend to result in propagation of twins, and larger differences serve as barriers. Similar observations were made by Khosravani that suggested that dislocation pileups can correlate with poor twin propagation as well as spontaneous twin nucleation (Khosravani et al. 2015). The final morphological measure of grain boundary trace angle (B_{10}) seems to show that boundaries more perpendicular to the RD will propagate twins, likely due to the increased area across which the incoherent twin boundary

spans. This relationship cannot be seen clearly in figure 2-7d but is extracted through the machine learning algorithm pointing to a potential advantage of the method presented in this section.

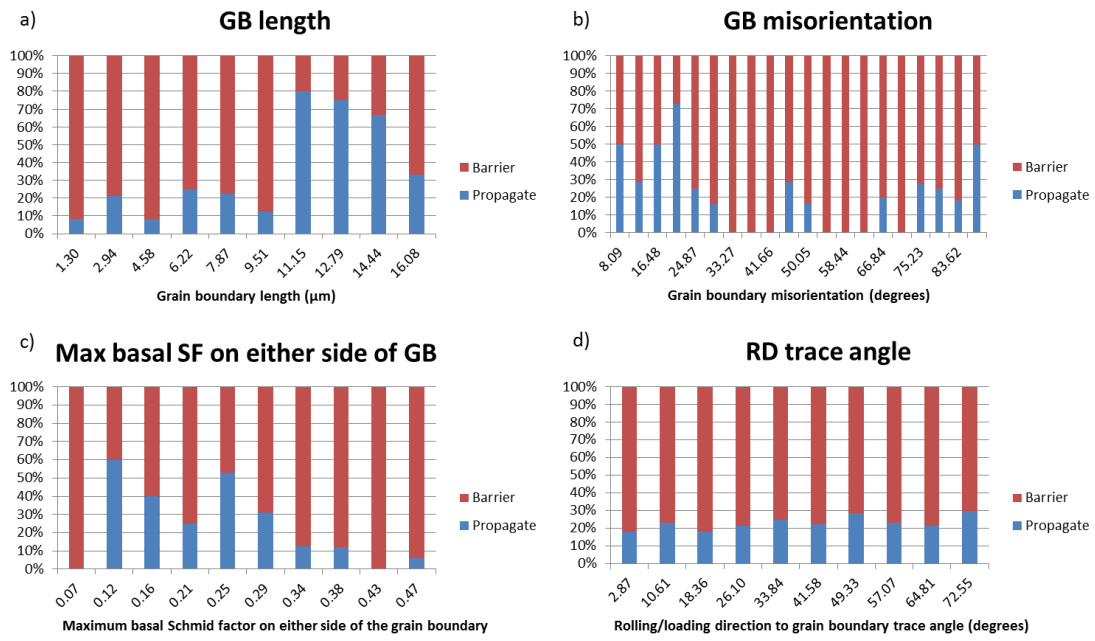

Figure 2-7: Bar charts of relevant features used in the decision tree for the twin propagation model: grain boundary length (a), grain boundary misorientation (b), maximum basal Schmid factor (c), and the angle between the grain boundary trace and loading direction, RD (d).

The decision tree is very accurate for the original data set from which it was derived, but less so for the larger test data. This may be due, in part, to the large size of the tree. Large trees / models tend to increase the likelihood of over fitting which limits the models ability to accurately characterize generalized data sets. Regardless of the potential errors in this model, attributes nearest to the root of the tree would most likely remain the most important across more general datasets, thus maintaining the relative accuracy and interpretation of the model.

2.4.3 Machine learning framework - discussion

When selecting the decision tree algorithm, it was understood that it would provide a rule-based description of the studied events related to twinning in AZ31, and not a knowledge-based description. Knowledge based machine learning methods, such as neural networks, tend to produce more accurate models, but require prior knowledge about the event studied. The methods employed by using J48 do not require previous knowledge about the events and thus cannot create the more complex, yet more accurate, knowledge based results. While trade off of accuracy might be considered a weakness of this machine learning framework, it is in fact an advantage since understanding of twin nucleation and propagation is not sufficient to create a model based on prior knowledge. The idea of extracting structure/ phenomena relations and ranking the importance of different structure attributes, without prior understanding of the physics, is perhaps the greatest benefit of using this rule-based machine learning approach. For example, if one considers a scenario where no previous work had been done to study twinning in Mg, then the results of machine learning could have focused subsequent studies on the highlighted individual attributes found in the decision trees. Even as prior knowledge was considered here, modest insights beyond current models have been identified for deformation twinning in AZ31.

The difference in accuracy between the small and large dataset should be noted. The models did not perform as well on the larger datasets, likely for several reasons. First, the model is biased towards the small dataset, as it was used to train the model. Second, small differences in strain or texture between the samples could greatly affect their accuracy. Despite the differences in accuracy, the 75% accuracy of the model in comparison to the large dataset

confirms that the framework produces robust models that have potential to be deployed for use with new data.

For example, one significant attribute found using the machine learning framework is the deviation of the c-axis from the sample ND. This new knowledge could lead to a more in-depth study to observe highly non-basal grains in a mostly basal textured material in an effort to come up with a measure of strain incompatibility that would then help explain twinning in these grains.

Another potential application of machine learning as it applies to the findings of this section is the opportunity to refine and accelerate microscope-based studies on twinning in Mg AZ31. The knowledge gained via the machine learning method gives future researchers the ability to quickly select areas of interest (e.g. regions where twin nucleation is probable) and capture high quality data in these areas. The model may also be applied to observe twin nucleation at its earliest detectable stages by looking for the highlighted attributes at lower levels of global strain. Such tools could serve to help future studies of any complex materials phenomenon observable by EBSD.

2.5 Conclusion

Twin formation within grains and twin propagation across grain boundaries in Mg alloy AZ31 was studied using a machine learning framework (J48 decision tree), which extracted attribute based rules. Models emerging from the study were 86.5% accurate for predicting twin nucleation and 96.1% accurate for predicting twin propagation across grain boundaries against the cross validated training set of 104 grains. The accuracy of the models against an independent test set was 75.1% for twin nucleation in 1239 grains and the twin propagation model was 75.5% accurate on 1127 GBs. The compression strain and distribution of twinned vs untwined instances

were slightly different between the test and model samples, which may have led to discrepancies between the accuracies between the two datasets.

The important observations associated with twin nucleation on the grain level, in order of the greatest to lowest relevance, include:

- increased twin nucleation in larger grains (>7.2 μm)
- decreased twin nucleation in grains with maximum basal Schmid factors above ~0.29
- decreased twin nucleation in grains with average dislocation densities above 2.23e15 m^{-2}
- increased twin nucleation in grains where the angular deviation between c-axis and sample ND was less than 30.5°

The important observations associated with twin propagation across a grain boundary, in order of relevance include:

- increased twin propagation across GBs with a length greater than 10.05 μm
- increased twin propagation at GB misorientations <27.1o
- decreased twin propagation for GBs where the maximum basal Schmid factor exceeded 0.359
- increased twin propagation across GBs where the difference between the ratio of twin Schmid factor to <c+a> Schmid factor was less than or equal to 0.317
- decreased twin propagation across GBs with a difference between kernel average misorientation greater than 0.032o
- decreased twin propagation across GBs where the average angle between the GB and loading direction was less than or equal to 46.63o

The combination of these attributes provide the greatest overall information gain of the available features and help understand the physical processes associated with tensile twinning in

AZ31. Furthermore, the findings of this section stand in agreement with work done by previous researchers (grain size corresponds to Hall-Petch/Barnett models , boundary length corresponds to Beyerlein (Beyerlein, McCabe, and Tomé 2011), and GB misorientation corresponds to both Khosravani (Khosravani et al. 2015) and Beyerlein (Beyerlein, McCabe, and Tomé 2011)) while building upon it with new insights. These additional insights provide a deeper understanding of some of the previously hidden details affecting twinning in AZ31, leading to potentially more accurate models in future work.

In conjunction with the findings on twinning in this Mg alloy, a machine learning framework for utilizing EBSD data has been adopted that can be used to analyze a variety of complex phenomena. The benefits of this technique are two-fold. They are; i) underlying processes, or microstructural features, behind studied events can be quickly revealed, and ii) continued study of a phenomenon will be aided by the ability to quickly refine data collection to areas of interest in a microstructure. The framework presented in this study is not limited to twinning in Mg or its alloys but extends to the broader set of crystalline materials. Ultimately this technique has potential for analyzing complex metallographic phenomena rapidly, which will allow for acceleration in researching links between microstructure and material properties

3 DEVELOPMENT OF A NEW VISCO PLASTIC SELF-CONSISTENT MODEL THAT CONSIDERS THE NEIGHBORHOOD OF THE GRAIN TO PREDICT TWIN NUCLEATION AND TRANSMISSION IN AZ31B

Publication citation: Chelladurai, Isaac, Devin Adams, David T. Fullwood, Michael P. Miles, Stephen Niezgoda, Irene J. Beyerlein, and Marko Knezevic. "Modeling of trans-grain twin transmission in AZ31 via a neighborhood-based viscoplastic self-consistent model." International Journal of Plasticity 117 (2019): 21-32.

3.1 Chapter Introduction

In this chapter we will be proving the hypothesis that, "*there is increase in accuracy of bulk behavior modelling of twin activity when the influence of twin neighborhood is included*".

Hexagonal close-packed (HCP) materials frequently rely upon twinning to accommodate plastic deformation in the c-axis direction. The resultant texture evolution is fundamental to subsequent deformation and hardening behavior. Hence, much work has been undertaken to elucidate specific twin mechanisms, such as nucleation and transmission, at the microstructural level. Various models of twin activity have been developed to incorporate twin nucleation and growth behavior, ranging from mean field to full-field explicit models (Ardeljan et al. 2015; Knezevic, Daymond, and Beyerlein 2016); however, while several studies highlight the importance and unique attributes of twin transmission across grain boundaries, the incorporation of this phenomenon into the constitutive modeling has been slow. This section introduces a neighborhood-based viscoplastic self-consistent (NVPSC) model to capture trans-grain boundary

(GB) transmission of twins, and analyze the effect of modeling this phenomenon in a study of AZ31 Mg alloy.

Early attempts to capture the evolution of texture, associated with twin formation, were based upon simple reorientation of entire grains (defined here as groupings in the texture that have distinct orientations) during the deformation process. These early twinning models were based on accounting for crystal reorientation effects as the predominant twin reorientation (PTR) and the volume fraction transfer (VFT) scheme. Subsequent improvements incorporated more realistic variant selection and the ability to transform sub regions of grains into twins (the so called composite grain twinning model) in both VPSC and finite element crystal plasticity models (e.g. (Lebensohn and Tomé 1993; Kalidindi 1998; Proust, Tomé, and Kaschner 2007; Knezevic et al. 2013)). Recent developments have also incorporated elastic effects into self-consistent models to enable the consideration of phenomena such as de-twinning and complex strain paths (Want, Tomé, and Huang 2010; Zecevic et al. 2015). An advantage of a CPFE approach is that it yields good texture predictions even at small scales where the constitutive law, which is built on a statistical dislocation model , reaches its limits owing to the small size of the elements (Roters and Raabe 2005). Of the various deformation models developed, the viscoplastic self-consistent (VPSC) models of crystal plasticity provide a popular compromise between accuracy and efficiency.

Most models that incorporate twin activity assume that they form and propagate according to a Schmid-type law (a review of several models is given in (Proust, Tomé, and Kaschner 2007)). Since the critical resolved shear stress (CRSS) for an extension twin formation at room temperature is lower than that of <c+a> slip, twin formation will be favored when c-axis extension is required (Barnett 2007a; Yoo 1981). Furthermore, twin evolution tends to follow a

more complex path, with twin nucleation occurring as a stochastic process, and subsequent growth complying with Schmid's law. A recent version of the VPSC model by Niezgoda et al. incorporates consideration of these factors (Niezgoda et al. 2014). The same study noted preferred formation of twins at certain GBs (see also (Beyerlein et al. 2010)), but did not include this factor into the model. Similarly, Khosravani et al. reported that twins are more likely to occur at GBs with high angles of misorientation.

In addition to spontaneous nucleation of twins at GBs, 'transmission' of twins across GBs is regularly observed, and may be an important component of the deformation process for incorporation into models. Chains of twins are often observed in micrographs of various materials that can extend across many grains. As a growing twin impinges upon a grain boundary low resistance to transmission and a high driving force arises between the twin and potential twin variants in the neighboring grain, leading to formation of a new twin and an expanding chain of connected twins. Earlier work on pure Mg studied the effect of grain boundary misorientation on the frequency of adjoined twin pairs, where two twins met at the same point in the boundary. It was found that the probability of finding an adjoining twin pair (ATP) steadily decreased with increasing misorientation angle, cutting off at an angle of 55° (Beyerlein et al. 2010). One recent study of AZ31B sheet found that extension twins were able to transmit across GBs with misorientations of less than ~35° (Khosravani et al. 2015). A similar study of HCP rhenium concluded that twin transmission occurred across GBs with misorientations of less than ~25° (Kacher and Minor 2014). Pure Zr was found to have an even higher value of 60° (Kumar et al. 2016). Similar results were found for AM30 magnesium.

The transmission coefficient (e.g. the m' factor described in) has been defined in various different ways, but would generally consider the relative alignments of two key crystallographic

features of the microstructure: 1) the twin plane in the current grain and the plane of potential variants in the neighboring grain, and 2) the Burgers vector of the current twin and the potential variants in the neighboring grain. A typical relationship is represented by:

$$m' = \cos\kappa \cos\psi = (\mathrm{n}^t \cdot \mathrm{n}^v)(\mathrm{b}^t \cdot \mathrm{b}^v) \quad (3\text{-}1)$$

where $\mathbf{n}^t$ and $\mathbf{n}^v$ are normals to the twin and variant planes respectively, and $\mathbf{b}^t$, $\mathbf{b}^v$ are unit vectors in the direction of the Burgers vector for the twin and variants. In prior studies with rhenium, m' provided a reasonable prediction of twin transmission (Kacher and Minor 2014). A more recent paper indicated a similar result for Mg (Kumar et al. 2016). However, m' and similar measures relating alignment of incoming and outgoing twin shear vectors, or Schmid factor for outgoing twin, tend to overestimate the probability of twin transmission at medium to high levels of misorientation. In the same paper, a qualitative explanation was given for the relatively poor predictive capability of these transmission factors. A large misorientation between the twinned grain and its neighbor was not the only reason for a lack of transmission, but also the fact that the neighbor grain was not oriented favorably for twinning with respect to the applied strain, compared to the parent grain. In addition, the local plastic response between the tip of the twin and the GB with the neighbor must be accounted for in order to accurately predict transmission and the more plastically anisotropic the material, the higher the driving force for twin transmission.

In VPSC models, microstructural detail (such as lattice orientation) is incorporated at the grain length scale, but is homogenized at the neighborhood level (Proust et al. 2009; Li et al. 2013; Abdolvand et al. 2015). These models fundamentally treat each grain in isolation, in the sense that they have no specific neighbors or neighborhood. It is an ideal model for capturing the stochastic nature of twin formation, and resultant texture evolution, when neighborhood-scale

correlations do not play a significant role. However, the absence of neighborhood details precludes a rigorous treatment of trans-GB phenomena, such as twin transmission. A twin in one VPSC grain forms completely independently of twins in other grains. In this work, a new type of VPSC model is studied, where grain neighbors are tracked in order to enable the concept of grain boundary to be employed, and to allow the phenomenon of twin transmission to be implemented and analyzed.

3.2 Methodology

3.2.1 VPSC Model

Commonly observed twins in the AZ31 system include extension twins: $\{10\bar{1}2\}\langle 1\bar{2}10\rangle$ and compression twins: $\{10\bar{1}1\}\langle 1\bar{2}10\rangle$ (Koike 2005). In the current study, the sheet specimen was compressed along the rolling direction, extending the c-axis to favor the creation of extension twins; subsequently, these were the only type that we observed in the data. Therefore, while the VPSC model was designed to cope with both twin types, we restrict the current discussion to extension twins.

This builds upon two previously developed VPSC models by merging them and adding the capability to predict transmission of twins between neighboring grains. The first model is built on a dislocation density based hardening law within crystal plasticity and is described in detail in (Knezevic et al. 2015). The second introduces a stochastic model for twin nucleation, along with other refinements, and is discussed in detail in (Niezgoda et al. 2014). We provide a brief review of these models below, followed by a presentation of the adaptations made for the current model.

A typical VPSC approach represents a polycrystal by a set of grains, each having an orientation, shape and size. The grain is treated as a visco-plastic inclusion embedded in a

homogeneous effective medium. The inclusion model is solved using a Green's function approach (Lebensohn and Tomé 1993). Enforcing the macro-homogeneity condition of self-consistency between the macroscopic stress and grain average stresses allows for calculation of the viscoplastic response of the effective medium. This response can be compared with that of a test polycrystalline specimen.

Plastic deformation in each grain is accommodated via the activation of slip, with an additional potential of twinning. The corresponding slip or twin shearing rate, $\dot{\gamma}^s$ on a given system, s, is modeled using the power-law relation:

$$\dot{\gamma}^s = \dot{\gamma}_0 \left|\frac{\tau^s}{\tau_c^s}\right|^{\frac{1}{m}} sign(\tau^s) \qquad (3\text{-}2)$$

where $\dot{\gamma}_0$ is the reference slip rate set to be the macroscopic strain rate, m is the rate sensitivity parameter set to be 0.05, τ^s is the resolved shear stress, and τ_c^s is the threshold stress on the slip system. The twin propagation is treated as a pseudo-slip mechanism, as originally proposed in (Van Houtte 1978; Chin, Hosford, and Mendorf 1969).

According to Eq. (2), the crystal plasticity constitutive law requires a threshold resistance to activate each slip mode and each twinning mode. In this modeling framework, these activation stresses can evolve with strain, separately, for each system, within each grain in the polycrystal via a dislocation density hardening law. For dislocation slip, resistance changes as more dislocations are stored in the crystal. The VPSC model adopts a thermally activated dislocation density based hardening law that was originally described in , and advanced in the context of the VPSC model and HCP metals in (Beyerlein, McCabe, and Tome 2011; Beyerlein, McCabe, and Tomé 2011; Knezevic et al. 2015) .

The hardening model parameters for AZ31 used in the present study are taken from (Ardeljan et al. 2016). Based on these parameters, the ratios of the initial resistances at room

temperature for basal <a> to prismatic <a> is 1:4, basal <a> to pyramidal <c+a> is 1:14, and basal <a> to extension twinning is 1:1.2. These ratios can evolve with the rate of strain hardening due to the evolution of dislocation density and various slip-slip and slip-twin interactions. The objective here is to combine this hardening model with the stochastic twinning model within the VPSC homogenization approach and to further advance it by enabling twin transmission from a grain containing a twin to its neighbor grains.

The approach of treating twin activation as a stochastic event that is influenced by stress level and grain size was described in (Niezgoda et al. 2014). For a given grain with known grain size, the number of neighbors is estimated, resulting in an approximated facet size for the grain neighbors. This facet size is divided into nucleation zones, the size of which are particular to the given material, and within each of which twin nucleation is possible. The VPSC model calculates the stress within the grain, then applies a perturbation to the stress to account for material heterogeneity. If the resultant stress exceeds the CRSS for twin nucleation (another material parameter), then there is a certain probability that each nucleation zone will spawn a twin. If at least one twin is predicted as likely to nucleate within the grain, then the grain is counted as a twinned grain, and is tracked for twin growth. As mentioned above, twin growth occurs as a pseudo-slip phenomenon if the resolved shear stress reaches the critical resolved shear stress for a twin type.

The dislocation density hardening law is combined here with the stochastic twin nucleation model. We then add the ability to transmit twins across grain boundaries by tracking neighbors of each grain. The selection of neighbors is based on an initial EBSD scan. While this only includes the neighbors that are visible in a 2D slice, it is assumed that the character of these

neighbors is representative of all neighbors. Furthermore, this allows a more accurate implementation of the observed correlations between twin nucleation and GB type.

The overall process of stochastic twin nucleation by Niezgoda et al. was maintained in the present work, with a few additions to more accurately reflect experimental data, and to incorporate GB misorientation into the process. First, a list of neighbors for each grain, as well as the corresponding misorientation between the grain and its neighbors, was obtained from EBSD scans containing approximately 4500 grains with each grain having an average of 6 neighbors. In the absence of experimental data, neighbor selection might be performed such that a desired grain boundary character distribution can be achieved. In order to determine whether twin nucleation would occur, a random grain from the list of neighbors was chosen to assign a misorientation angle and to calculate the facet area. Next, based on the experimental work done in published literature (Khosravani et al. 2015; Beyerlein et al. 2010), it is clear that there is a relationship between the misorientation angle and twin activity, with twin nucleation being more prevalent in the misorientation angle range of 30-45°. For this model, it was assumed that a simple Gaussian distribution could approximate the relationship between the frequency of twinning and misorientation:

$$x = \frac{k}{\sqrt{2\pi\sigma^2}} e^{-\frac{(m-\mu)^2}{2\sigma^2}} \qquad (3\text{-}3)$$

where x is the probability value of twin nucleation based on the misorientation angle between neighboring grains, μ is the mean misorientation angle where twin nucleation is assumed to be most favorable, m is the misorientation angle between the two grains, σ is the standard deviation of misorientation, and k is a correction factor to scale the probability value according to the other stochastic weights used. This misorientation probability weight was included as another factor, in addition to the facet area and stress fluctuation, to determine

whether twin nucleation should occur. Both the nucleation and transmission probabilities correlate with GB misorientation, with transmission preferring low angle GBs. The minimum geometrical compatibility factor for transmission was adjusted to provide a reasonable reflection of twin-twin intersections at GBs in the experimental data; then the distribution for weighting nucleation activity was tuned to fit the overall distribution of twin-GB intersections. The resultant assumed distribution has a mean of 30°, which was observed to be several degrees less than expected from Khosravani's results (which has a mean closer to 40°), but is generally in line with the results of Beyerlein and other studies. k and σ have been set to 50 and 20, respectively.

3.2.2 Incorporating misorientation and twin transmission into VPSC misorientation

To include the capability of twin transmission within the VPSC framework, a new subroutine was appended onto the stochastic nucleation model. Several assumptions were made to simplify the model. First, when a twin was predicted in a grain no other twin was considered to nucleate in the same grain. Therefore, once a twin is nucleated or transmitted into a grain, that grain was flagged for twinning and the twin could then propagate as normal, but further nucleation events, either stochastically or through transmission, were no longer considered in the grain. Second, no transmission events could occur on the first strain step. Third, for a twin to transmit into a specific neighboring grain, it would need to impinge on that grain's boundary. Consequently, there is a probabilistic nature to transmission based on whether the twin impinges on the correct boundary. Fourth, the activated twin system would be the twinning variant most closely aligned with the twin found within the neighboring grain. Finally, the minimum twin volume fraction that a twin must have to transmit through a grain boundary is assumed, arbitrarily, to be 1% of the area of the grain in which the twin is located.

Based upon the preceding assumptions, the following conditions were used to determine whether a twin would transmit into the grain being observed:

I. The volume (or area for 2D) of the twin must exceed 1% of the grain volume in which the twin is found.

II. The maximum geometric compatibility factor (over all possible twin variants), m' (Eq. 1), must exceed a given threshold value. (In this experiment, the threshold value for m' was calibrated from the data to be 0.32).

III. The neighboring twin must be impinging on the correct grain boundary. Each grain had an average of ~6 neighbors (an assumption in the calculations based on AZ31B's HCP structure). A twin, which is direction dependent, can stretch between two grain boundaries. So out of the 6 GB's available, the twin can originate from 3 GB's and is therefore assumed to nucleate or transmit through any one of these 3 GB's giving it a 33% (1/3) chance to do so on a correct GB.

If all three of these criteria were satisfied, then the grain being observed was assigned a twin and was counted as a transmission twin. Using the criteria given, the transmission process can be summarized in the following paragraph.

For every strain increment following the first (in which only stochastic nucleation was considered), each grain was checked for a twin. If the grain contained a twin, then its propagation and subsequent effect on hardening would be calculated. If the grain did not have a twin, then each of its neighbors would be checked for a twin that satisfies each of the three transmission criteria. If such a neighboring twin was found, then the grain would be assigned a transmission twin, otherwise it would be checked for stochastic nucleation of a twin. This process was repeated for each grain in each strain step up to a targeted amount of strain. The

overall process of including the potential for twin transmission in the NVPSC model is described using a flowchart shown in figure 3-1. The effectiveness of the model was tested against a specimen of AZ31B that was deformed and characterized as described in the next section.

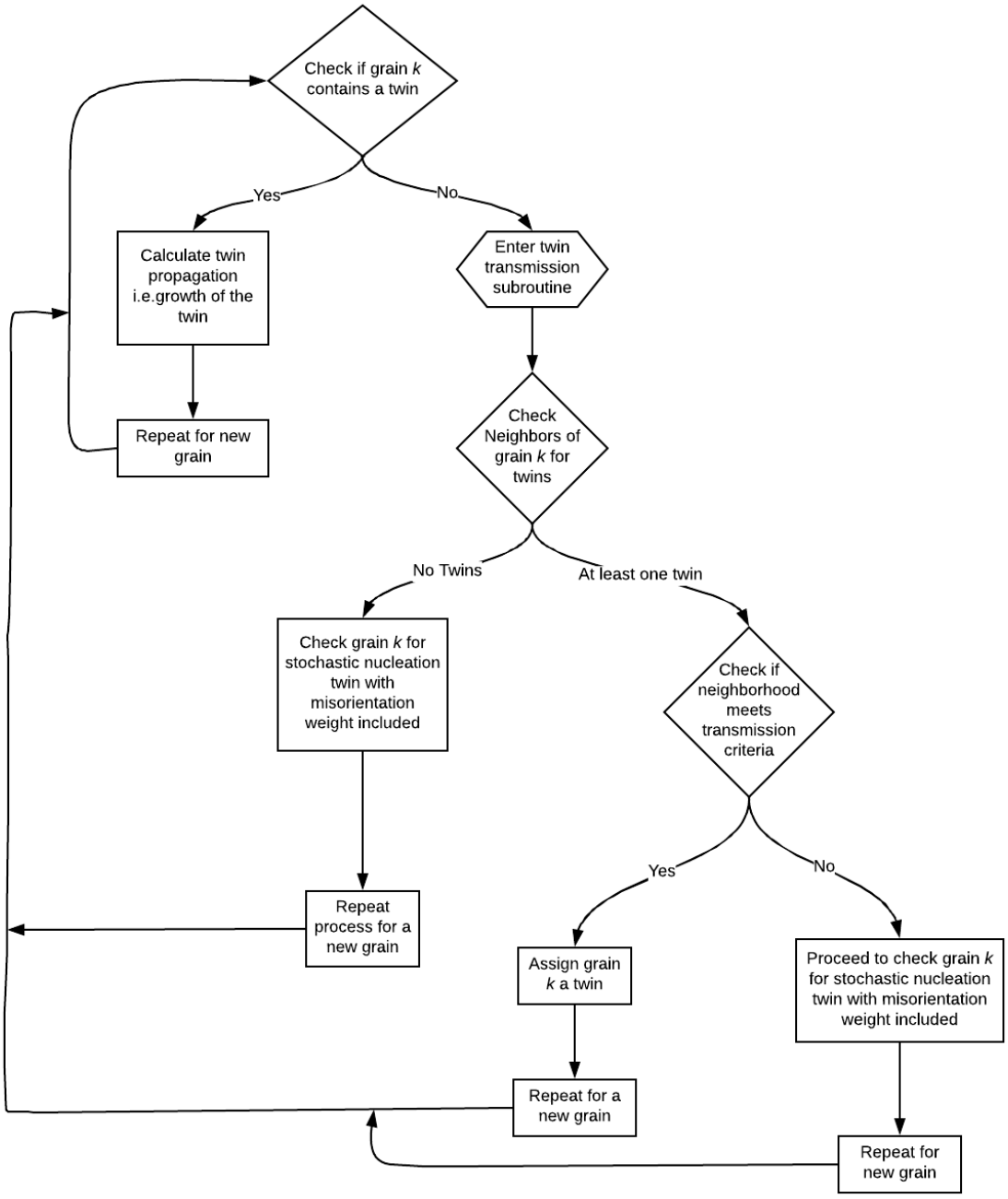

Figure 3-1: Flowchart of twin transmission simulation algorithm.

3.2.3 Experiment

A rectangular prism of size 4 mm x 3 mm of annealed (350°C for 15 minutes) and twin-free AZ31B sheet was polished for EBSD analysis on the ND surface using the following procedure. The specimen was first levelled by grinding the ND surface with 800 grit SiC and 1200 grit SiC sheets on a LECO® automatic polishing machine. This was followed by polishing the specimen surface using polycrystalline diamond compounds of size 6 μm, 3 μm and 1 μm, in that order, on an Imperial polishing cloth from Allied High Tech®. Chemical polish was done by immersing the specimen for 10 secs in a solution of 100 ml of methanol, 12 ml of HCl and 8 ml of HNO3. The specimen surface was further fine polished with 0.25 μm polycrystalline diamond paste to remove any discoloration that occurred during the chemical polish. It was then etched using a solution containing 60% ethanol, 20% water, 15% acetic acid and 5% nitric acid for 1 second and washed immediately in a bath of ethanol in preparation for EBSD study. The specimen was compressed in-situ along the RD direction, and constrained in the TD direction to ensure Poisson expansion in the ND direction. This would promote tensile twin formation due to the lack of basal or pyramidal slip systems (high CRSS at room temperature) available to accommodate expansion in this direction. The deformation mode is programmed into the NVPSC to reflect this constraint. Macroscopic compression true strain levels of 2.5%, 5.3% and 7.5% were applied, and scans of size 90 x 137.7 μm on the ND surface were taken in different regions in each specimen, with a step size of 0.3 μm and a total of 138,460 scan points within the area.

Standard commercial EBSD software (TSL OIM Analysis®) was used to determine the orientation at each scan point, and to identify twins resulting from the compression of the specimens. To account for all the twins, including the twins not identified by the software, the IQ

map was used to manually count the relevant twins. To eliminate partial grains from the analysis, the twins on the edge of the scan area and those with poor confidence index (CI<0.1) were ignored. In so doing, approximately 135 twins for 2.5% strain, 136 twins for 5.3% strain, and 192 twins for 7.5% strain were added to those automatically detected by the software. Twin numbers used in the analysis that follows are counts of twins in the areas scanned at each intermittent strain step, where each scan area contained an average about 1500 grains. The counts provided by OIM software were augmented by manual, visual identification of twins not identified by the software. Identity of the parent grain for each twin was entered into the VPSC model, to provide the model with information about those grains before the formation of twins. This introduces a small error into the process since the parent grain would reorient slightly during deformation. After calibrating the model to achieve the overall number of twins at the 2.5% strain level (by adjusting the stochastic nucleation parameters), the model prediction of twin activity was then compared with the actual twin activity seen in the compressed specimens at all strain levels. Specifically, the Weibull parameter affecting nucleation probability was set to 140, while the shape parameter was set to 2.0 (see (Niezgoda et al. 2014) for more details on these parameters). The minimum geometrical compatibility factor for transmission was set to 0.32 to give the approximate number of transmission events.

3.3 Results

Twin formation and growth in the AZ31B specimen subjected to uniaxial compression is shown using the twin-parent maps generated by using the OIM Analysis tool in . The twins are identified to be predominately of the orientation $\{10\bar{1}2\}\langle 11\bar{2}0\rangle$ as shown in Figure 3-2. In fact, approximately 90% - 98% of the total twins formed are noticed to be of this type in the deformed sample for the strain levels observed. When the NVPSC is to be modelled for different textures

and different loading conditions, the type of twins allowed to be simulated in the model should be changed to more correctly reflect what happens in the microstructure.

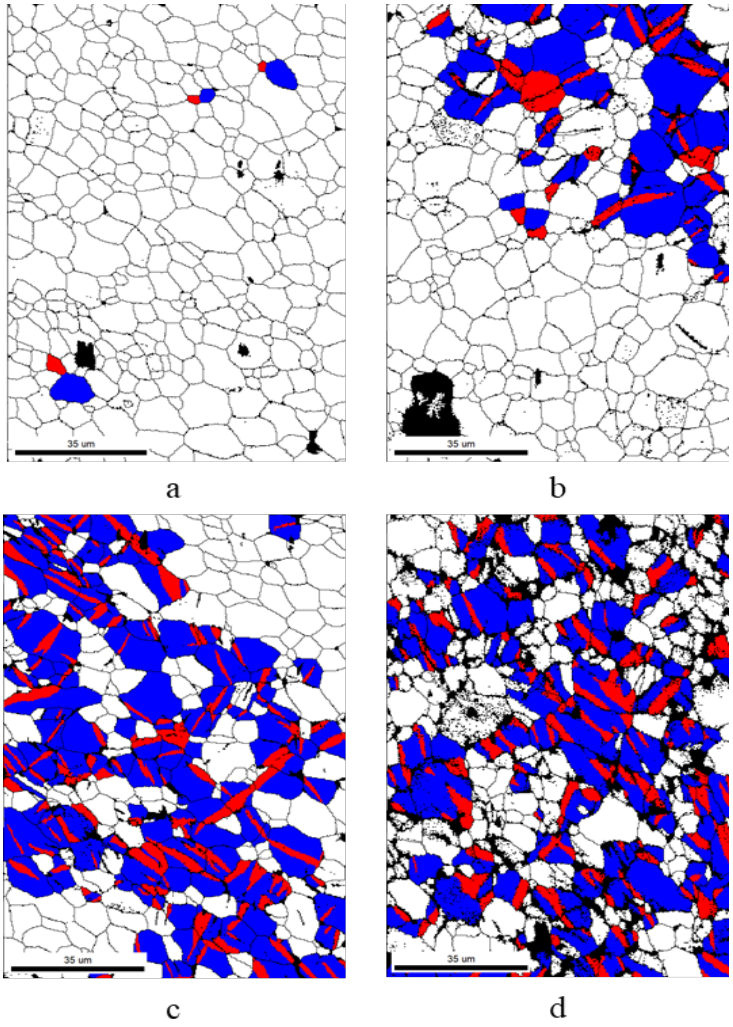

Figure 3-2: Twin - Parent maps for sample with a. 0% strain, b. 2.5% strain, c. 5.3% strain and d. 7.5% strain. Blue color denotes the parent grain and red color denotes the twins identified by OIM Analysis. The black areas are filtered out because of their low confidence index.

As the CRSS value of the grain determines the probability of twin nucleation according to the stochastic model, it was adjusted to accurately reflect the twinning phenomenon for this model. The CRSS values used in the 3 models are listed in Table 3-1. The constants A, B, C and

D used to calculate the resolved shear stress (τ_c^s) as described in equation 3 in the paper (Knezevic et al. 2015) are also listed in Table 3-1. The texture evolution for VPSC simulations and for the compressed sample are compared in figure 3-3 using pole figures at each of the intermittent strain levels.

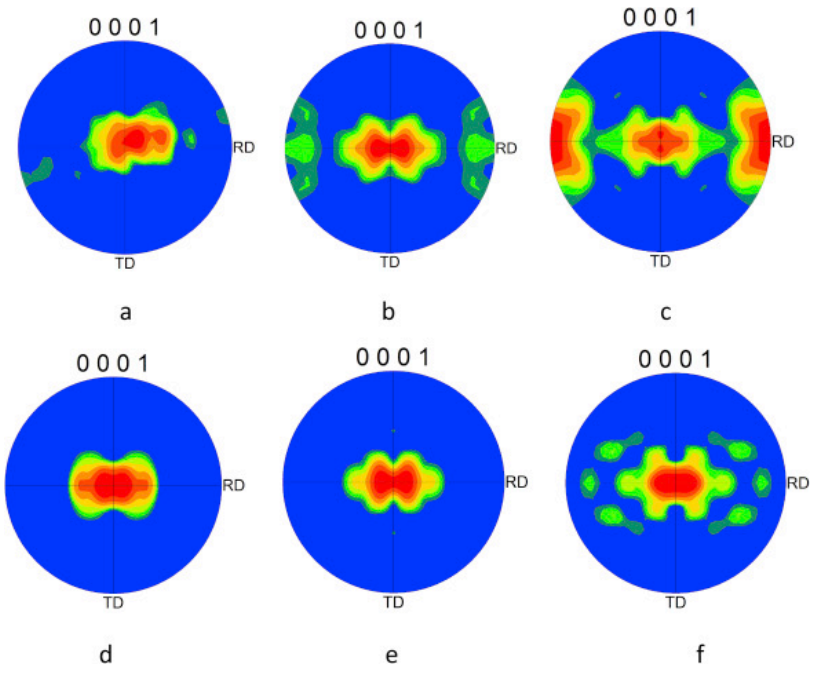

Figure 3-3: Representative pole figures for each strain step a. 2.5% strain, b. 5.3% strain and c. 7.5% strain. Simulated Pole figures by VPSC from NVPSC for samples strained to different strain steps d. 2.5% strain, e. 5.3% strain and f. 7.5% strain. 0% strain utilizes the same texture file.

The development of simulated texture compares favorably with the observed sample texture. There is a gradual deviation from the initial basal texture as the strain applied on the specimen increases. This can also be observed from the deviation of the c-axis orientation from the normal direction as shown in figure 3-4. The figure gives the count or frequency of grains with twins for a range of misorientations (0° - 90°). The grains oriented initially parallel to the normal direction appear to have the most twins for the initial strain levels. The percentage of

grains that have an orientation deviation of the c-axis away from normal increases for the sample when the strain level increases. The NVPSC simulation follows the experimental observation closely. Similar results have been published recently (Kabirian, Khan, and Gnaupel-Herlod 2015).

Table 3-1: Comparison of material parameters used in the VPSC and NVPSC models.

MATERIAL PARAMETERS FOR NVPSC		A	B	C	D	CRSS, MPA
Prismatic		108	0	1	359	108
Pyramidal <c+a>		290	0	1	489	290
Basal		17	0	1	786	17
Twin Nucleation	Tensile Twinning	13	0	100	NA	165
	Compressive Twinning	5	0	77	NA	340
Twin Propagation	Tensile Twinning	135	0	120	NA	20
	Compressive Twinning	130	0	90	NA	340

Figure 3-5 shows that the total number of predicted twins agrees favorably with the observed twins counted in the EBSD scans for the compressed sample at the different strain levels. The number of transmission twins predicted by the NVPSC model, based upon both the transmissivity factor and local strain content (incorporated into the twin size), also generally line-up with the experimental data, except for a slight increase in predicted number at the highest strain level. Since the previous VPSC model does not track neighborhoods (neighbors may be randomly assigned at each strain step, but do not result in the same neighborhood each time), predictions are not available for that model. However, an estimate can be made by considering the probability of neighboring grains both containing twins for the case that no transmission

occurs (i.e., twins in one grain do not affect twins in neighboring grains). In this case, it may be assumed that the probability of twins occurring in adjoining grains is random; these values are given in Table 3-2. The number of adjoining grains, with twins in both grains, is significantly higher than random for the NVPSC model.

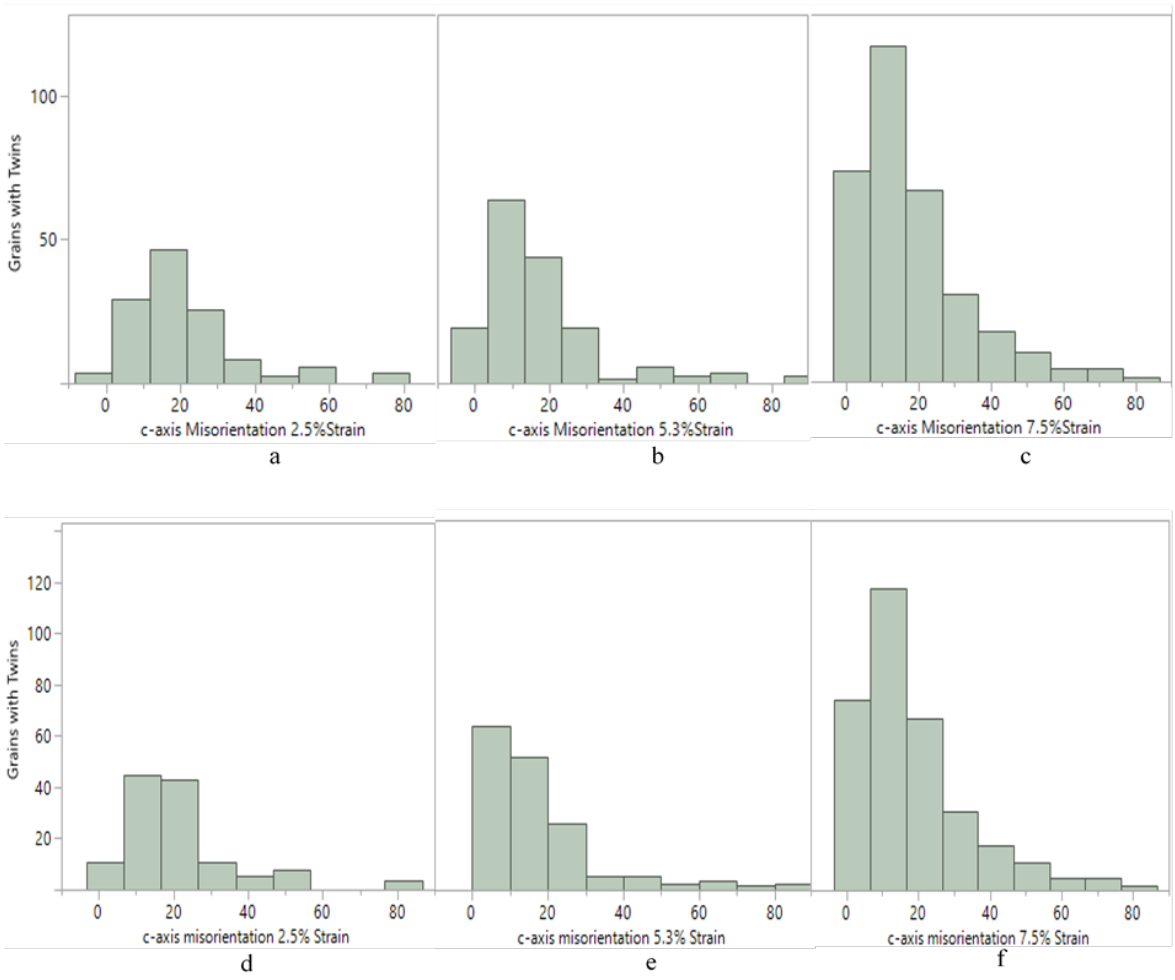

Figure 3-4: c-axis misorientation of twinned grains for (a – c) compressed sample and (d – f) NVPSC simulation.

The effect of transmission twins on the relationship between twins present in neighboring grains is also illustrated in figure 3-6. The appearance of twinned grains for the different numbers of neighbors from the experimental data, and from the NVPSC model is visualized. The

NVPSC model with transmission prediction reflects the actual data much more closely. Without identifying twin neighborhoods, transmission activities within the microstructure, twin transmission cannot be simulated correctly by the VPSC model.

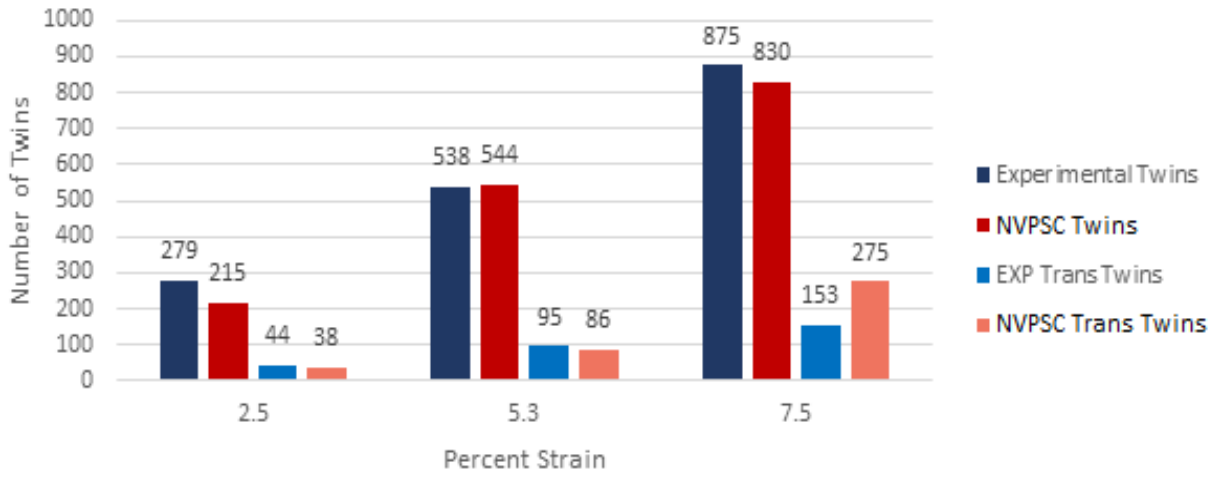

Figure 3-5: Comparison of number twins observed experimentally and twins predicted using NVPSC model.

Table 3-2: Prediction of twinned grains with a twinned neighbor- VPSC vs. NVPSC.

Strain Level	*Random probability that a twinned grain has a neighbor with a twin according to previous VPSC*	*Probability that a twinned grain has a neighbor with a twin according to NVPSC*
2.5%	20.3%	28.1%
5.3%	22.9%	37.3%
7.5%	32.7%	55.3%

It has been noted that twin activity at GBs due to spontaneous nucleation favors higher angle grain boundaries, while transmission events on twin activity for various materials favors low angle grain boundaries (LAGB) (Khosravani et al. 2015). By modifying the transmissivity coefficient, the NVPSC model proposed in this demonstrates that when LAGB's are favored for

twin transmission has more accurately predicted the frequencies seen in the experiment. The relation between the experimental, VPSC and NVPC models with respect to twin activity and preferred GB misorientation is demonstrated in figure 3-7. It should be noted that the NVPSC model does not add significant computational overhead to an existing VPSC model.

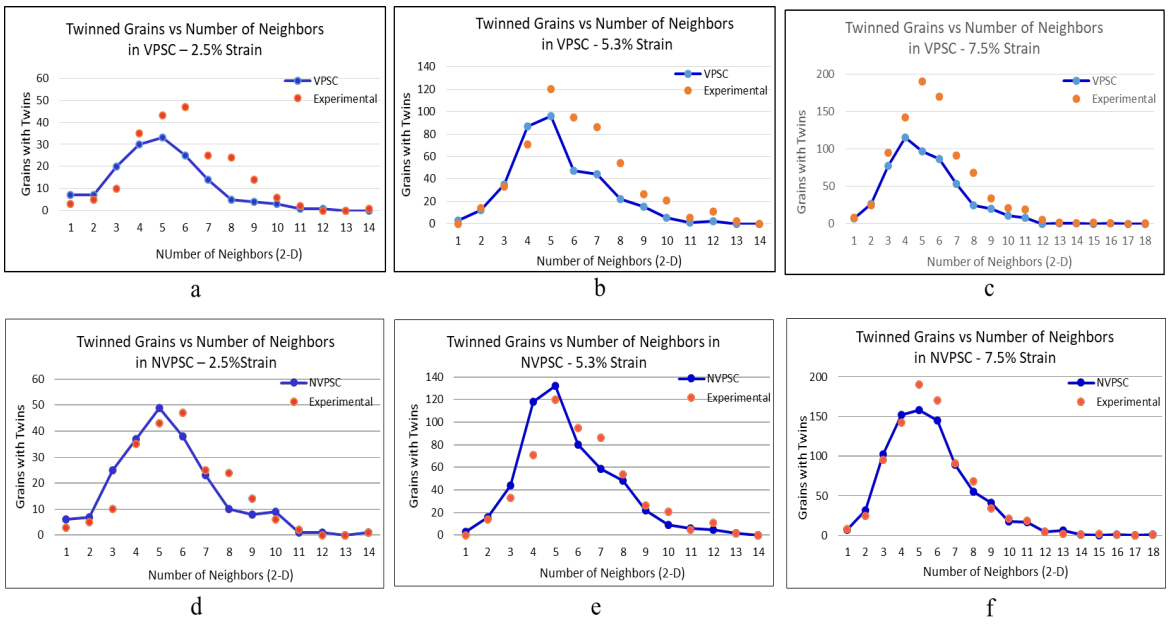

Figure 3-6: Comparison of frequency of twinned grains and the number of neighbors for the grain in the VPSC and the NVPSC models. a, b & c are the comparison charts for the VPSC model for increasing strain levels of 2.5%, 5.3% and 7.5% and d, e &f are similar comparison charts for NVPSC with transmission.

3.4 Conclusion

The presence of transmission events during twin activity for various materials is commonly observed in experimental investigations. The neighborhood VPSC model (NVPSC) proposed in this section demonstrates that statistically accounting for transmission events can be handled in a practical manner that does not add significant computational overhead to an existing VPSC model. A dislocation density-based hardening law and a stochastic model for twin nucleation from previous work are combined, and a neighborhood tracking capability is added.

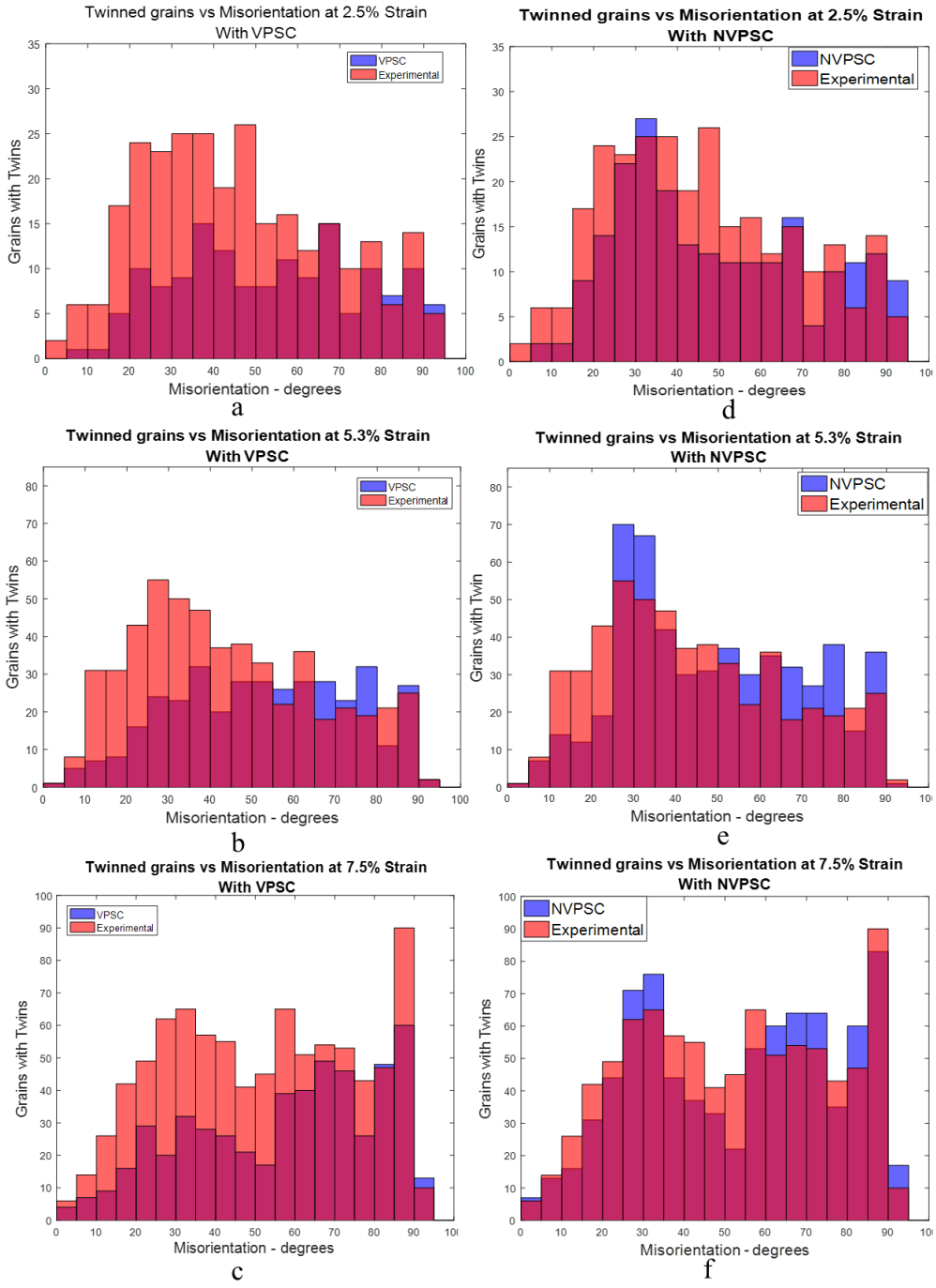

Figure 3-7: Comparison of accuracy in predicting twin-twin interaction with GBs of particular misorientation for VPSC and NVPSC 2.5%, 5.3% and 7.5% strain

The resultant ability of twins in neighboring grains to influence twin formation in a given grain is incorporated into the model, and the resultant twin distributions compared with

experimentally observed results. In building of the model several assumptions were made: for example, only one twin per grain is allowed, a transmissivity coefficient is defined, and twin transmission can only occur if a twin occupies 1% of the area of the parent grain.

The change in texture and twin activity is followed for several strain increments of AZ31B for both experimental and simulated deformation. After fitting the model to the number of twins observed in the first strain step, the number of predicted twins agrees favorably with the observed twins counted in the EBSD scans for the compressed specimens at each level of strain. The number of transmission twins predicted by the NVPSC model also agrees with the experimental data.

The NVPSC model better captures the relationship between twin activity and GB misorientation, with the new model predicting higher numbers of interactions with low angle grain boundaries, due to the greater ease of transmission. The propensity of GB types to transmit twins agreed with published research (Khosravani et al. 2015; Kacher and Minor 2014; Kumar et al. 2016; El Kadiri, Baird, et al. 2013; El Kadiri, Kapil, et al. 2013). Such behavior may significantly affect resultant deformation models and related hardening behavior. Furthermore, the distribution of twins in a given neighborhood is much better reflected by the new model (with higher likelihood that neighboring grains will both have twins).

While this particular case study is somewhat limited in its consideration of a single texture and a single strain path, it does cover a range of strain steps, and there is no particular reason to believe that the underlying factors governing tension twin activity would fundamentally change (in terms of nucleation and transmission) for other textures and strain paths. This is also somewhat validated in the sense that the results correlate with various other published experimental studies (for example, in terms of the correlation between GB type and

twin interactions). The current study is valid for tensions twins and a different study would be required for compression-type twins.

4 <C+A> SLIP VS TWIN ACTIVITY AT SLIGHTLY ELEVATED TEMPERATURE IN AZ31B

Publication citation: Chelladurai, Isaac, Michael P. Miles, David T. Fullwood, John E. Carsley, Raj K. Mishra, Irene J. Beyerlein, and Marko Knezevic. "Microstructure correlation with formability for biaxial stretching of magnesium alloy AZ31B at mildly elevated temperatures." JOM 69, no. 5 (2017): 907-914.

4.1 Chapter Introduction

In this chapter of the thesis, the hypothesis, "*c+a slip provided an important deformation mode in hexagonal materials even at mildly elevated temperatures*".

Magnesium and its alloys undergo only moderate amounts of plasticity at room temperature before fracture. The HCP crystal structure of magnesium has only one close packed plane (basal plane) and when deformed, slip on these close packed planes does not provide the required number of independent deformation modes needed for an arbitrary shape change (Staroselsky and Anand 2003) causing a lack in ductility at room temperature. Furthermore, at room temperature, strong basal texture of the rolled Mg sheet with the c-axis direction largely perpendicular to the plane of the sheet leads to insufficient strain accommodation through the thickness. For this alloy, it has been suggested that twinning, and more particularly compression twinning, is the primary mechanism for through-thickness contraction deformation (Martin et al. 2010; Agnew, Yoo, and Tome 2001). The evolution of microstructure for a range of

temperatures has been previously explored for the AZ31B alloy (Chapuis and Driver 2010), and improved ductility has been observed in various Mg alloys at elevated temperatures(Chen and Huang 2003; Zhang, Yin, and Wu 2006; Tabacaru and Oancea 2001). Barnett explained this as a result of enhanced activity of non-basal slip (Barnett 2007a). Other studies also demonstrate how twinning could favorably assist in improving the ductility of HCP materials (Yoshinaga, Obara, and Morozumi 1973; Yoo 1981). This study seeks to quantify slip and twin activity for the AZ31B alloy across this moderately elevated temperature range under a biaxial load in order to provide insight into the observed improvement in ductility with increase in temperature.

Many studies have used a variety of methods to understand correlations and behavior at the microstructural level for magnesium. For example, formability and failure mechanisms for Mg alloys deformed in uniaxial tension, uniaxial compression and biaxial tension have been studied for the purpose of establishing crack initiation sites and investigating the relationship between strain path and the failure initiation mechanism (Scott et al. 2012; Al-Samman and Gottstein 2008). Other articles have investigated these correlations to better predict twinning events (Beyerlein et al. 2010; Wang, Beyerlein, and Tomé 2010; Capolungo and Beyerlein 2008; Wang et al. 2009; Rampton 2015; Beyerlein, McCabe, and Tomé 2011). But a more detailed investigation on the microstructural features relating to the transition from twin activity to the various slip modes (including non-basal slip) is needed. One approach to establishing these correlations utilized recent advances in cross-correlation electron backscatter diffraction (EBSD) to observe microstructure changes after AZ31B specimens were deformed at various temperatures, in order to assess the potential to resolve slip activity onto the various possible planes (Gardner et al. 2010).

In the present work, AZ31B sheets were stretched in biaxial tension using a limiting dome height die set at room temperature and subsequent increments of 25ºC up to 150ºC. Changes in microstructure were then related to deformation mechanisms that were deduced from twin density, calculated as the ratio of the number of twins per unit area in each of the observed EBSD scans, and geometrically necessary dislocation (GND) content for each temperature. Though there have been studies on the influence of temperature on extension twins, as far as the authors are aware similar studies for compression twins are less common. Evidence of secondary twinning at lower temperatures is presented along with analysis of slip activity based on GND for different temperatures.

4.2 Methodology

AZ31B sheets of 2 mm thickness were stretched over a 101.6 mm diameter hemispherical punch at temperatures ranging from 25°C - 150°C (in increments of 25°C). All sheet blanks had dimensions of approximately 200 mm x 200 mm to ensure that they were fully clamped. In addition, boron nitride lubricant was applied to the center of each specimen prior to forming, to reduce friction and promote biaxial stretching. The press was a double-action, servo-hydraulic press with a fully closed-loop control system consisting of a clamp rated at 68,000 kgf (75 tons) and a punch rated at 45,000 kgf (50 tons). The upper die and lower blank holder were heated to the target forming temperature with band heaters (Hsu, Carsley, and Verma 2008). The upper and lower sections were enveloped in Cer-Wool® ceramic fiber to reduce heat loss during forming. A K-type thermocouple was used to measure the temperature of the blank prior to forming, where forming was initiated as soon as the target temperature was reached. Black and white ink was applied to each blank in a speckled pattern on one side of the sheet prior to forming and the resulting pattern allowed for the measurement of surface strains by a digital

image correlation (DIC) method. Biaxial strain measurements were taken from the pole area as the sheets were stretched to punch heights of 4 mm and 6 mm for each temperature. After forming, specimens were cut from the pole area and prepared for EBSD by grinding with 1200 grit silicon carbide sheets, followed by electro polishing in an electrolyte consisting of 150 ml 2-butoxyethanol, 30 ml ethanol and 15 ml perchloric acid (60%) at a voltage of 17 kV. These samples were then etched with a solution of 60% ethanol, 20% water, 15% acetic acid and 5% nitric acid prior to performing EBSD scans using a SEM microscope. Data from the EBSD scans were collected using OIM DC® software and analyzed using the TSL OIM Analysis® tool. For convenience, RD, TD and ND refer to the rolling direction, transverse direction and normal direction respectively. For example, a plane identified as an ND plane is one for which the normal is along the sheet normal direction.

To generate dislocation maps, the EBSPs (electron backscattered patterns) were post-processed. Using cross correlation techniques, the lattice perturbation between the neighboring scan points can be measured from their corresponding EBSPs from which relative elastic distortion, β, can be measured, and hence the GND density can be deduced (Gardner et al. 2010; Wilkinson, Meaden, and Dingley 2006; Ruggles and Fullwood 2013). The Nye tensor (Nye 1953) aggregates dislocation activity from individual slip systems as follows:

$$\alpha_{ij} = \Sigma_m \rho^m b_i^m v_j^m \qquad (4\text{-}1)$$

where ρ is the dislocation density for GNDs of the m^{th} dislocation system (defined here as a unique combination of Burgers vector and line vector for a pure edge or screw dislocation); b is the Burgers vector and ν is the associated line vector. The measured distortion is related to the Nye tensor via (Kroner 1958):

$$\alpha = \nabla \times \beta \qquad (4\text{-}2)$$

Because this study uses 2D EBSD, derivatives normal to the sample surface are unavailable, meaning only the right-most column of α is fully known. If strain is assumed to be negligible compared to lattice rotations, then an additional three degrees of freedom are available (Pantleon 2008). Because Mg has 36 possible slip systems and 27 unique dislocation systems, the problem of determining GND density is under-constrained. To find the most physical solution, typically the total line length of dislocations is minimized (Sun, Adams, and King 2000; Field 2005). In this case, the dislocation densities were weighted by their critical resolved shear stress (CRSS) factor:

$$\text{Minimize } f = \sum_{t=1}^{N} \left| w^t \rho^t \right| \text{, s.t. } \alpha_{ij} = \sum_{t=1}^{N} \rho^m b_i^m v_j^m \qquad (4\text{-}3)$$

where w is the weight for the CRSS factor and f is the function to be minimized.

The <c+a> to total slip ratio and the total dislocation density were then calculated from the individual dislocation system densities (El-Dasher, Adams, and Rollett 2003; Littlewood, Britton, and Wilkinson 2011). The specimens for this study were cut such that the microscopy sample surface was perpendicular to the normal direction of the sheet in each case. This was done because the plastic effects of sheet thinning were being observed, and EBSD dislocation microscopy techniques work best on this plane of deformation (Kysar et al. 2010; Kysar et al. 2007).

4.3 Results

DIC measurements of surface strains showed that stretching of the AZ31B sheets was almost perfectly biaxial for each temperature, as seen in figure 4-1. Strain in the x and y directions (in the plane of the sheet) were proportional for all punch displacements and across all forming temperatures indicating that the boron nitride lubricant was effective in minimizing

friction between the punch and the sheets for all temperatures. Biaxial stretching was desired here because the AZ31B sheets had an initial strong basal texture and any stretching that occurred required immediate thinning of the sheet with a corresponding contraction of the c-axis at the level of the average grain. As discussed in the introduction of this section, the c-axis contraction in AZ31B at room temperature induces twinning to accommodate thinning strain, but there is no clear understanding of the relationship between twinning and slip as temperature rises. An interesting result from our biaxial stretching experiments is shown in figure 4-2.

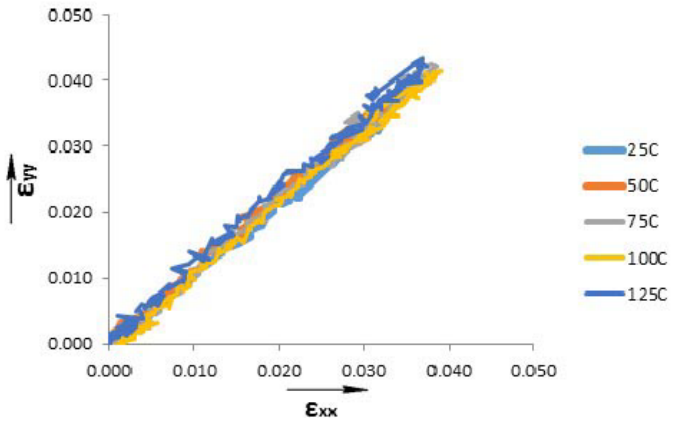

Figure 4-1: Strain paths for biaxial stretching experiments from 25°C to 125°C

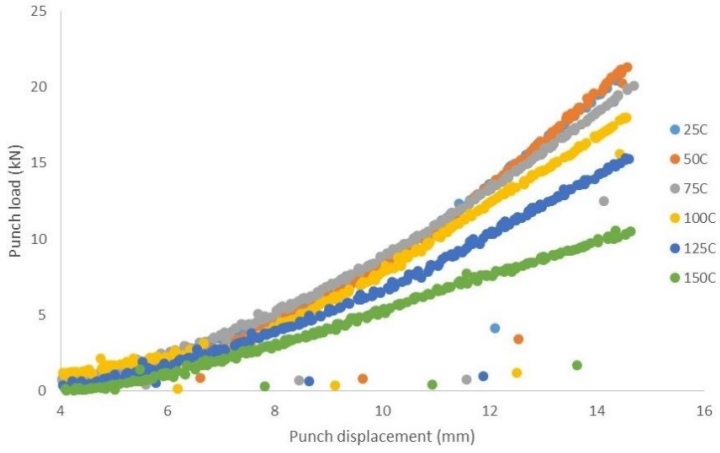

Figure 4-2: Load vs punch displacement for biaxial stretching experiments (25ºC to 150ºC)

The punch load versus punch displacement curves are almost identical for 25°C and for 50°C. At 75°C and with increasing temperature, the load increases with displacement at progressively decreasing rates. The decreasing loading curves observed between 50°C and 75°C might be explained by a reduction in the critical resolved shear stress for either contraction twinning, slip in the <a> direction, or possibly by slip in the <c+a> direction. Similar results were found in prior work when forming limits of annealed AZ31B sheets were measured at 25ºC, 75ºC, and 125ºC (Khosravani et al. 2013).

In order to quantify the change between these two activities, micrographs of the bi-axially strained specimens were examined, along with EBSD scans, to post process the scans and to measure twin density and GND content at the different forming temperatures. The microstructure reveals that contraction and double twins are predominant, but some tension twins are also present. The double twins are found to have an axis-angle combination of $\langle 11\bar{2}0 \rangle$ and 38˚. The primary twin variant was found to be a compression twin of type $\{10\bar{1}1\}$. The predominance of these twins has been observed in AZ31B in several studies (Cizek and Barnett 2008; Barnett et al. 2008; Martin et al. 2010; Lentz, Behringer, et al. 2014; Lentz, Coelho, et al. 2014).

As can be seen in figure 4-3, the overall twin density remains almost level with perhaps only a slight increase. For the purposes of this paper, the automated count of the various types of twins by the analysis tool is augmented with a manual count of twins not identified by the software, and this approach resulted in the overall twin density that was established for each scan. The apparent noise in twin measurement does not allow for identifying a trend with temperature. It appears there could be a slight upward trend for both punch heights, but there is not enough data to draw a conclusion. Therefore, we make the assumption that twin density is essentially constant with temperature in these experiments. We would also expect a larger twin

density with greater punch height, but it appears that the 4 mm sample data exhibit greater twin density than 6 mm sample data. This is likely also a result of twin density measurement error, which can be attributed to the TSL OIM Analysis® software being unable to identify all of the twins seen in the IPF maps.

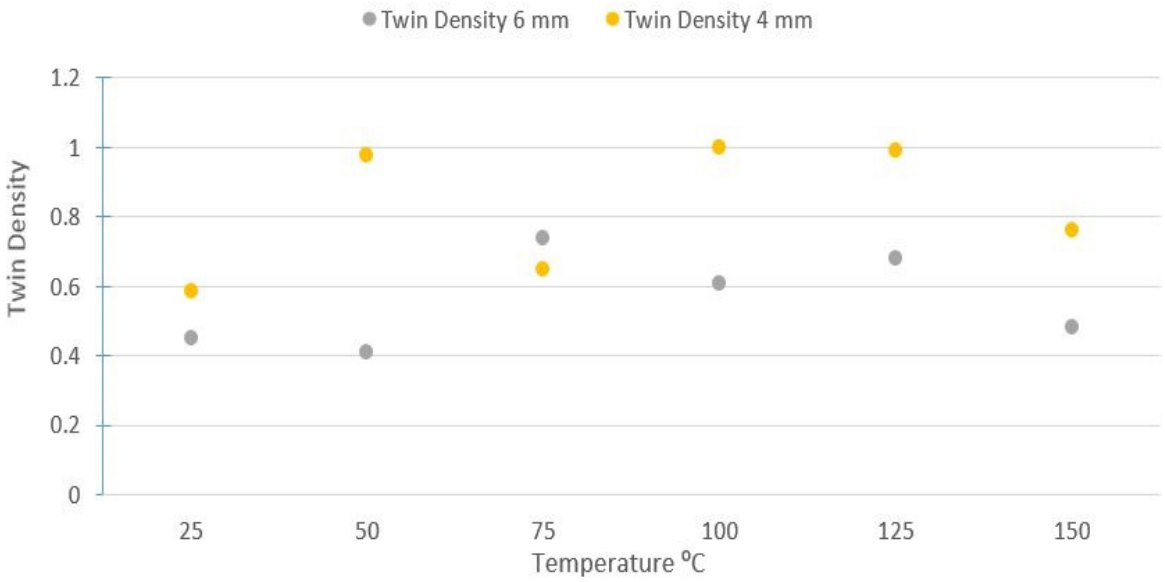

Figure 4-3: Twin density vs temperature for specimens deformed by LDH dome heights of 6 mm and 4 mm.

The primary twinning mechanism of $\{10\bar{1}1\}$ twins gives rise to thin twin lamellas within the grains and the 0.3 μm step size used for the EBSD scan does not seem to be sufficient to define the twin areas with the required detail for the software to establish them as twins. Furthermore, the analysis tool does not have the capacity to identify secondary twins or double twins in the microstructure by default and even when programmed to find these twin systems, they are not identified entirely. Having said that, it is still successful in establishing the formation of double twins originating from within the initial compression twins. Compared to all of the twin types identified in the microstructures, the $\langle 11\bar{2}0\rangle$ 38° double twins were the ones observed

with the greatest frequency, for both specimens tested both punch heights and at all temperatures. The formation of these twins even at low temperatures is an interesting observation as it would mean that twin simulation models need to account for double twinning even at room temperature.

To understand the evolution of twin structures with increasing temperatures, twin aspect ratios were studied. This was determined by first obtaining a "Twin Parent/Daughter" map generated by OIM Analysis (figure 4-4 and 4-5) using definitions for the twin systems of interest and processing the resulting image in MATLAB to isolate regions classified as twins. In order to get a measurement of twin lengths and twin thickness, the twins are treated as elliptical areas where major and minor axes (representing twin length and twin thickness) were fitted to each twin. The aspect ratio was calculated for each twin as the minor axis divided by the major axis. An average was then taken. Size was determined by multiplying the number of pixels in each twin by a unit area of the step size squared. The results of this analysis did not show any significant changes in twin length or twin thickness for increasing temperatures. But the fact that the minor axis of contraction twins does not change significantly with temperature further supports the OIM analysis that indicated the presence of double twins. The rapid transition from contraction to double twins by the formation of extension twins within the initially formed contraction twins could be a dominant factor in influencing twin growth and shape evolution for AZ31B material under biaxial stretching. Upon formation of these extension twins, the contraction twin stops growing because of loss of coherency with the matrix leading to more opportunities of failure within the microstructure of AZ31B under such types of load (Knezevic et al. 2010). However, a more detailed study with additional strain steps is required to observe trends in formation of twins earlier along the strain path.

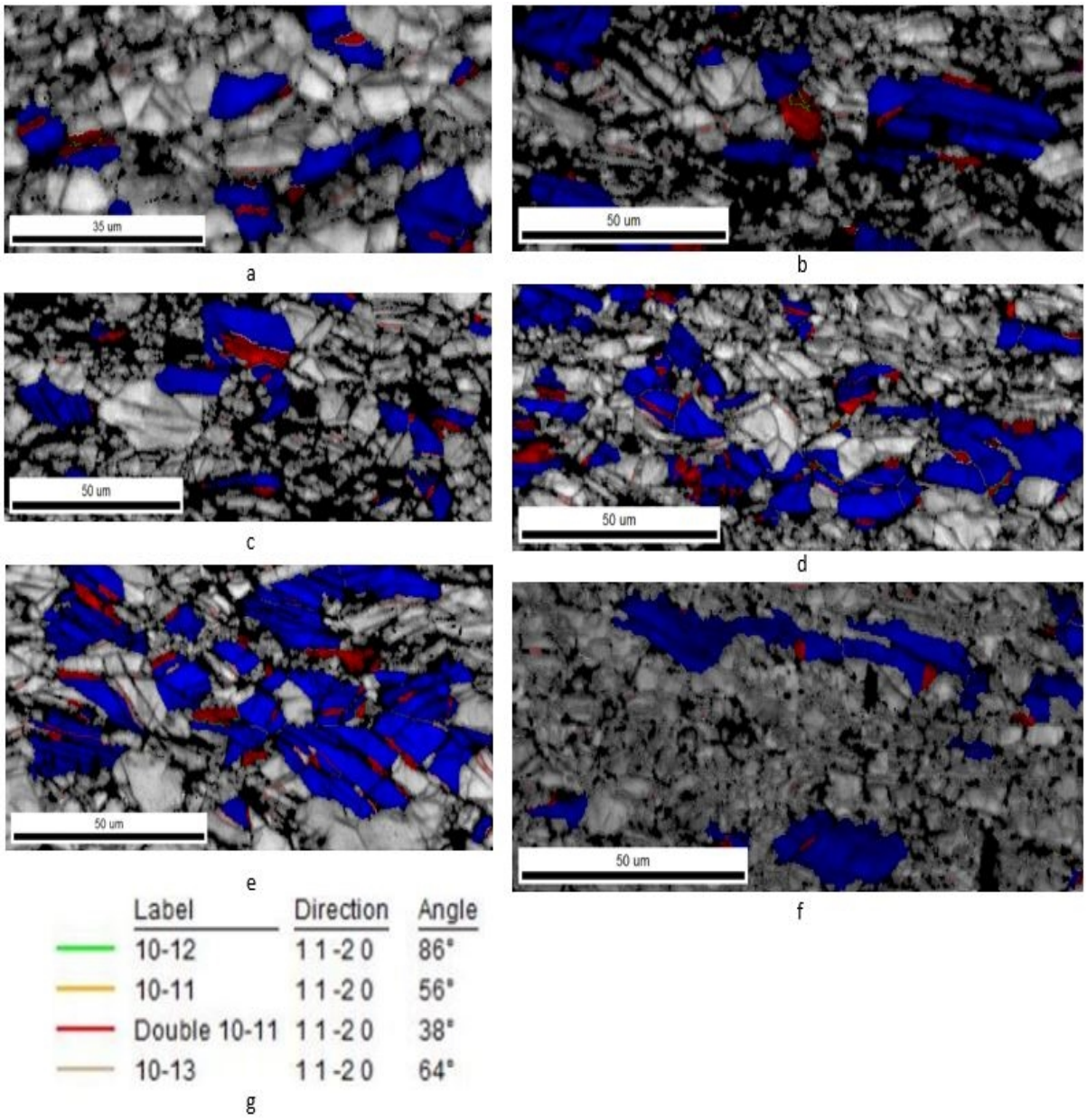

Figure 4-4: Twin parent maps of representative regions along on the ND plane after biaxial stretching for 6 mm of punch travel at (a) 25ºC, (b) 50ºC, (c) 75ºC, (d) 100ºC, (e) 125ºC and (f) 150 ºC. (g) Legends for different twin systems.

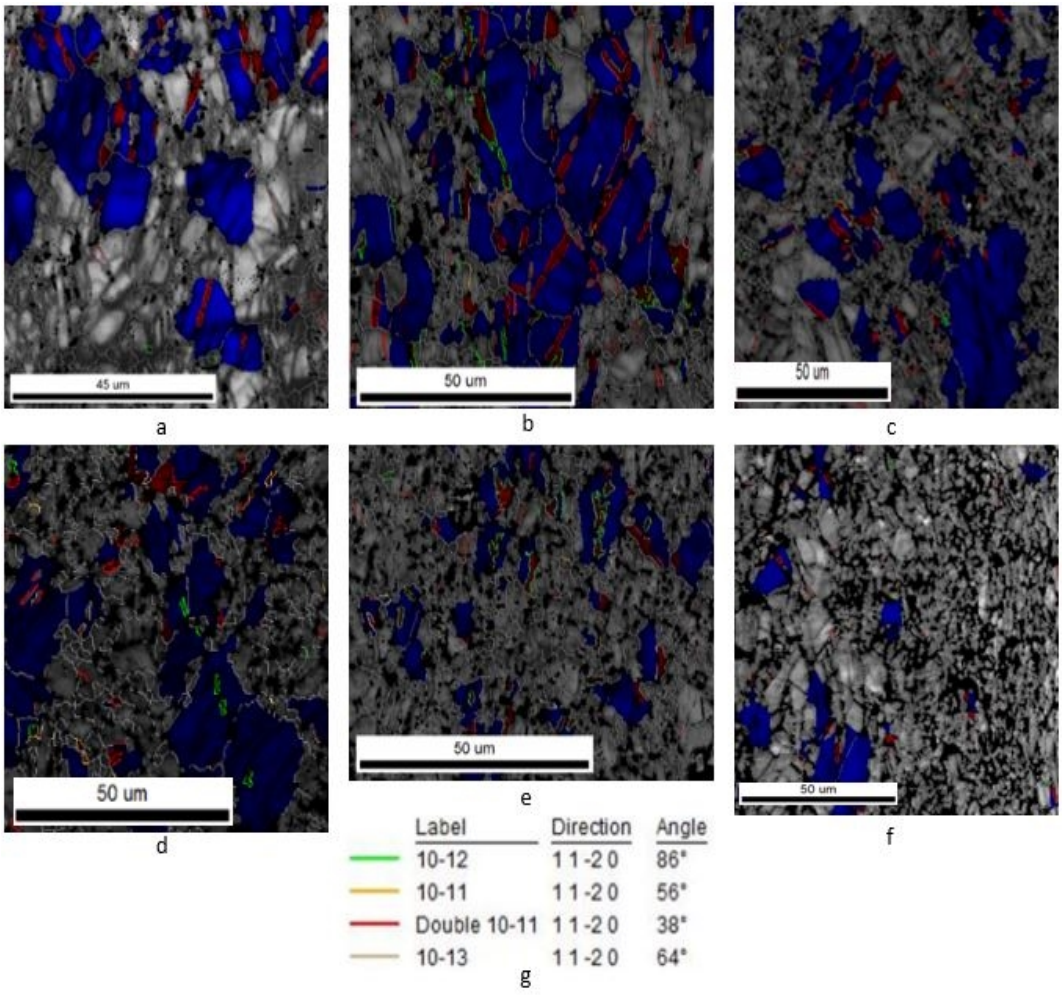

Figure 4-5: Twin parent maps of representative regions along the ND plane after biaxial stretching for 4 mm of punch travel at (a) 25ºC, (b) 50ºC, (c) 75ºC, (d) 100ºC, (e) 125ºC and (f) 150 ºC. (g) Legends for different twin system.

In anticipation of quantifying both twin and slip activity during this study, relative activity of various deformation mechanisms in AZ31B were estimated as a function of temperature based upon predicted CRSS evolution with temperature from a recently published constitutive model (Ardeljan et al. 2016). The following temperature dependencies were used for the CRSS of AZ31B slip systems:

$$\tau_0^{basal} = 17e^{(-T/786)}, \tau_0^{prism} = 108e^{(-T/359)}, \tau_0^{pyram} = 290e^{(-T/489)} \text{ (MPa)} \qquad \textbf{\textit{(4-4)}}$$

where T is the temperature (K).

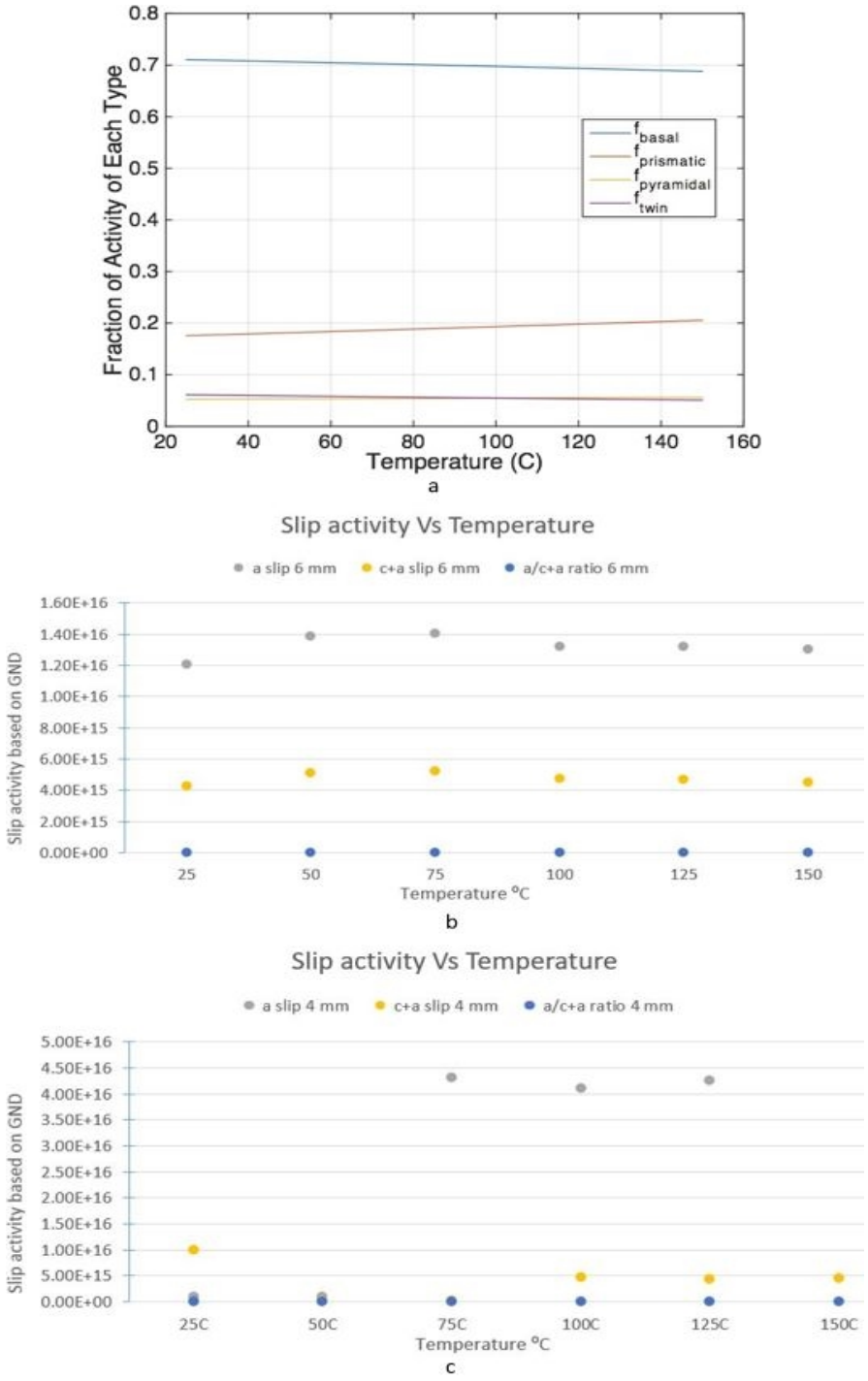

Figure 4-6: (a) Predicted relative slip and twinning activity as a function of forming temperature based upon a CRSS law. (b) Slip activity for the specimens deformed biaxially for 6 mm of punch travel at different temperatures. (c) Slip activity for the samples deformed biaxially for 4 mm of punch travel at different temperatures.

As per current literature, the CRSS for contraction twins is assumed to be constant with temperature at 13 MPa (Ardeljan et al. 2016). If the fraction of initial slip relating to a particular mode is assumed to be proportional to the CRSS, then while the CRSS for twinning does not change with temperature, the relative amount of slip will change slightly as depicted in figure 4-6a. The observed trend in slip activity obtained from the GNDs calculated in the tested specimens is slightly upwards as seen in figure 4-6b and 4-6c.

This could possibly point to a need for review of the assumptions made in the model used for simulations. The scattering noticed in figure 4-6c at initial temperatures can be attributed to low quality scans. However, at higher temperatures for the same test specimen an upward trend similar to the one in the 6 mm test specimen is observed.

4.4 Conclusions

Biaxial forming experiments over the temperature range from 25-150°C were carried out on a double action hydraulic press, where the punch strokes of 4 mm and 6 mm for used for each temperature. Strain ratios measured by DIC on the surface of the sheet showed that stretching was biaxial throughout each test. Load versus punch stroke curves were similar at both 25°C and 50°C, while the loads began to decrease at 75°C and higher. Specimens cut from the pole of each sheet were analyzed for twin density, GND content, and slip activity. Twin densities were not much changed given the scatter in the data over the complete range of forming temperatures. Contraction twins that were initially formed rapidly transformed into secondary (double) twins to accommodate the deformation caused by stretching. The ratio of <a>/<c+a> slip appeared to be relatively constant over the entire range of forming temperatures. However, basal slip decreased mildly over the temperature range, while prismatic and pyramidal slip showed mild increases.

The increase in non-basal slip would help in accommodating through thickness strains during biaxial stretching while also resulting in the decreased forming loads that were observed as forming temperatures were increased.

5 3-DIMENSIONAL STUDY OF QP1180 MICROSTRUCTURE TO UNDERSTAND THE INFLUENCE OF MORPHOLOGY AND ORIENTATION ON RETAINED AUSTENITE TRANSFORMATION DURING UNIAXIAL TENSION.

5.1 Chapter Introduction

The final hypothesis that, "a *3 dimensional study about the transformation of retained austenite in QP1180 advanced high strength steel will reveal more detailed relationships between transformation rate and the morphology and orientation of the retained austenite*" is investigated in this chapter of the thesis.

The effect of morphology and directionality of the orientation of retained austenite (RA) grains on its transformation is studied using 3 dimensional microstructures collected from an unstrained sample and a strained sample. The strain on this sample is at ~8.4% engineering strain. The introduction section of this dissertation contains discussion of the features considered to be major influences in RA transformation. Among them, the orientation and morphology is briefly explained in the following paragraphs.

If a RA grain is oriented favorably towards its habit plane, it can promote shear along that plane. It has been reported that when this RA transforms, it is divided into packets of martensitic lath with the same habit plane. Each packet is also subdivided into blocks of lath with the same crystallographic orientation (Marder and Krauss 1967; Marder and Marder 1969). The crystallographic orientation relationships (OR) are defined using the Kurdjumov–Sachs (K-S) relationship in this analysis (Kral 2012). The K-S relationship is one of the most frequently cited OR's for fcc – bcc interphase boundaries and has been found to be prevalent in low carbon steels (Kelly, Jostsons, and Blake 1990). This OR defines 24 different variants of lath martensite.

Subsequently, assuming that this relationship between austenite and martensite is fixed, Morito et al (Morito et al. 2003; Morito et al. 2005; Morito, Adachi, and Ohba 2009) obtained the shape strain for each martensite variant using the phenomenological theory of martensite crystallography developed by Kelly (Kelly 1992). Based on Morito's work, the habit plane of **(0.49714 0.71113 0.49714)** and shear direction of **[-0.2343 0.6617 -0.7121]** was calculated and used in this analysis. The directionality of RA grains in the unstrained and strained samples with respect to the loading direction is analyzed along with its interdependence with morphology and this morphology classification scheme is described below.

With respect to RA grain morphology, there are two types typically addressed in the present literature (Diego-Calderon et al. 2016; Chiang et al. 2011). They are lamellar or lathe like and blocky RA. At low strains the microstructure with globular shape RA (equiaxed) is shown to have higher work hardening rate due to the ease of transformation of the RA with this morphology; however, the material fails once the hardening capacity has been exhausted. On the other hand, the microstructure with lath shaped RA (lamellar) is shown to have better work hardening behavior across the range of deformation, arising from the desired uniform transformation rate, and improved ductility. The difference is shown in figure 5-1.

Observation of the different morphologies and orientations along with their behavior under deformation is accomplished by using different characterization techniques. But such characterization of morphologies during RA transformation has been difficult using existing microscopic techniques and many attempts have been made to understand RA transformation. The identification of globular and lamellar RA is subject to the location of the grain along the thickness of the region of interest and the use of 2D characterization techniques does not provide the below surface information needed to fully identify their actual morphology. The use of

multiple characterization techniques such as TEM, magnetic resonance, XRD, etc. has been suggested to obtain any missing information necessary to characterize RA transformation (for example (Haidemenopoulos et al. 2018)).

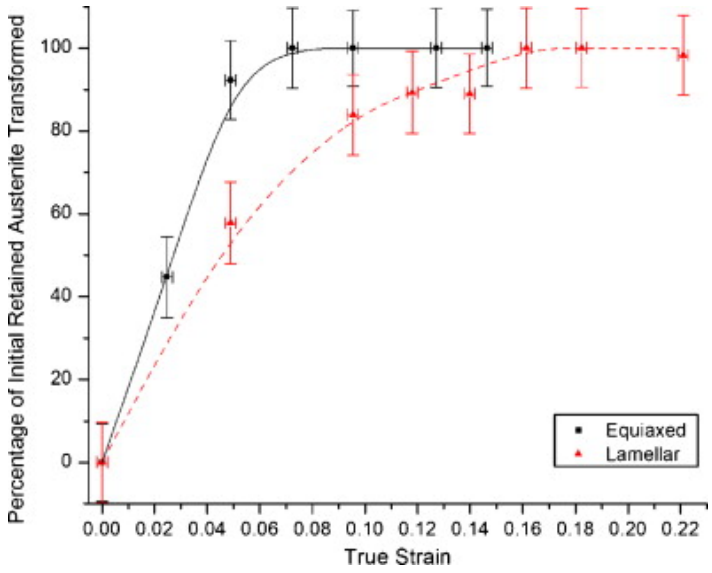

Figure 5-1: Percentage of initial retained austenite transformed as a function of strain for equiaxed and lamellar shapes with bainite hold of 100s at 450°C (Chiang et al. 2011).

However, such a combination of the different 2D characterization methods does not provide reliable information for the microstructure below the surface either. Another possible solution to provide the needed 3D information using 2D characterization techniques, it has been proposed that they can be coupled with stereological models (Russ and DeHoff 2000). But, most of these models are limited to lower-order moments of microstructural parameter distributions and are not adept at predicting the higher-order moments (Dehoff 1983). Hence information needed for generating accurate FEA models such as, grain morphology, local neighborhood information, and grain boundary network information cannot be accurately acquired using them.

In comparison to stereological modeling, a 3D microstructure can be more readily obtained by reconstruction from stacked group of 2D data (Groeber et al. 2006). The 2D data can

be captured by characterizing surfaces of different sections one after the other using EBSD in an SEM. The serial sectioning method is time and labor intensive but provides an accurate representation of the overall microstructure. From this 3D element, information about the RA grains can be obtained.

5.2 Methodology

QP1180 tensile samples are cut from a 1 mm thick rolled sheet metal such that the rolling direction of the sheet is along the short direction of the tensile sample as shown in figure 5-2. One of the samples is subjected to uniaxial tension, using an insitu stage till ~8.4% strain. From a previous study, this was noted to be the strain at which there is partial transformation of the RA grains initially present in the microstructure (Cramer et al. 2018).

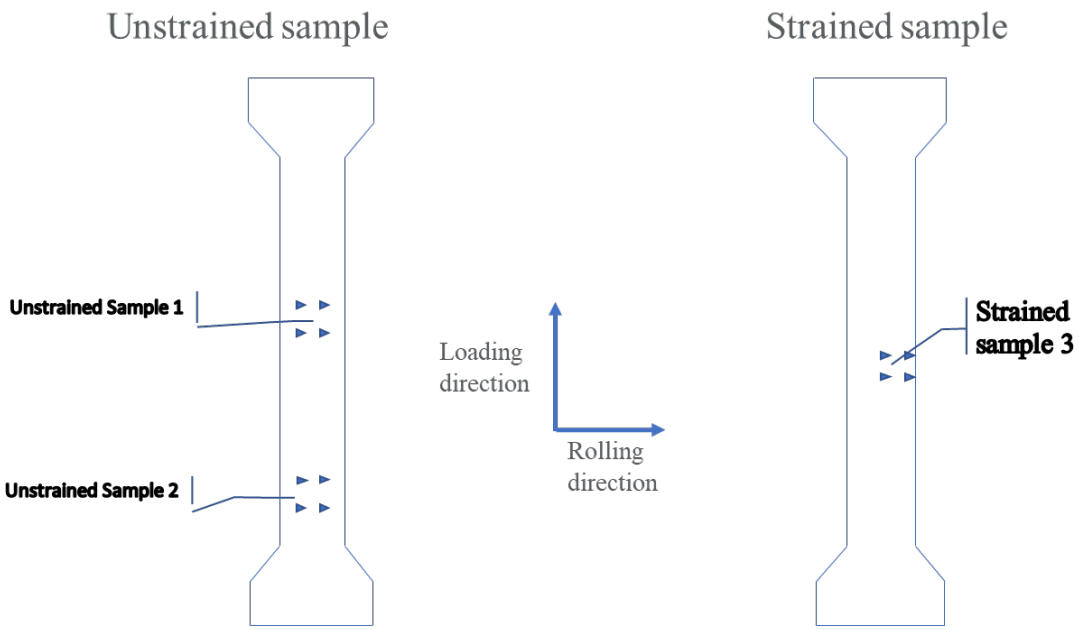

Figure 5-2: Graphical representation of QP1180 tensile samples.

One unstrained and strained sample is polished manually and embedded with fiducials to mark the area where the EBSD scans are to be performed. After each scan is completed (scan details are given below), the surface is polished with colloidal silica for 25-30 seconds manually to remove material from the surface. This process is repeated to get 9 sections for the unstrained sample and 16 sections for the strained sample. The total depth of the 3 dimensional volume element is 1.529 µm and 1.309 µm respectively for the two locations in the unstrained sample with an average of 180 nm and 150 nm removed between each sections in the two samples. For the strained sample 3.24 µm of material was removed at an average of 173 nm between each section. The data acquisition process is shown in figure 5-3.

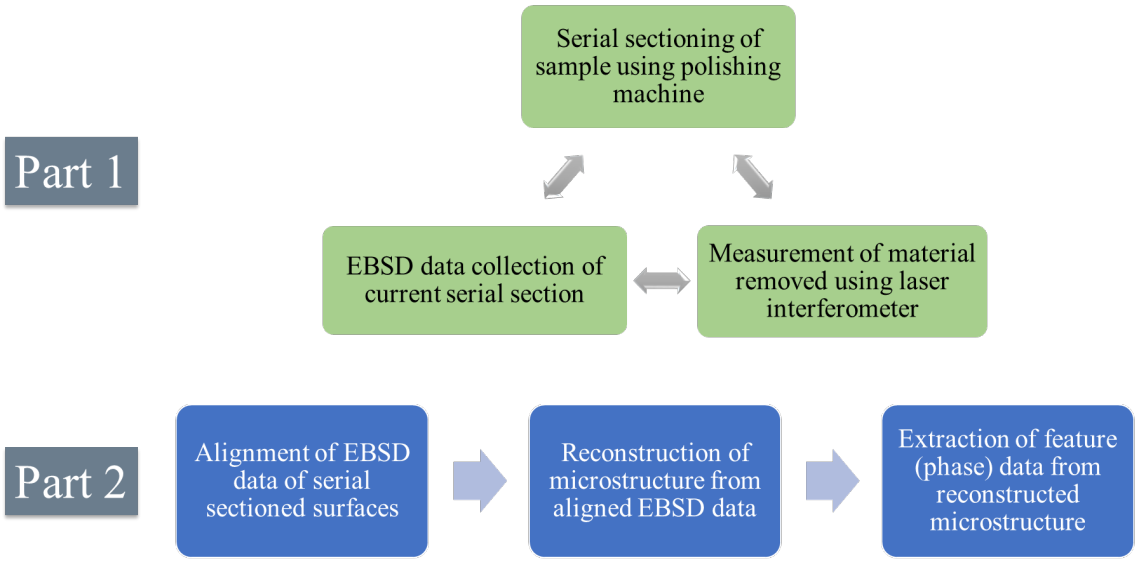

Figure 5-3: Graphical representation of data acquisition process for 3D EBSD by serial sectioning and 3D reconstruction using DREAM 3D.

The process is explained in two-parts. Part 1 is the sample preparation and EBSD data collection process. EBSD is performed over an area of 40 x 40 μm^2 with a step size of 0.08 µm using a scanning electron microscope with a EDAX® EBSD data acquisition system. The EBSD

data is processed such that any data point with confidence interval less than 0.1 is removed using the TSL OIM Analysis® tool to reduce the noise in data collected. Part 2 involves taking the individual 2D EBSD data and then stacking them over one another to reconstruct an accurate 3D microstructure using Dream 3D.

DREAM 3D is an open source, cross-platform and modular software package that allows users to reconstruct, instantiate, quantify, mesh, handle and visualize multidimensional, multimodal data (Brahme et al. 2006; Saylor et al. 2004). Using DREAM 3D to reconstruct a 3 dimensional microstructure we can detail the neighborhood of several RA grains before and after transformation. The resulting 3D data is analyzed the influence of RA morphology with its transformation into martensite.

When Dream 3D reconstructs a RA grain/feature it represents its shape as an ellipsoid in such a way that the major axis is always known as the ***a-axis*** and the minor axis is always the ***c-axis***. And the axis with length between ***a*** and ***c-axis*** length is always designated as the ***b-axis***. Thus the relation between the three axis' is given as length(a) > length(b) > length(c). From their aspect ratio, namely b/a and c/b, we can categorize them into distinct morphologies. If the aspect ratios are closer to one, then the RA grain will be closer to a spherical shape. If the aspect ratio of the biggest axes (b/a) is small and the one between the smaller axes (c/b) is very large, then its shape will be a lenticular shape. Because the RA shape can be visualized in three dimensions, a third shape, where the length of the b-axis is greater than half the length of a-axis and the other aspect ratio, c/b is very small, is a disk-like shape. The visualization of the adopted classification is shown in figure 5-4b. Thus using these two aspect ratios the RA grain morphology can be defined as follows,

1. **globular:** when b/a aspect ratio is greater than 0.49 and c/b aspect ratio is greater than 0.79,
2. **disk:** when b/a aspect ratio is greater than 0.49 and c/b aspect ratio is lesser than 0.79,
3. **lath:** when the aspect ratio b/a is < 0.49.

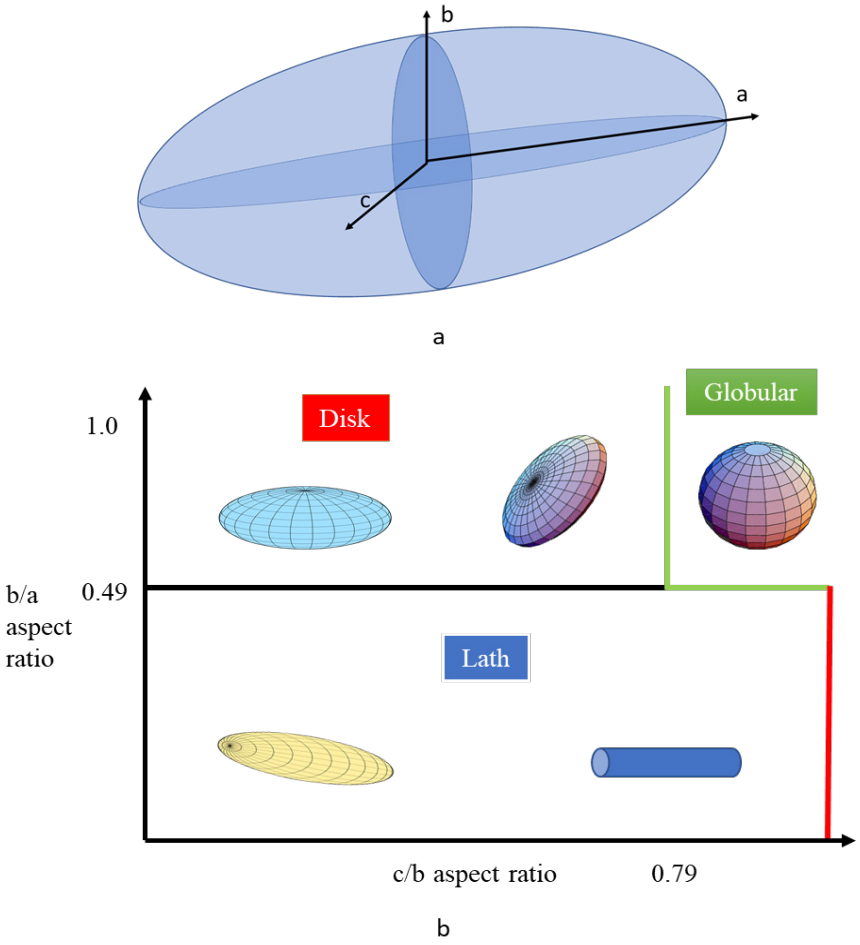

Figure 5-4: a. Ellipsoid reconstruction of the grain by DREAM 3D. b. Morphological classification of Retained Austenite based on aspect ratio.

After determining the bounds for the different morphologies, the size of the RA grains is checked to see if they have adequate resolution for morphology classification. The resolution along the x-y plane is 0.08 μm for both unstrained and strained datasets. For the unstrained data the resolution along the z axis (i.e. the average distance between the different sections) is ~165

nm. For the strained data the resolution along the z axis is ~173 nm. Thus one pixel of data in such a volumetric representation is approximately of size 0.0011 μm^3. Comparatively, the minimum size of the RA grain in the actual reconstructed dataset is 0.00112 μm^3, which is very close to the size of one pixel. Hence, to improve the accuracy of the reconstruction, we introduce a size threshold of 125 pixels for a grain. As such, the minimum size for a reconstructed RA grain to be 0.14 μm^3 and the reconstructed grains have adequate resolution to be categorized into different morphologies.

The final distribution of the morphology is shown in figure 5-5. There was one globular shaped RA grain identified in the unstrained sample and no grains with globular shape for the strained sample. As such it is excluded from the figure. It is however included in a scatter plot that shows how the RA grains are distributed according to their morphology in figure 5-6.

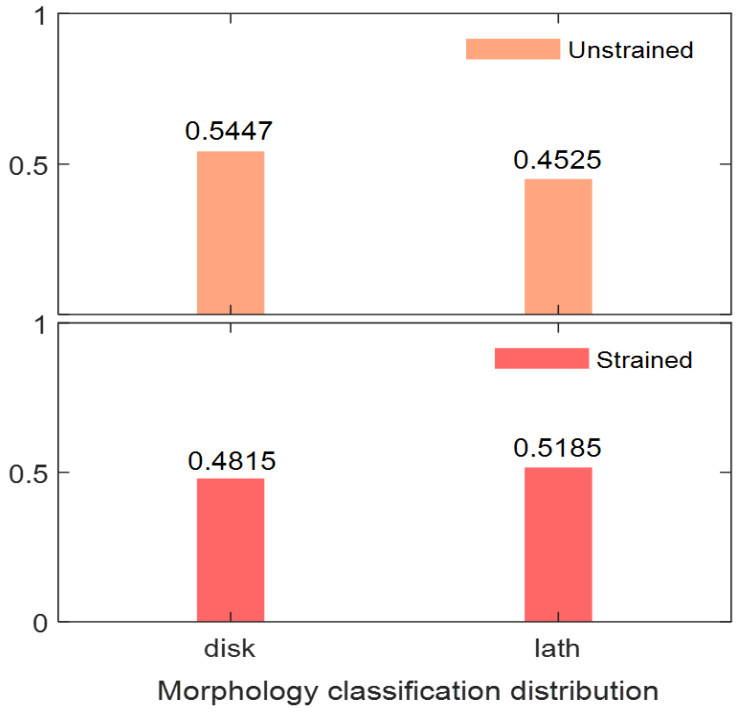

Figure 5-5: Distribution of morphology for both unstrained and strained samples for the dataset with size threshold used.

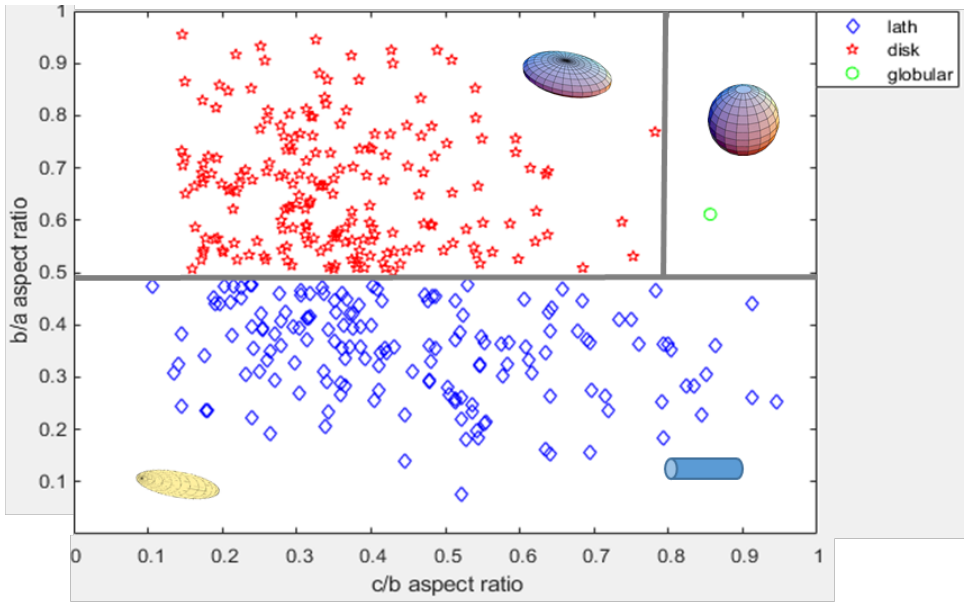

a

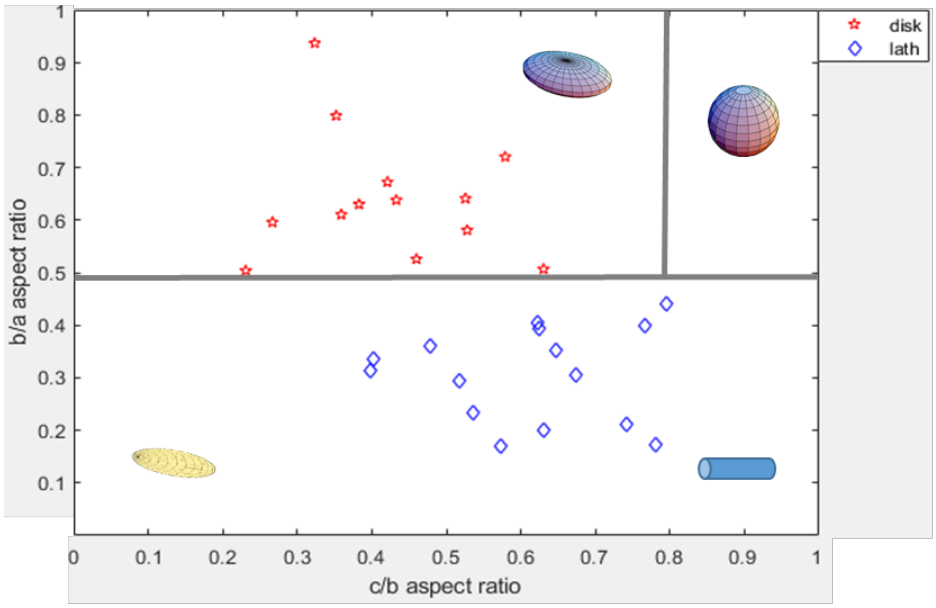

b

Figure 5-6: Distribution of Retained Austenite grains according to morphology show for a. Unstrained sample and b. Strained sample. Refer to figure 4-4b for clarification on the clarification about the different shapes shown here.

Dream3D also allows the user to export several attributes of RA grains that help define the reconstructed microstructure. The theoretical validations for the calculation of these attributes are established in the Dream3D website in its help files and in publications listed in these help

files (Rollett, Campman, and Saylor 2006; Wang et al. 2011). In this study we are concerned with the feature attributes that provide information about morphology and its influence on the transformation of RA grains. Table 5-1 shows a list of the attributes that have been chosen for this study.

Table 5-1: Feature (grain) attributes extracted from Dream3D

Attributes extracted from Dream3D	***Attribute information***
Aspect Ratio b/a	Morphology
Aspect Ratio c/a	Morphology
Semi Axis Length	Morphology
Euler orientation of feature in radian	Orientation
Equivalent Diameter of feature	Morphology
Number of features in contact with a feature of interest	Neighborhood
Phase of feature	Material information
Volume of feature	Morphology
Deviation of shear plane normal from loading direction	Material texture
Average misorientation of feature with all of its neighbors	Orientation
Rotation needed for the axis of the reconstructed feature to align with the sample reference frame	Orientation

5.3 Results and Discussion

Having reconstructed the microstructure for the unstrained and strained samples, we proceed to compare the distribution of their features to understand the influence of morphology on the transformation of RA grains. But before proceeding with the analysis, the impact of some

of the RA grains being sectioned off by the surface/edge of the reconstructed volume element should be considered. Figure 5-7a shows that within the reconstructed element, three fourths of the RA grains touch the surface for the unstrained sample and for the strained sample two thirds of the reconstructed grains touch the surface. As such, an inherent bias may be present in the dataset since the majority of the minor c-axes lie parallel to the through thickness direction. The distribution of c-axis lengths for both samples is used to understand the impact of this bias on the analysis. As seen in figure 5-7b, all RA grains that touch the surface only touch a single surface (they do not span the sample).

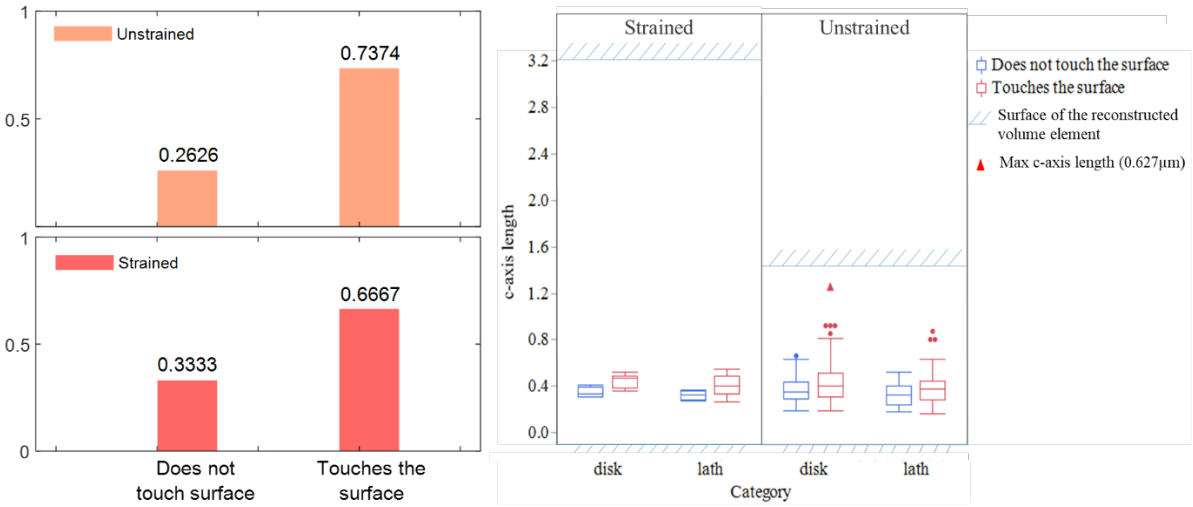

Figure 5-7: a. Shows the fraction of the RA grains that touch the edges of the reconstructed microstructure element for both unstrained and strained sample. b. The distribution of c axis length is shown for each group and for both shapes.

Additionally, the average c-axis length for RA grains that touch the surface for both unstrained and strained sample is far less than the total depth of the sample acquired, as described in the methodology section. It is therefore reasonable to conclude that even if the sample might possess a slight bias in morphological characteristics measured in the z (i.e. the sample thickness) direction, the trend seen in the preferential alignment of the minor axis of the reconstructed grain along the through thickness direction appears correct.

First we look at the impact of morphology as a single attribute on RA transformation. When the aspect ratios of the RA grains (used here to define its morphology) in the unstrained and strained samples are compared, as in figure 5-6, there is a clear difference in the regions of the morphology map where the RA grains are populated. The visualization of the combined distribution of both these aspect ratios shows them to be different for unstrained and strained sample group. A deeper look at the morphology distribution allows us to identify certain combinations of b/a and c/b aspect ratios that preferentially transform. RA with b/a aspect ratios that are less than 0.2 are absent in the strained data compared to the unstrained data. Similarly, if a line was drawn at a value of b/a aspect ratio equals 0.5 and c/b aspect ratio equals 0.4, RA grains to the bottom left of these lines have transformed. There are some regions of with high b/a aspect ratio (>0.8) that also transform. The region with both high b/a aspect ratio and high c/b aspect ratio have very few data points and hence the influence of morphology on transformation cannot be confidently identified for this region. In conjunction, figure 5-5 also shows that there is a slight decrease in the fraction of RA grains that are identified as disks. A trend is seen where, as QP1180 is deformed the disks are reduced and laths occupy more of the microstructure. As established in literature, this would indicate that blocky RA grains are less stable compared to lamellar or lath shaped RA grains.

We now look for significant changes in microstructural attributes that are caused by plastic deformation, and associated transformation of the RA. Significant differences in the distributions of each attribute between the unstrained and strained samples are identified using p values from a non-parametric Wilcoxon signed ranked test for each attribute. A significant p value (assumed to be those below 0.05) denotes a difference in attribute distribution that indicates that the selected attribute has been affected by the plastic deformation, and presumably

by the RA transformation process. When the distribution of RA grains with a certain attribute significantly decreases, it is likely that the attribute is influencing the RA transformation rate. The results of this statistical analysis is presented in table 5-2.

Table 5-2: List of p-values for different attributes of RA grains according to Wilcoxon signed rank test between unstrained and strained groups. Significant p-values are highlighted in bold

Attribute	***p-value***
Average Misorientation	**0.0326**
Volume	**0.0007**
a-axis misorientation with tensile axis	0.2684
b-axis misorientation with tensile axis	0.1670
c-axis misorientation with tensile axis	0.1562
Deviation of close packed plane from tensile axis	**<0.0001**
Shear affinity factor	**0.0002**
a-axis length	0.2094
b-axis length	**0.0009**
c-axis length	0.2863

For the attributes that show a significant change in distribution after straining the sample (table 5-2), we now consider the combined effect of the microstructural attributes and the morphological aspect ratios based classification as discussed earlier. This is performed visually by mapping a given attribute onto the convex hull of data points presented on the morphological map that is shown in figure 5-6b.

First, the distributions of RA grain volume for the unstrained and strained samples, with respect to their morphology, are shown in figure 5-8. Most of the RA grains in the unstrained sample are of a size less than 0.7 μm^3. Consideration of the strained map indicates that RA grains

with volume greater than 0.52 μm^3 have transformed; a more detailed analysis of the data indicates that laths with volume between 0.32 – 0.52 μm^3 are also transformed. To understand this deviation, the orientation of the 3 ellipsoidal axes is analyzed. A large fraction of a-axis (major axis) is oriented towards the rolling direction as expected and the b and c axes are oriented towards the loading and through thickness direction respectively. And an analysis, that is discussed later in this section about the change in axis length shows that RA with large a and b axes transform preferentially. Laths in this data are defined to have larger a axes and it can be inferred that the low volume laths that have transformed have large a axes that promote their transformation before large volume RA disks. This data shows that a majority of large volume RA grains transform faster than smaller shapes supporting existing hypotheses (Xiong et al. 2013; Shen et al. 2015), but highlights a possible influence of the length of the major axis on how these large volume RA's transform.

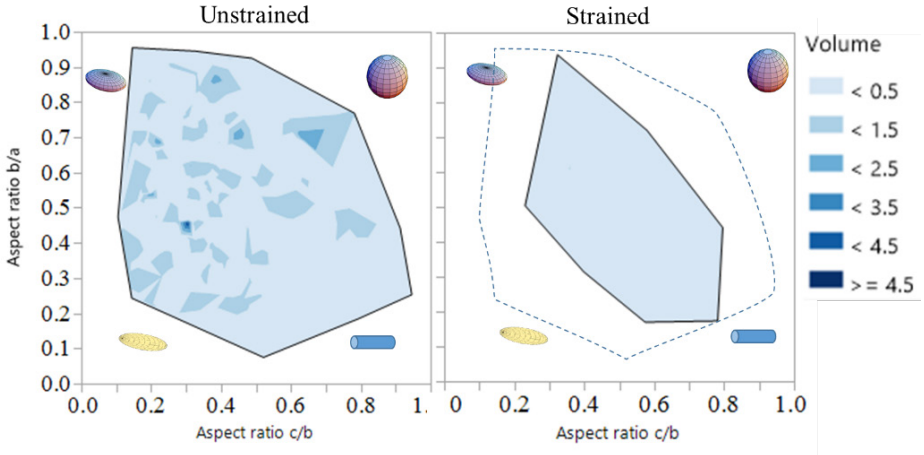

Figure 5-8: Density map showing distribution of volume of reconstructed RA shape for unstrained and strained samples.

Next the deviation of the close packed plane from the tensile force axis, shown in figure 5-9 a and b, is analyzed. Figure 5-9a shows the distribution of misorientations of close packed

plane from tensile axis for unstrained and strained RA grains. The difference between the two distributions points to a significant correlation between this attribute and transformation of RA. After a deformation of ~8.4% strain, all the RA grains with deviation of less than 57.5° between the [110] tensile axis and the (111) close packed plane have transformed. Large deviations appear to make the RA grains more stable. The overlay of this attribute onto the morphological aspect ratio space does not show any clear combined effects as seen in Figure 5-9b.

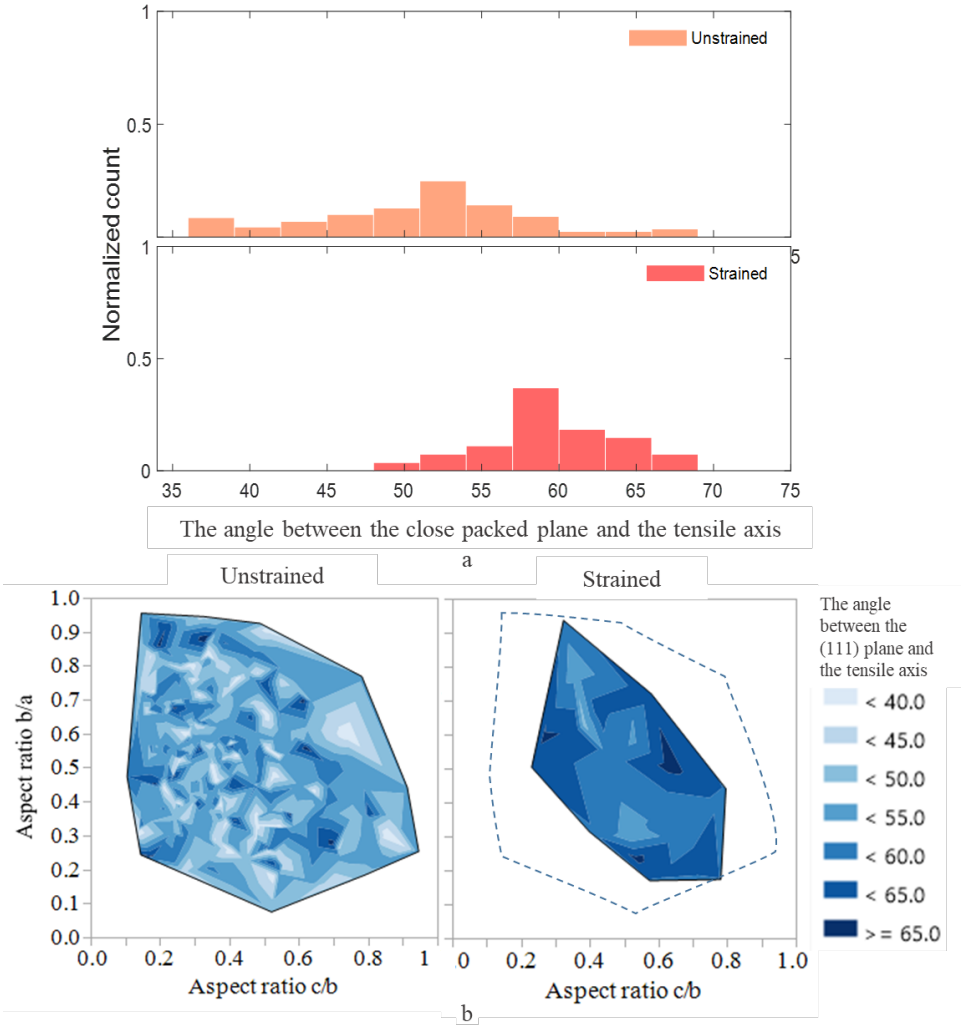

Figure 5-9: a. Distribution of deviation of closely packed plane with the tensile force direction for unstrained and strained samples. b. Density map showing distribution of schmid factor for unstrained and strained samples according to morphology.

Along with the angle between the tensile axis and the close packed plane, the local 'average misorientation' of the grain is also a likely influencer of RA transformation. Here, average misorientation indicates the mean misorientation between an RA grain and each of its neighbors. When a RA grain has higher misorientation with its neighbors, the neighborhood of that grain makes it difficult for it to re-orient itself in the direction of the shape strain for activation of martensitic transformation. With low misorientation with its neighbors, the region will be able to experience strain localization that will help it to more favorably re-orient and activate martensitic transformation of RA. The distribution of average misorientation according to morphology is shown in figure 5-10. The maps show that RA grains with low average misorientation angles (between 0°-37°) are completely transformed for lath shaped RA grains. For disk shaped RA grains this transformation zone extends from 0° to 42.5°.

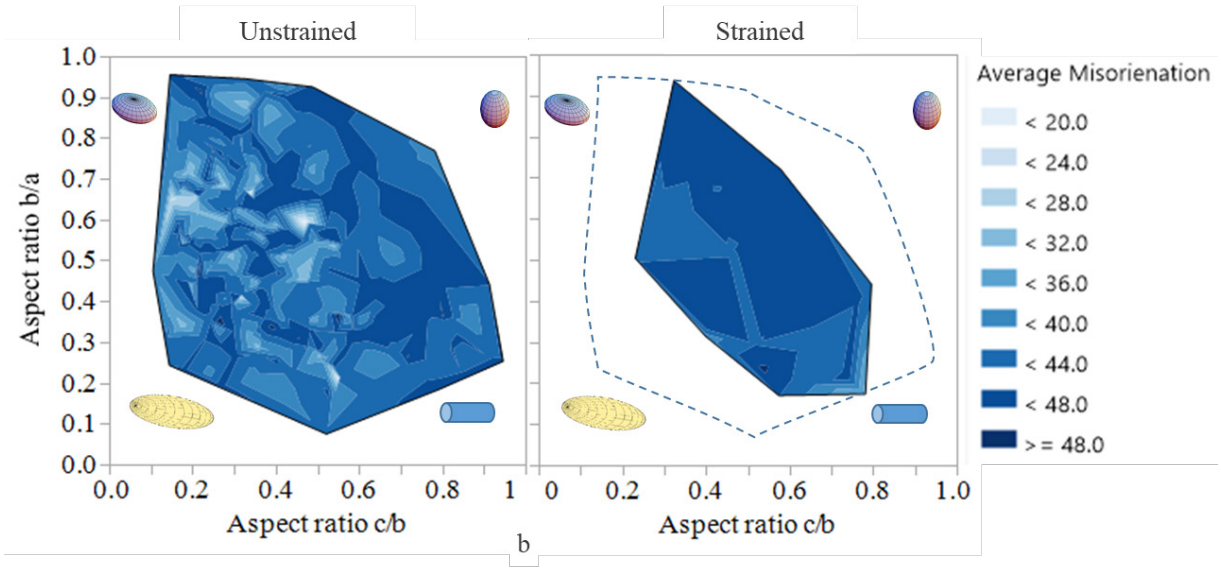

Figure 5-10: Density map showing distribution of average misorientation of retained austenite grains with neighbors according to morphology.

A shear affinity factor (*saf*) is introduced, where instead of using a slip plane and slip direction to calculate a traditional schmid factor, the habit plane and the shear direction are used to calculate the saf of a grain. The saf for all 24 variants is the K-S orientation relationship is calculated and the maximum value is reported as the saf for the RA grain as shown in equation 5-1.

$$shear\ affinity\ factor = \max_{i=1:24} (\cos(\theta_i) . \cos(\lambda_i)) \qquad 5\text{-}1$$

where, i is the number of a given variant, and θ and λ are the angle of the habit plane and shape strain direction with the tensile axis of the sample respectively.

High saf indicates that the RA grain is oriented closer to the shape strain direction. Figure 5-11a shows the distribution for the saf for the unstrained and strained samples. The unstrained sample has a larger distribution of high saf RA grains than the strained sample. Figure 5-11b shows how the saf is distributed according to the morphology classification. SAF between 0.43 and 0.5 are not observed for the strained sample except for an outlier. Thus higher saf are almost nonexistent in the strained sample indicating that these RA grains (with high saf) have been transformed.

Additionally, deviation of the major axis away from the loading direction, listed in table 5-2, is also analyzed for any correlations to test whether there may be a significant correlation with strain / transformation when combined with morphology. The deviation of the major axis away from the loading direction can influence how much area of the RA grain is exposed to the tensile force. The distribution shown in figure 5-12a does not show any major differences. But when morphology is introduced to this distribution (figure 5-12b) it can be seen that disks with a high angle deviation have transformed (between 80.5°-90°) and laths with low angle deviations (between 5°-50°) have transformed.

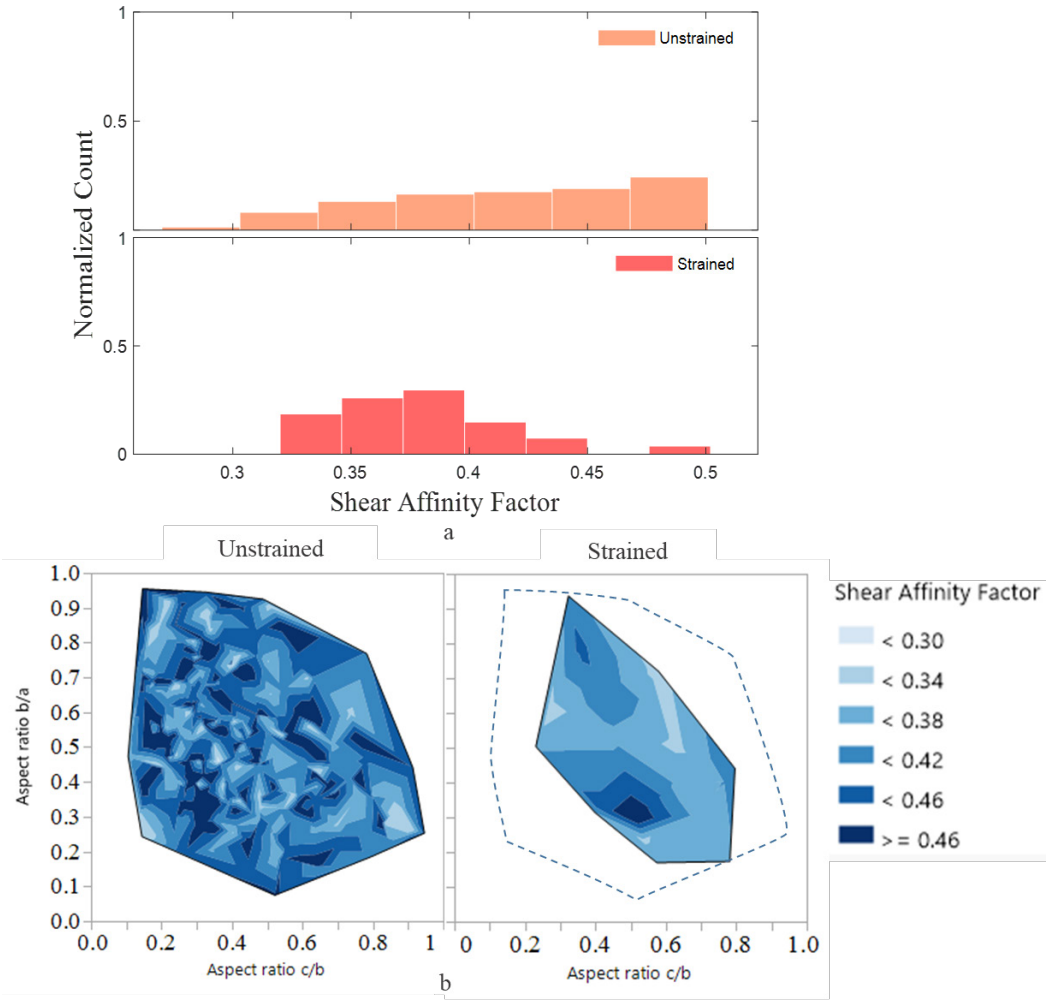

Figure 5-11: a. Distribution of shear affinity factor for unstrained and strained samples. b. Density map showing distribution of the same for unstrained and strained samples according to morphology.

The final attribute showing a significant change in distribution with strain in table 5-2 is the b-axis length. RA grains with longer b-axis lengths (between 1.34 µm and 2.84 µm) have transformed for both disk and lath shapes after straining the sample. Also, RA with longer a-axis lengths (between 2.86 µm – 6.24 µm) have transformed for disks while RA laths having a-axis lengths between 2.86 µm – 6.24 µm and between 1.8 µm and 2.2 µm have also transformed. Both these axes lie on the plane containing the rolling and transverse directions. Thus, under uniaxial tension, for RA grains having a and b ellipsoidal axes lying on the plane where the

tensile axis acts, those grains having longer axes transform preferentially. On the other hand, disk RA with smaller c-axis lengths (0 – 0.28 μm) and lath RA with c-axis lengths between 0.4 μm and 0.56 μm appear to transform. However, this correlation cannot be confirmed to be significant because of the low number of data points in each of the regions of interest.

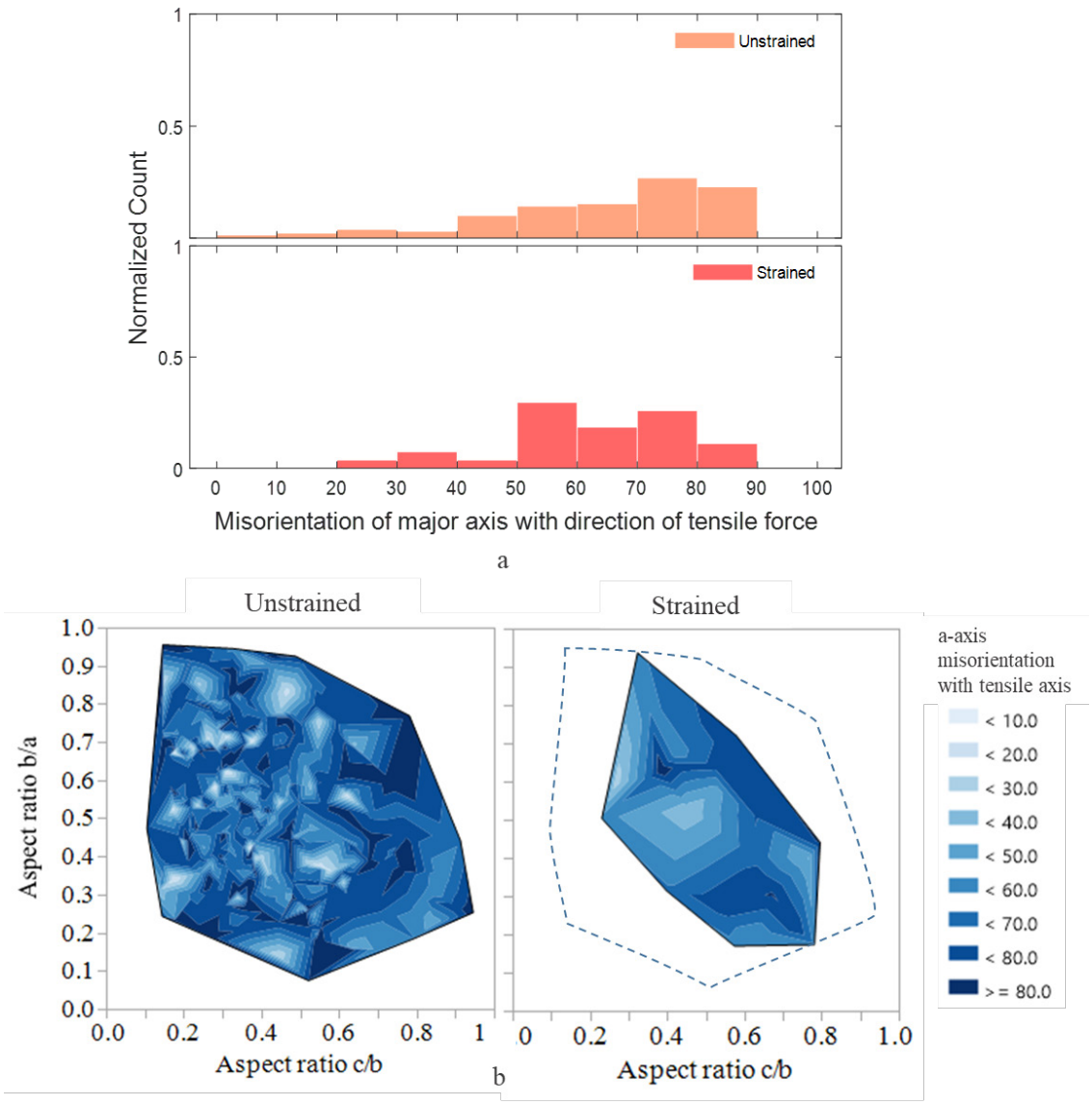

Figure 5-12: a. Distribution observed for the orientation of the major axis (in degrees) of reconstructed RA grains w.r.t. the sample rolling direction. b. Density plot for the distribution of orientation of major axis with loading axis for unstrained and strained samples.

5.4 Conclusion

The study undertaken examined the influence of morphology of retained austenite grains on their transformation using a 3 dimensional dataset. This dataset was obtained by serial sectioning strained and unstrained samples and then reconstructing a 3D microstructure using 2D EBSD scans of the individual surfaces with DREAM 3D. The dataset thus obtained was filtered to retain larger size RA grains so the morphology of these grains could be confidently defined. Subsequently, morphology was divided into 3 categories, globular, disk and lath.

The length of the c-axis for RA that touch the edges of the reconstructed volume element is observed to be on average a fourth of its total depth. As such it is reasonable to assume that the bias introduced by including grains that touch the sample surface (and therefore have a cropped z-dimension) is not severe.

The conclusions from this study are listed below, in terms of the attributes considered:

- Aspect ratios (morphology)
    - b/a aspect ratios less than 0.2 transform preferentially at ~8% strain.
    - RA below a line drawn between b/a aspect ratio of 0.6 and c/b aspect ratio of 0.6 have transformed.
    - b/a aspect ratio greater than 0.8 also transform.
    - The region with both high b/a aspect ratio (>0.7) and high c/b (>0.7) aspect ratio have very few data points and hence transformation cannot be confidently identified in this region.
- Volume
    - Large volume RA grains (between 0.52 and 5 μm^3) transforms for both disk and lath shapes.

    - Lath shaped RA grains with volume between 0.32 and 0.52 μm^3
- Average misorientation with neighboring grains
    - RA with low misorientation (< 37°) transform for both disk and lath shapes.
    - Additionally, laths with average misorientation between 37° and ~43° also appear to transform
- Deviation of close packed plane from tensile axis
    - RA with deviation less than 57.5° transforms for all shapes
- Shear affinity factor
    - RA with high saf transforms for all shapes (greater than 0.43)
    - Disks with high b/a aspect ratio (>0.6) also transform. Lath RA's exist in the strained sample across all values of c/b aspect ratio.

Since large volume RA grains are seen to transform, disks, which have a tendency to have the higher volume, preferentially transform before laths. As the misorientation of a-axis or major axis of the reconstructed RA grain increases, the transformation of these grains becomes more difficult. Thus depending on at which strain level the grain should transform, we can design the shape or morphology of RA grains. Large sized RA grains with high shear affinity factor and low average grain misorientation will transform preferentially according to this study.

Other than morphology, carbon concentration and the type of martensite neighborhood are also known to heavily influence the metastable RA transformation to stable martensite. Combining the information about the morphology found from this study, it is possible to generate microstructures that will have greater affinity to transform at particular strain levels during plastic deformation. The test conducted was a uniaxial tension test. Other studies have shown that the uniaxial tension is the least effective in transforming RA grains (Cramer et al.

2018). Understanding the morphology and the physical relation between morphology and loading conditions can help with revealing additional relationship necessary to design an optimum microstructure.

REFERENCES

Abdolvand, Hamidreza, Marta Majkut, Jette Oddershede, Jonathan P. Wright, and Mark R. Daymond. 2015. 'Study of 3-D stress development in parent and twin pairs of a hexagonal close-packed polycrystal: Part II – crystal plasticity finite element modeling', *Acta Materialia*, 93: 235-45.

Agency, United States Environmental Protection. 2019. 'The 2018 EPA automotive trends report: greenhouse gas emissions, fuel economy and technology since 1975'.

Agnew, S. R., and O. Duygulu. 2005. 'Plastic anisotropy and the role of non-basal slip in magnesium alloy AZ31B', *International Journal of Plasticity*, 21: 1161-93.

Agnew, S. R., C. N. Tomé, D. W. Brown, T. M. Holden, and S. C. Vogel. 2003. 'Study of slip mechanisms in a magnesium alloy by neutron diffraction and modeling', *Scripta Materialia*, 48: 1003-08.

Agnew, S. R., M. H. Yoo, and C. N. Tome. 2001. 'Application of texture simulation to understanding mechanical behavior of Mg and solid solution alloys containing Li or Y', *Acta Materialia*, 49: 4277-89.

Al-Samman, T., and G. Gottstein. 2008. 'Room temperature formability of a magnesium AZ31 alloy: Examining the role of texture on the deformation mechanisms', *Materials Science and Engineering: A*, 488: 406-14.

Altinkok, N., and R. Koker. 2006. 'Modelling of the prediction of tensile and density properties in particle reinforced metal matrix composites by using neural networks', *Materials & Design*, 27: 625-31.

Ardeljan, Milan, Irene J. Beyerlein, Brandon A. McWilliams, and Marko Knezevic. 2016. 'Strain rate and temperature sensitive multi-level crystal plasticity model for large plastic deformation behavior: Application to AZ31 magnesium alloy', *International Journal of Plasticity*, 83: 90-109.

Ardeljan, Milan, Rodney J. McCabe, Irene J. Beyerlein, and Marko Knezevic. 2015. 'Explicit incorporation of deformation twins into crystal plasticity finite element models', *Computer Methods in Applied Mechanics and Engineering*, 295: 396-413.

Barnett, M. R. 2007a. 'Twinning and the ductility of magnesium alloys Part I: "Tension" twins', *Materials Science and Engineering a-Structural Materials Properties Microstructure and Processing*, 464: 1-7.

Barnett, M. R. 2007b. 'Twinning and the ductility of magnesium alloys Part II. "Contraction" twins', *Materials Science and Engineering a-Structural Materials Properties Microstructure and Processing*, 464: 8-16.

Barnett, M. R., Z. Keshavarz, A. G. Beer, and X. Ma. 2008. 'Non-Schmid behaviour during secondary twinning in a polycrystalline magnesium alloy', *Acta Materialia*, 56: 5-15.

Barnett, M.R., Z. Keshavarz, A.G. Beer, and D. Atwell. 2004. 'Influence of grain size on the compressive deformation of wrought Mg–3Al–1Zn', *Acta Materialia*, 52: 5093-103.

Basinger, Jay, David Fullwood, and Brent Adams. 2011. "EBSD Detail Extraction for Greater Spatial and Angular Resolution in Material Characterization." In *TMS*. San Diego.

Beyerlein, I. J., L. Capolungo, P. E. Marshall, R. J. McCabe, and C. N. Tomé. 2010. 'Statistical analyses of deformation twinning in magnesium', *Philosophical Magazine*, 90: 2161-90.

Beyerlein, I. J., R. J. McCabe, and C. N. Tomé. 2011. 'Effect of microstructure on the nucleation of deformation twins in polycrystalline high-purity magnesium: A multi-scale modeling study', *Journal of the Mechanics and Physics of Solids*, 59: 988-1003.

Beyerlein, Irene J., R. J. McCabe, and C. N. Tome. 2011. 'Stochastic processes of {1012} deformation twinning in hexagonal close-packed polycrystalline zirconium and magnesium', *International Journal for Multiscale Computational Engineering*, 9: 459-80.

Blonde, R., E. Jimenez-Melero, L. Zhao, J.P. Wright, E. Bruck, S. van der Zwaag, and N.H. van Dijk. 2012. 'High-energy X-ray diffraction study on the temperature-dependent mechanical stability of retained austenite in low-alloyed TRIP steels', *Acta Materialia*, 60: 565-77.

Brahme, A., M. H. Alvi, D. Saylor, J. Fridy, and A. D. Rollett. 2006. '3D reconstruction of microstructure in a commercial purity aluminum', *Scripta Materialia*, 55: 75-80.

Britton, T.B., and A.J. Wilkinson. 2011. 'Measurement of residual elastic strain and lattice rotations with high resolution electron backscatter diffraction', *Ultramicroscopy*, 111: 1395-404.

Capolungo, L., and I. J. Beyerlein. 2008. 'Nucleation and stability of twins in hcp metals', *Physical Review B - Condensed Matter and Materials Physics*, 78: 1-19.

Capolungo, L., I. J. Beyerlein, and C. N. Tomé. 2009. 'Slip-assisted twin growth in hexagonal close-packed metals', *Scripta Materialia*, 60: 32-35.

Chapuis, A., and J. H. Driver. 2011. 'Temperature dependency of slip and twinning in plane strain compressed magnesium single crystals', *Acta Materialia*, 59: 1986-94.

Chapuis, Adrien, and Julian Driver. 2010. "A fundamental study of the high temperature deformation mechanisms of magnesium." In *Journal of Physics: Conference Series*, 012092. IOP Publishing.

Chen, Fuh-Kuo, and Tyng-Bin Huang. 2003. 'Formability of stamping magnesium-alloy AZ31 sheets', *Journal of Materials Processing Technology*, 142: 643-47.

Chiang, J., J. D. Boyd, and A. K. Pilkey. 2015. 'Effect of microstructure on retained austenite stability and tensile behaviour in an aluminum-alloyed TRIP steel', *Materials Science and Engineering a-Structural Materials Properties Microstructure and Processing*, 638: 132-42.

Chiang, J., B. Lawrence, J. D. Boyd, and A. K. Pilkey. 2011. 'Effect of microstructure on retained austenite stability and work hardening of TRIP steels', *Materials Science and Engineering a-Structural Materials Properties Microstructure and Processing*, 528: 4516-21.

Chin, G. Y., W. F. Hosford, and D. R. Mendorf. 1969. 'Accommodation of Constrained Deformation in f.c.c. Metals by Slip and Twinning', *Proceedings of the Royal Society of London Series A-Mathematical and Physical Sciences*, 309: 433-56.

Christian, J W, and S Mahajan. 1995. 'Deformation twinning', *Progress in Materials Science*, 39: 1-157.

Cizek, P., and M. R. Barnett. 2008. 'Characteristics of the contraction twins formed close to the fracture surface in Mg-3Al-1Zn alloy deformed in tension', *Scripta Materialia*, 59: 959-62.

Cramer, J., D. Adams, M. P. Miles, D. T. Fullwood, E. R. Homer, T. Brown, R. K. Mishra, and A. Sachdev. 2018. 'Effect of strain path on forming limits and retained austenite transformation in Q&P 1180 steel', *Materials Science and Engineering a-Structural Materials Properties Microstructure and Processing*, 734: 192-99.

De Knijf, D., C. Fojer, L. A. I. Kestens, and R. Petrov. 2015. 'Factors influencing the austenite stability during tensile testing of Quenching and Partitioning steel determined via in-situ Electron Backscatter Diffraction', *Materials Science and Engineering a-Structural Materials Properties Microstructure and Processing*, 638: 219-27.

Dehoff, R. T. 1983. 'Quantitative Serial Sectioning Analysis - Preview', *Journal of Microscopy-Oxford*, 131: 259-63.

Diego-Calderon, I. de, I. Sabirov, J.M. Molina-Aldareguia, C. Fojer, R. Thiessen, and R.H. Petrov. 2016. 'Microstructural design in quenched and partitioned (Q&P) steels to improve their fracture properties', *Materials Science ad Engineering: A*, 657: 136-46.

Edmonds, D. V., K. He, F. C. Rizzo, B. C. De Cooman, D. K. Matlock, and J. G. Speer. 2006. 'Quenching and partitioning martensite - A novel steel heat treatment', *Materials Science and Engineering a-Structural Materials Properties Microstructure and Processing*, 438: 25-34.

El-Dasher, B.S., B.L. Adams, and A.D. Rollett. 2003. 'Viewpoint: Experimental recovery of geometrically necessary dislocation density in polycrystals', *Scripta Materialia*, 48: 141-45.

El Kadiri, H., J. C. Baird, J. Kapil, A. L. Oppedal, M. Cherkaoui, and S. C. Vogel. 2013. 'Flow asymmetry and nucleation stresses of {10(1)over-bar2} twinning and non-basal slip in magnesium', *International Journal of Plasticity*, 44: 111-20.

El Kadiri, H., J. Kapil, A. L. Oppedal, L. G. Hector, S. R. Agnew, M. Cherkaoui, and S. C. Vogel. 2013. 'The effect of twin-twin interactions on the nucleation and propagation of {10(1)over-bar2} twinning in magnesium', *Acta Materialia*, 61: 3549-63.

Fallahi, A., and A. Ataee. 2010. 'Effects of crystal orientation on stress distribution near the triple junction in a tricrystal γ-TiAl', *Materials Science and Engineering: A*, 527: 4576-81.

Field, D.P. 2005. 'Improving the spatial resolution of EBSD', *Microscopy and Microanalysis*, 11: 52-53.

Gardner, Calvin J., Brent L. Adams, John Basinger, and David T. Fullwood. 2010. 'EBSD-based continuum dislocation microscopy', *International Journal of Plasticity*, 26: 1234-47.

Groeber, M. A., B. K. Haley, M. D. Uchic, D. M. Dimiduk, and S. Ghosh. 2006. '3D reconstruction and characterization of polycrystalline microstructures using a FIB-SEM system', *Materials Characterization*, 57: 259-73.

Haidemenopoulos, G. N., M. Constantinou, H. Kamoutsi, D. Krizan, I. Bellas, L. Koutsokeras, and G. Constantinides. 2018. 'Probing the Evolution of Retained Austenite in TRIP Steel During Strain-Induced Transformation: A Multitechnique Investigation', *Jom*, 70: 924-28.

Haj-Ali, R., H. K. Kim, S. W. Koh, A. Saxena, and R. Tummala. 2008. 'Nonlinear constitutive models from nanoindentation tests using artificial neural networks', *International Journal of Plasticity*, 24: 371-96.

Hsu, E., J. E. Carsley, and R. Verma. 2008. 'Development of forming limit diagrams of aluminum and magnesium sheet alloys at elevated temperatures', *Journal of Materials Engineering and Performance*, 17: 288-96.

Izadbakhsh, A., K. Inal, R. K. Mishra, and M. Niewczas. 2011. 'New crystal plasticity constitutive model for large strain deformation in single crystals of magnesium', *Computational Materials Science*, 50: 2185-202.

Jacques, P.J., J. Ladriere, and F. Delanny. 2001. 'On the influence of interactions between phases on the mechanical stability of retained austenite in transformation-induced plasticity multiphase steels', *Metallurgical and Materials Transactions A: Physical Metallurgy and Materials Science*, 32: 2759-68.

Jimenez-Melero, E., N.H. van Dijk, L. Zhao, J. Sietsma, S.E. Offerman, J.P. Wright, and S. van der Zwaag. 2007. 'Martensitic transformation of individual grains in low-alloyed TRIP steels', *Scripta Materialia*, Scripta Materialia: 421-24.

Jon Scott, Michael Miles, David Fullwood, Brent Adams, Ali Khosravani, Raja K. Mishra. 2012. 'Room Temperature Shear Band Development in Highly Twinned Wtought Magnesium AZ31B Sheet', *Metall. Mater. Trans.A*, 44: 512-16.

Jonas, John J., Sijia Mu, Talal Al-Samman, Günter Gottstein, Lan Jiang, Ėtienne Martin, and Etienne Martin. 2011. 'The role of strain accommodation during the variant selection of primary twins in magnesium', *Acta Materialia*, 59: 2046-56.

Kabirian, F., A. S. Khan, and T. Gnaupel-Herlod. 2015. 'Visco-plastic modeling of mechanical responses and texture evolution in extruded AZ31 magnesium alloy for various loading conditions', *International Journal of Plasticity*, 68: 1-20.

Kacher, J., and A. M. Minor. 2014. 'Twin boundary interactions with grain boundaries investigated in pure rhenium', *Acta Materialia*, 81: 1-8.

Kacher, Josh, Brent Adams, and David Fullwood. 2009. "Detection of Tetragonalities and Pseudo-Symmetries by High Resolution EBSD Methods." In *MS&T*. Pittsburgh.

Kalidindi, S. R. 1998. 'Incorporation of deformation twinning in crystal plasticity models', *Journal of the Mechanics and Physics of Solids*, 46: 267-+.

Kelly, P. M. 1992. 'Crystallography of Lath Martensite in Steels', *Materials Transactions Jim*, 33: 235-42.

Kelly, P. M., A. Jostsons, and R. G. Blake. 1990. 'The Orientation Relationship between Lath Martensite and Austenite in Low-Carbon, Low-Alloy Steels', *Acta metallurgica et materialia*, 38: 1075-81.

Khosravani, A., J. Scott, M. P. Miles, D. Fullwood, B. L. Adams, and R. K. Mishra. 2013. 'Twinning in magnesium alloy AZ31B under different strain paths at moderately elevated temperatures', *International Journal of Plasticity*, 45: 160-73.

Khosravani, Ali, David Fullwood, John Scott, Michael Miles, and Raj Mishra. 2015. 'Nucleation and propagation of 1012 twins in AZ31 magnesium alloy', *Acta Materialia*, 100: 202-14.

Klimanek, P., and A. Potzsch. 2002. 'Microstructure evolution under compressive plastic deformation of magnesium at different temperatures and strain rates', *Materials Science and Engineering a-Structural Materials Properties Microstructure and Processing*, 324: 145-50.

Knezevic, Marko, Irene J. Beyerlein, Donald W. Brown, Thomas A. Sisneros, and Carlos N. Tomé. 2013. 'A polycrystal plasticity model for predicting mechanical response and texture evolution during strain-path changes: Application to beryllium', *International Journal of Plasticity*, 49: 185-98.

Knezevic, Marko, Mark R. Daymond, and Irene J. Beyerlein. 2016. 'Modeling discrete twin lamellae in a microstructural framework', *Scripta Materialia*, 121: 84-88.

Knezevic, Marko, Amanda Levinson, Ryan Harris, Raja K. Mishra, Roger D. Doherty, and Surya R. Kalidindi. 2010. 'Deformation twinning in AZ31: Influence on strain hardening and texture evolution', *Acta Materialia*, 58: 6230-42.

Knezevic, Marko, Milovan Zecevic, Irene J. Beyerlein, John F. Bingert, and Rodney J. McCabe. 2015. 'Strain rate and temperature effects on the selection of primary and secondary slip and twinning systems in HCP Zr', *Acta Materialia*, 88: 55-73.

Koike, J. 2005. 'Enhanced deformation mechanisms by anisotropic plasticity in polycrystalline Mg alloys at room temperature', *Metallurgical and Materials Transactions a-Physical Metallurgy and Materials Science*, 36a: 1689-96.

Kral, M. V. 2012. 'Proeutectoid ferrite and cementite transformations in steels.' in E. V. Pereloma and D. V. Edmonds (eds.), *Phase Transformation in Steels: Fundamentals and Diffusion-Controlled Transformations* (Woodhead Publishing Series in Metals and Surface Engineering).

Kroner, E. 1958. 'Continuum theory of dislocations and self-stresses', *Ergebnisse der Angewandten Mathematik*, 5: 1327-47.

Kumar, M. A., I. J. Beyerlein, R. J. McCabe, and C. N. Tome. 2016. 'Grain neighbour effects on twin transmission in hexagonal close-packed materials', *Nature Communications*, 7.

Kysar, J. W., Y.X. Gan, T.L Morse, Xi Chen, and M.E. Jones. 2007. 'High strain gradient plasticity associated with wedge indentation into face-centered cubic single crystals: Geometrically necessary dislocation densities', *Journal of the Mechanics and Physics of Solids*, 55: 1554-73.

Kysar, J.W., Y. Saito, M.S. Oztop, D. Lee, and W.T. Huh. 2010. 'Experimental lower bounds on geometrically necessary dislocation density', *International Journal of Plasticity*, 26: 1097-123.

Landon, C., B. Adams, and J. Kacher. 2008. 'High resolution methods for characterizing mesoscale dislocation structures', *Journal of Engineering Materials and Technology*, 130: 40-45.

Lebensohn, R. A., and C. N. Tomé. 1993. 'A self-consistent anisotropic approach for the simulation of plastic deformation and texture development of polycrystals: Application to zirconium alloys', *Acta Metallurgica et Materialia*, 41: 2611-24.

Lentz, M., A. Behringer, C. Fahrenson, I. J. Beyerlein, and W. Reimers. 2014. 'Grain Size Effects on Primary, Secondary, and Tertiary Twin Development in Mg-4 wt pct Li (-1 wt pct Al) Alloys', *Metallurgical and Materials Transactions a-Physical Metallurgy and Materials Science*, 45a: 4737-41.

Lentz, M., R. S. Coelho, B. Camin, C. Fahrenson, N. Schaefer, S. Selve, T. Link, I. J. Beyerlein, and W. Reimers. 2014. 'In-situ, ex-situ EBSD and (HR-)TEM analyses of primary, secondary and tertiary twin development in an Mg-4 wt%Li alloy', *Materials Science and Engineering a-Structural Materials Properties Microstructure and Processing*, 610: 54-64.

Li, L., L. M. Shen, G. Proust, C. K. S. Moy, and G. Ranzi. 2013. 'Three-dimensional crystal plasticity finite element simulation of nanoindentation on aluminium alloy 2024', *Materials Science and Engineering a-Structural Materials Properties Microstructure and Processing*, 579: 41-49.

Li, Wan-Song, Hong-ye Gao, Hideharu Nakashima, Satoshi Hata, and Wen-huai Tian. 2016. 'In-situ EBSD study of deformation behavior of retained austenite in a low-carbon quenching and partitioning steel via uniaxial tensile tests', *Materials Characterization*, 118: 431-37.

Littlewood, P.D., T.B. Britton, and A.J. Wilkinson. 2011. 'Geometrically necessary dislocation density distribution in Ti-6Al-4V deformed in tension', *Acta Materialia*, 59: 6489-500.

Marder, A. R., and G. Krauss. 1967. 'Morphology of Martensite in Iron-Carbon Alloys', *Asm Transactions Quarterly*, 60: 651-&.

Marder, J. M., and A. R. Marder. 1969. 'Morphology of Iron-Nickel Massive Martensite', *Asm Transactions Quarterly*, 62: 1-&.

Marion Calcagnatto, Dirk Ponge, Eralp Demir, Dierk Raabe. 2010. 'Orientation gradients and geometrically necessary dislocations in ultrafine grained dual-phase steels studied by 2D and 3D EBSD', *Materials Science and Engineering: A*, 527: 2738-46.

Martin, E., L. Capolungo, L. A. Jiang, and J. J. Jonas. 2010. 'Variant selection during secondary twinning in Mg-3%Al', *Acta Materialia*, 58: 3970-83.

Morito, S., Y. Adachi, and T. Ohba. 2009. 'Morphology and Crystallography of Sub-Blocks in Ultra-Low Carbon Lath Martensite Steel', *Materials Transactions*, 50: 1919-23.

Morito, S., H. Saito, T. Ogawa, T. Furuhara, and T. Maki. 2005. 'Effect of austenite grain size on the morphology and crystallography of lath martensite in low carbon steels', *Isij International*, 45: 91-94.

Morito, S., H. Tanaka, R. Konishi, T. Furuhara, and T. Maki. 2003. 'The morphology and crystallography of lath martensite in Fe-C alloys', *Acta Materialia*, 51: 1789-99.

Mueller, Mike. 2016. "Timeline: A Path to Lightweight Materials in Cars and Trucks." In, edited by Office of Energy Efficiency and Renewable Energy.

Niezgoda, Stephen R, Anand K Kanjarla, Irene J Beyerlein, and Carlos N Tomé. 2014. 'Stochastic modeling of twin nucleation in polycrystals: An application in hexagonal close-packed metals', *International Journal of Plasticity*, 56: 119-38.

Nye, J.F. 1953. 'Some geometrical relations in dislocated crystals', *Acta Metallurgica*, 1: 153-62.

Pantleon, W. 2008. 'Resolving the goemetrically necessary dislocation content by conventional electron backscattering diffraction', *Scripta Materialia*, 58: 994-97.

Perez-Benitez, J. A., and L. R. Padovese. 2011. 'Falling sheet envelope method for non-destructive testing time-dependent signals', *Expert Systems with Applications*, 38: 3192-98.

Proust, G., C. N. Tome, A. Jain, and S. R. Agnew. 2009. 'Modeling the effect of twinning and detwinning during strain-path changes of magnesium alloy AZ31', *International Journal of Plasticity*, 25: 861-80.

Proust, G., C. N. Tomé, and G. C. Kaschner. 2007. 'Modeling texture, twinning and hardening evolution during deformation of hexagonal materials', *Acta Materialia*, 55: 2137-48.

Quinlan, J. R. 1996. 'Improved use of continuous attributes in C4.5', *Journal of Artificial Intelligence Research*, 4: 77-90.

Quinlan, J.R. 1993. 'C4.5: programs for machine learning', *Morgan Kaufmann Publishers*.

Rampton, Travis Michael. 2015. 'Deformation Twin Nucleation and Growth Characterization in Magnesium Alloys Using Novel EBSD Pattern Analysis and Machine Learning Tools', Dissertation, Brigham Young University.

Rasmussen, J. 1983. 'Skills, Rules, and Knowledge - Signals, Signs, and Symbols, and Other Distinctions in Human-Performance Models', *Ieee Transactions on Systems Man and Cybernetics*, 13: 257-66.

Reich, Yoram, and Nahum Travitzky. 1995. 'Machine learning of material behaviour knowledge from empirical data', *Materials & Design*, 16: 251-59.

Rollett, A. D., R. Campman, and D. Saylor. 2006. 'Three dimensional microstructures: Statistical analysis of second phase particles in AA7075-T651', *Aluminium Alloys 2006, Pts 1 and 2*, 519-521: 1-10.

Roters, M. A. F., and D. Raabe. 2005. 'A dislocation density based constitutive model for crystal plasticity FEM', *Icotom 14: Textures of Materials, Pts 1and 2*, 495-497: 1007-12.

Ruggles, T. J., and D. T. Fullwood. 2013. 'Estimations of bulk geometrically necessary dislocation density using high resolution EBSD', *Ultramicroscopy*, 133: 8-15.

Russ, John C., and Robert T. DeHoff. 2000. *Practical stereology* (Kluwer Academic/Plenum: New York).

Santofimia, M. J., L. Zhao, and J. Sietsma. 2011. 'Overview of Mechanisms Involved During the Quenching and Partitioning Process in Steels', *Metallurgical and Materials Transactions a-Physical Metallurgy and Materials Science*, 42a: 3620-26.

Saylor, D. M., J. Fridy, B. S. El-Dasher, K. Y. Jung, and A. D. Rollett. 2004. 'Statistically representative three-dimensional microstructures based on orthogonal observation sections', *Metallurgical and Materials Transactions a-Physical Metallurgy and Materials Science*, 35a: 1969-79.

Scott, Jon, Michael Miles, David Fullwood, Brent Adams, Ali Khosravani, and Raja K. Mishra. 2012. 'Room Temperature Shear Band Development in Highly Twinned Wrought Magnesium AZ31B Sheet', *Metallurgical and Materials Transactions A*, 44: 512-16.

Sha, W., and KL Edwards. 2007. 'The use of artificial neural networks in materials science based research', *Materials & Design*, 28: 1747-52.

Shen, Y. F., L. N. Qiu, X. Sun, L. Zuo, P. K. Liaw, and D. Raabe. 2015. 'Effects of retained austenite volume fraction, morphology, and carbon content on strength and ductility of nanostructured TRIP-assisted steels', *Materials Science and Engineering a-Structural Materials Properties Microstructure and Processing*, 636: 551-64.

Speer, J.G., D.K. Matlock, L. Wang, and D.V. Edmonds. 2014. 'Quenched and Partitioned Steels', *Reference Module in Materials Science and Materials Engineering*, 1: 217-25.

Staroselsky, A., and L. Anand. 2003. 'A constitutive model for hcp materials deforming by slip and twinning: Application to magnesium alloy AZ31B', *International Journal of Plasticity*, 19: 1843-64.

Sun, S., B.L. Adams, and W.E. King. 2000. 'Observations of lattice curvature near the interface of a deformed aluminium bicrystal', *Philosophical Magazine A: Physics of Condensed Matter, Structure, Defects and Mechanical Properties*, 80: 9-25.

Tabacaru, V., and N. Oancea. 2001. 'Sheet metal forming of magnesium wrought alloys - Formability and process technology', *Journal of Materials Processing Technology*, 115: 14-19.

Taub, A. I., P. E. Krajewski, A. A. Luo, and J. N. Owens. 2007. 'The evolution of technology for materials processing over the last 50 years: The automotive example', *Jom*, 59: 48-57.

Tirumalasetty, G.K., M.A. van Huis, C. Kwakernaak, J. Sietsma, W.G. Sloof, and H.W. Zandbergen. 2012. 'Deformation-induced austenite grain rotation and transformation in TRIP-assisted steel', *Acta Materialia*, 60: 1311-21.

Tompos, A., J.L. Margitfalvi, E. Tfirst, and K. Héberger. 2007. 'Predictive performance of "highly complex" artificial neural networks', *Applied Catalysis A: General*, 324: 90-93.

Van Houtte, P. 1978. 'Simulation of the rolling and shear texture of brass by the Taylor theory adapted for mechanical twinning', *Acta metallurgica et materialia*, 26: 591-604.

Villert, S., C. Maurice, C. Wyon, and R. Fortunier. 2009. 'Accuracy assessment of elastic strain measurement by EBSD', *Journal of Microscopy*, 233: 290–301.

Wang, J., I. J. Beyerlein, and C. N. Tomé. 2010. 'An atomic and probabilistic perspective on twin nucleation in Mg', *Scripta Materialia*, 63: 741-46.

Wang, J., R. G. Hoagland, J. P. Hirth, L. Capolungo, I. J. Beyerlein, and C. N. Tomé. 2009. 'Nucleation of a (1, 0 1 2) twin in hexagonal close-packed crystals', *Scripta Materialia*, 61: 903-06.

Wang, S. Y., E. A. Holm, J. Suni, M. H. Alvi, P. N. Kalu, and A. D. Rollett. 2011. 'Modeling the recrystallized grain size in single phase materials', *Acta Materialia*, 59: 3872-82.

Wang, X. D., B. X. Huang, Y. H. Rong, and L. Wang. 2006. 'Microstructures and stability of retained austenite in TRIP steels', *Materials Science and Engineering a-Structural Materials Properties Microstructure and Processing*, 438: 300-05.

Want, H., C. N. Tomé, and Y. Huang. 2010. 'A finite strain elasctic-viscoplastic self-consistent model for polycrystalline materials', *Journal of the Mechanics and Physics of Solids*, 58: 594-612.

WEKA. 2010. "Waikato Environment for Knowledge Analysis (WEKA)." In. Hamilton, New Zealand: The University of Waikato.

Wilkinson, A. J., G. Meaden, and D. J. Dingley. 2005. 'Elastic Strain Tensor Mapping - extending the limits of EBSD analysis', *Microscopy and Microanalysis*, 11: 520-21.

Wilkinson, A. J., G. Meaden, and D. J. Dingley. 2006. 'High resolution mapping of strains and rotations using electron backscatter diffraction', *Materials Science and Technology*, 22: 1271-78.

Wright, S. I. 2010. 'A Parametric Study of Electron Backscatter Diffraction based Grain Size Measurements', *Praktische Metallographie-Practical Metallography*, 47: 16-33.

Wright, Stuart, Matthew Nowell, and John Basinger. 2011. 'Precision of EBSD based orientaion measurements', *Microscopy & Microanalysis*, 17: 406-07.

Xiong, X. C., B. Chen, M. X. Huang, J. F. Wang, and L. Wang. 2013. 'The effect of morphology on the stability of retained austenite in a quenched and partitioned steel', *Scripta Materialia*, 68: 321-24.

Yassar, R. S., O. AbuOmar, E. Hansen, and M. F. Horstemeyer. 2010. 'On dislocation-based artificial neural network modeling of flow stress', *Materials & Design*, 31: 3683-89.

Yoo, M H. 1981. 'Slip, Twinning and Fracture in Hexagonal Close-Packed Metals', *Metallurgical and Materials Transactions A, Physical metallurgy and materials science*, 12: 409-18.

Yoshinaga, H., T. Obara, and S. Morozumi. 1973. 'Twinning deformation in magnesium compressed along the C-axis', *Materials Science and Engineering*, 12: 255-64.

Yue, Jiansong Wan and Zhufeng. 2003. 'Non-uniform Stress Field and Stress Concentration Inducedby Grain Boundary and Triple Junction of Tricrystal', *J. Mater. Sci. Technol.*, 18: 303-08.

Zecevic, M., M. Knezevic, I.J. Beyerlein, and C.N. Tomé. 2015. 'An elasto-plastic self-consistent model with hardening based on dislocation density, twinning an de-twinning: Application to strain path changes in HCP metals', *Mater. Sci. Eng. A*, 638: 262-74.

Zhang, K.F. F, D.L. L Yin, and D.Z. Z Wu. 2006. 'Formability of AZ31 magnesium alloy sheets at warm working conditions', *International Journal of Machine Tools and Manufacture*, 46: 1276-80.